DOCTORAL DISSERTATION

SEISMIC HAZARDS AND DAMAGE ASSESSMENTS BASED ON REMOTE SENSING AND GIS TECHNOLOGIES

SADRA KARIMZADEH

June 2015

博士論文

SEISMIC HAZARDS AND DAMAGE ASSESSMENTS BASED ON REMOTE SENSING AND GIS TECHNOLOGIES

リモートセンシングと GIS 技術による地震危険度および被害評価

金沢大学大学院自然科学研究科

環境科学専攻

環境計画講座

Student Number: 1223142015

Name: SADRA KARIMZADEH

Supervisor: Professor MASAKATSU MIYAJIMA

Date of Submission: June 2015

Summary

Geospatial Information System (GIS) basically works with coordinates and datums. They enable geographic datasets to use common locations for integration (Booth and Mitchell, 2001). A coordinate system in GIS (coordinates and a datum) is a reference system used to represent the locations of geographic features and observations within a common geographic framework. Rather than being completely independent, GIS has gradually developed by linking a number of discrete information into a whole that is greater than the sum of its components. GIS has served an important role as an integrating technology in the past two decades, especially its applications with remote sensing data have increased (Burrough et al., 2000; De Reu et al., 2013; Drăguţ and Blaschke 2006; Iwahashi and Pike 2007; Luo et al., 2014; Raup et al., 2007; Song et al., 2012; Yu et al., 2012) [9, 15, 16, 25, 31, 49, 51, 58]. The flexible structure of GIS technology increases its applications and the development of GIS has relied on innovations made in many different disciplines. In the present study for remote sensing developments, firstlywe have studied tectonic and non-tectonic natural hazards in NW Iran using PS-InSAR time series analysis of 17 ENVISAT ASAR images acquired between 2004 and 2010 using combination of the permanent scatterers InSAR (PSI) and the small baseline InSAR (SBAS) approach. At the first step, the majority achievements include the following contributions: 1) Reported the first interseismic slip rate (8.7 ± 2.5 mm/year) and locking depth (15.8 ± 10.8 km) of the North Tabriz Fault (NTF) using elastic dislocation modeling of the mean line-of-sight velocity field estimated from PS-InSAR time series [*Karimzadeh et al., JG, 2013*]. This supports the results of Iranian GPS network [*Djamour et al., EPSL 2011*] that earthquake recurrence intervals for large earthquake (Mw 7–7.3) on the NTF are about 250–300 years [*Wells and Coppersmith, BSSA, 1994*].Therefore, 2) an elapse time of 234 and 293 years since the two last major earthquakes (1780 and 1721) nearby Tabriz city on the NTF implies a high potential for a large earthquake in the next several decades.3)The study area also had a potential of land subsidence owing to its arid and semi-arid climate and necessity of the agricultural activities for ground water extraction. Thus, 4) three regions of rapid subsidence with a maximum rate of 20 mm/year were detected near some critical structures such as: Tabriz thermal power plant and petrochemical facilities in Tabriz basin. [*Karimzadeh et al., JG, 2013*]. The analyzed piezometer measurements support the land subsidence phenomenon in Tabriz basin since 2008 ground water extraction largely accelerated. At the second step, investigation of the seismicity of the study area has taken into account. We described the development of a comprehensive earthquake catalog for NW Iran by unifying all of the records (historical pre-1900 earthquakes + instrumental events) and determinedsome of the seismicity information such as range of magnitudes, number of events, length of the potential faults and their distance from the built areas. The statistical results of instrumental earthquake

catalogs in the study area with a radius of 150 km indicated that the seismogenic depth was approximately 20 km and fewer daytime than nighttime earthquakes were recorded, also coulomb stress distribution of the last earthquake (Ahar-Varzaghan earthquake 2012) has been studied [*Amiraslanzadeh et al., JAEE 2013*; *Karimzadeh et al., JAEE, 2013*; *Karimzadeh et al., SDEE, 2014*]. Using the obtained results in the second step, creation of microzonation maps and earthquake scenarios for the study area would be much accurate and easier. At the third step, a GIS-based procedure that illuminates the consequences of a possible earthquake is presented in two main tasks (1-seismic microzonation; 2- building and human damages). An accurate seismic microzonation map of the study area has created through a series of influential parameters in site amplification (i.e., geology, alluvial thickness, ground water level and sedimentology) and in natural hazards (i.e., the detected land subsidence at the step 1 and prepared earthquake catalog at the step 2). Beside the aforementioned parameters, different data (remote sensing data) and geoid slope contributed and adopted to be utilized in the ArcGIS environment. The detailed geological, geodetical, geotechnical and geophysical parameters of the region are combined using an Analytic Hierarchy Process (AHP) and a deterministic near-field earthquake of magnitude 7 in the NTF was simulated. This simulation provided differing intensities of ground shaking in the different districts of Tabriz city. Using the simulated Ground Shaking Map, the vulnerability of buildings, human losses and basic resources for survivors was estimated in the city based on fragility curves, damage functions and relational analyses. Overall the obtained results help decision-makers and urban planners for taking better strategies and quick responses against natural disasters like earthquakes, landslides, etc. [*Karimzadeh et al., SDEE, 2014*].At the final step, we worked to depict effect of topography on seismic amplification owing to irregular shape of terrain in order to characterize seismic record stations using ASTER digital elevation data and Topographic Position Index (TPI) [*Karimzadeh et al., JS, 2015*].

Acknowledgments

بسم الله الرحمن الرحيم

SEISMIC HAZARDS AND DAMAGE ASSESSMENTS BASED ON REMOTE SENSING AND GIS TECHNOLOGIES

TABLE OF CONTENTS

LIST OF FIGURES

LIST OF TABLES

1. Introduction

1.1 Background

Initial hazard, building damage and human assessments are important for critical cities. Indeed spatial earthquake hazard assessment studies play a key role in identifying and mitigating the potential consequences of an earthquake in the hazardous cities. In the recent decades developments in remote sensing techniques (e.g. image processing, phase processing) are serving a great help for seismologists, geologists and civil engineers in order to identify scale of damage, geology units and initial hazards (Cinicioglu et al., 2007; Pessina and Fiorini 2014)[1-2]. One case in this thesis is InSAR method, for instance, for either crustal or building damage mapping, high spatial resolution optical satellite imagery is one of the popular methods. However, owing to frequent occurrence of clouds, smog, etc., optical data is not always useful, but space-borne Synthetic Aperture Radar (SAR) sensor allows us to monitor a wide field of ground (i.e. from tens of km to more than 100 km) at low costs with a regular revisit interval. At the present time, various phenomena in different fields can be studied by SAR imagery. SAR has several advantages compared to optical sensors. First, as an active sensor SAR is independent of day and night, while passive optical sensors use the solar radiation. Second, due to its larger wavelength (λ: mm to dm) SAR is almost an all-weather and all-condition technique as only larger atmospheric changes in the time between the radar acquisitions have an influence on interferometric (InSAR) applications (Plank 2014) [3]. In mostcircumstances, GIS, expert systems and statistical methods are also used jointly with remote sensing technologies (Hashemi et al., 2014; Ren et al., 2014) [4,17]. On the other hand, experiments and results of the areas which shocked by strong earthquakes in the last decades provided enough evidence to suggest that local parameters like alluvial thickness, local geology, topography, ground water level, etc., may alter earthquake waves and amplify certain period bands of ground motion significantly (Borcherdt, 1994) [5]. Ground shaking affects the structures by both its direct action and also indirectly by changing the state of the soil (consistency, continuity and rigidity) and thus its constitutive response.One of the basic necessities of disaster management for cities during (co-), after (post-) or even before (pre-) an earthquake is the provision of a well-enriched geodatabase including results from remote sensing data. This database with GIS support helps engineers and urban planners to predict future events, which allows them to design better strategies for the future of cities. A spatially based earthquake scenario to plan for quick responses is the basis of urban preparation and earthquake disaster management using decision-making techniques. Disasters, such as earthquakes, floods and fires, significantly affect the community and infrastructures. Most natural phenomena are characterized by short action, but their impacts, such as that on buildings or other tangible structures, persists for years.

1.2 Thesis objectives

This thesis is a multi-disciplinary one (Fig. 1.1a), among GIS, seismology and earthquake engineering focused on seismically active country Iran emphasizing on Remote sensing and ground truth data. At the first step, surface deformation along the North Tabriz Fault (NTF) deduced from Synthetic Aperture Radar Interferometry (InSAR) technique will be presented. The estimated slip rate would be important for initial hazard estimation of Tabriz city which is located in the near of the NTF, also using empirical relations and inverse modeling, the approximate locking depth of the NTF can be estimated, and then can be compared with other observations (e.g., GPS time series). Next objective, using paleoseismology of the interested area, new earthquake catalogs and statistical analysis, one could be able to assess the seismicity of the study area to understand what they want to do at the next step (step2). For instance, if you want to define an earthquake scenario, having knowledge about active surrounding faults, their distances to the inhabited areas, as well as number day/night earthquakes happened in the past would be important for realizing seismicity nature of the study area and defining true and effective scenarios either deterministic or probabilistic. The objective of third step is to develop an integrated GISsystem for earthquake studies as much as close to the reality using influential parameters on seismic wave amplification in order to assess seismic hazard, building and human losses. The developed GIS will benefit various factors, methods and functions. Each country has own risk/hazard/damage model which enhances the ability and resilience of experts and urban planners against natural disasters. For instance, HAzards United States (HAZUS) is an example of the second category. It is a multi-hazard model for the three main natural disasters in the US, i.e., earthquakes, winds and floods, that was developed by the Federal Emergency Management Agency (FEMA) [6,7]. It operates on the ArcMap interface and estimates physical damages (i.e., buildings, pipeline networks) and social damage (i.e., casualties) based on damage functions and census tract areas, respectively. The presented model in this thesis mostly adopted with common hazards in Iran, accordingly fire and storm hazards are neglected naturally, because earthquakes and drought aredominant natural hazards which threat the country. However, the presented model's main objective is focused on earthquake damages on buildings and human life. Studies show that earthquake casualties in Iran are 20% more than the world norm, thus more detailed information of earthquake parameters are considered in this thesis(Hashemi and Alesheikh 2011; Hassanzadeh et al., 2013)[8,9]. More detailed information lead to an accurate seismic microzonation, accordingly building and human damage estimations would be closer to the reality. The final objective defined in this thesis is the fast characterization of seismic stations in Iran through GIS and remote sensing. Topographic Amplification Factor (TAF) due to ground surface irregularity could be one of the reasons of earthquake wave amplification and unexpected damage of buildings or other tangible structures located on the top of hills in many examples. Here, an

integrated model using GIS and remote sensing for topographic position index (TPI) and seismic network development will be the last objective.
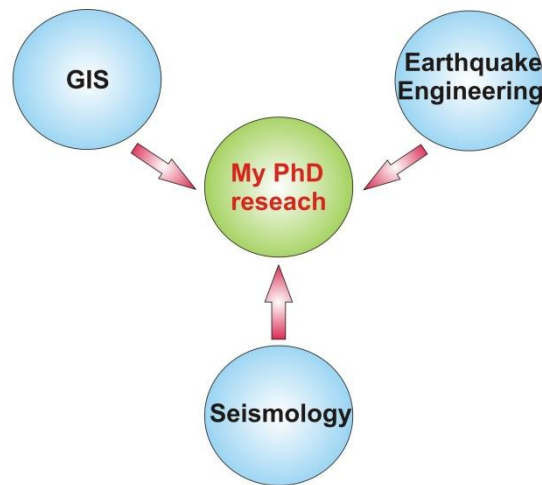
Fig.1.1 Sketch of the current research

1.3 Remote sensing principals

Remote sensing has been define in different concepts, however in this thesis an adequate definition of remote sensing is: observation technology of a specific scene, object or phenomena (e.g. fault slip rate) by sensor-based techniques without physical contact only through electromagnetic or light waves. This definition of remote sensing can be used in different disciplines like: archeology, earth sciences, architecture, earthquake engineering, etc.

1.3.1 Concepts

Although application of remote sensing are expanded between planets. Here, we desire it is in spacecraft observations of the surfaces and atmospheres of the Earth, focusing on Earthquake-related studies. Since various concepts are included in remote sensing technology, we only introduce essential concepts related with the topic.

1.3.1.1 Sensors

In remote sensing issues, sensor is a device to measure level of electromagnetic waves. In general manner, sensors are two types. 1- Passive sensors which use external energy sources (e.g. solar energy). They usually work in a range between 1 picometer and 1 meter (Fig. 1.2). 2- Active sensors which use their own energy or in other words, they work by sending infrared light or ultrasound waves into the Earth. Thereafter, sensor keepsthe recorded energy of the returned

waves for further analysis. When there is no moment of an object (here we assume tectonic movements) or a person in the path of sound waves or light, the floor or walls reflects back the energy without any change inthe level of energy. It means the recorded wave will have static manner when there is no moment. In case of any moment, sensor responds to the recorded waves by the object and sends the signal to the installed system for further action like opening and closing an aperture.

In order to collect and record energy reflected or emitted from a target on the earth (e.g. interseismic movements of a specific fault), the sensor must be assembled on a steady platformremoved from the target or surface being observed. Platforms for remote sensors may be situated on the ground, on an aircraft/spacecraft outside of the Earth's atmosphere.
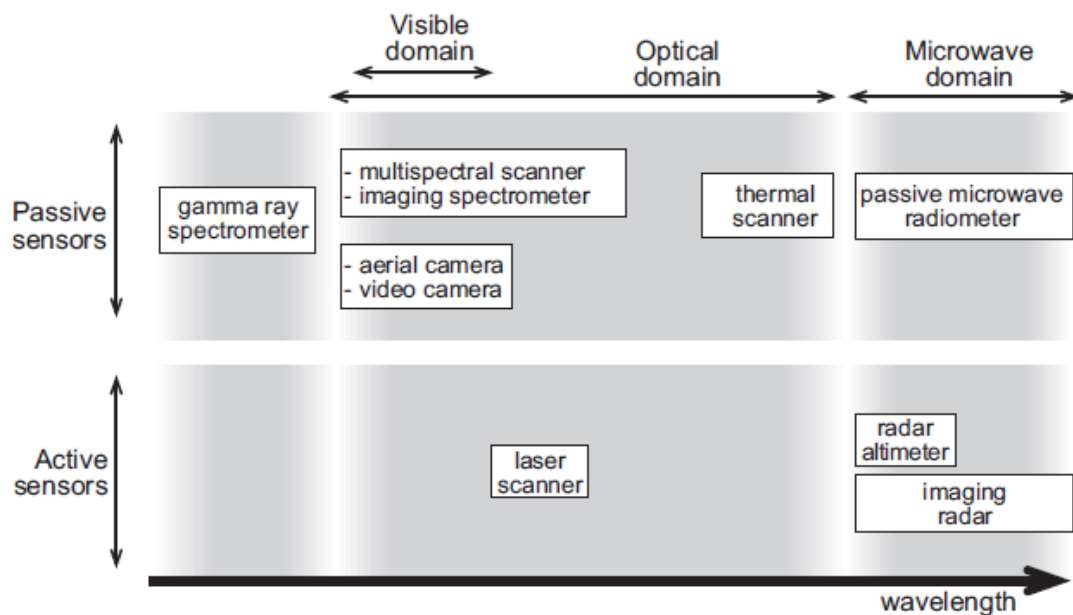
Fig.1.2 Wavelength domain of active and passive sensors(Tempfli et al., 2009) [10].

1.3.1.2 Spectral resolution

Spectral resolution is the sensitivity of a sensor to emittanceof avariety of wavelengths (mostly for satellite and airborne sensors). The frequency ranges covered often include not only visible light but also non-visible light and electromagnetic radiation. Objects on the ground can be identified by the different wavelengths reflected (interpreted as different colors) but the sensor used must be able to detect these wavelengths in order to see these features.Typical spectral classes are water and vegetation which can usually be separated using very broad wavelength ranges (the visible and near infrared). However, other complex classes (e.g. rock classes) would be tricky and may not be easily distinguishable using either of these broad wavelengths. Thus, a sensor with higher spectral resolution is needed[11].

1.3.1.3 Geometric distortion

Satellite or airborne images, regardless of their acquired methods have different distortions in their first level of acquisition. This is a usual defect in allprojects with 3D data which we want to project on a 2D surface (e.g. on a paper) including remote sensing missions, as we attempt to accurately represent the 3D surface of the Earth as a 2D image. All remote sensing images are subject to some form of geometric distortions, depending on data acquisition strategies. Common error sources are as follow:

- the view angle of the sensor
- the motion of the scanning system,
- the instability of the platform,
- the platform altitude, attitude, and velocity
- the curvature and rotation of the Earth.

1.3.1.4 Land observation

Land observation through remote sensing is a technology to gather information of the Earth in different sides of the science (e.g. chemical and physical data). In recent years, in land observation, many advances have been achieved and more sophisticated techniques have been presented in Japan and elsewhere (Pulido et al., 2012; Maruyama et al., 2012; Liu and Yamazaki 2013)[12-14]. It has also become more important due to the dramatic impact of earthquakes and other disasters like typhoons on the planet Earth, and the need to minimize negative impacts along with the opportunities land observation provides to improve social and economic well-being. In this thesis we deal on land observation application to monitor and assess both natural environment (the fault slip rate) and the built environment (integration of variety data for building damage assessment).

1.4 InSAR

Interferometric Synthetic Apreture Radar (InSAR) is a radar technique in remote sensing which works based on phase differences between two radar acquisitions (Fig. 1.3). It had a long way to become a widely used technique to study surface deformations. Although the phase ϕ has different unit, unlike displacement units (e.g. cm; mm), but it is directly related with $2R$ travel distance of the signal (double travel distance from the sensor to the ground and scattering way). Different sensor positions during two acquisitions receive slightly different phase signals as the

distance from the second SAR sensor to the object on the ground is by the amount of ΔR larger than the corresponding distance from the first SAR (Fig.1.4).

$$\phi_1 = -4\pi\lambda R_s + \phi_{scatt1} \quad (1.1)$$

$$\phi_2 = -4\pi\lambda R_s + \Delta R + \phi_{scatt2} \quad (1.2)$$

$$\Delta R = B_\perp \tan\phi \quad (1.3)$$

Assuming constant backscattering properties at both acquisition times ($\phi_{scatt1} = \phi_{scatt2}$), the interferometric phase ϕ_{int} is: $\phi_{int} = \phi_1 - \phi_2 = 4\pi\lambda\Delta R$ (Plank 2014).

Now itis recognized as a sophisticated technique of space geodesy to measure surface displacements in different aspects, especially, its high sensitivity for vertical deformations and wide spatial coverage is one of the advantages in Earth sciences(Motagh et al., 2007; Ciampalini et al., 2014) [15,16].
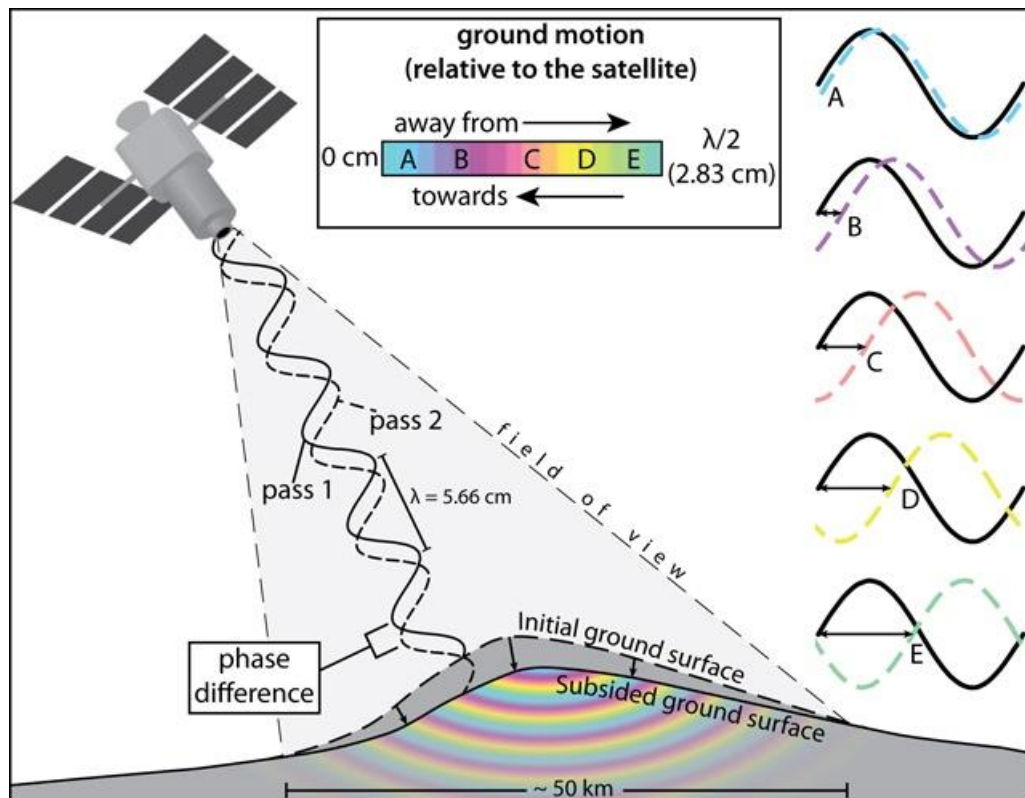
Fig.1.3 Principals of InSAR technique is based on phase differences of electromagnetic waves between two epochs [*Leo's website: http://www.volcano.si.edu/*].
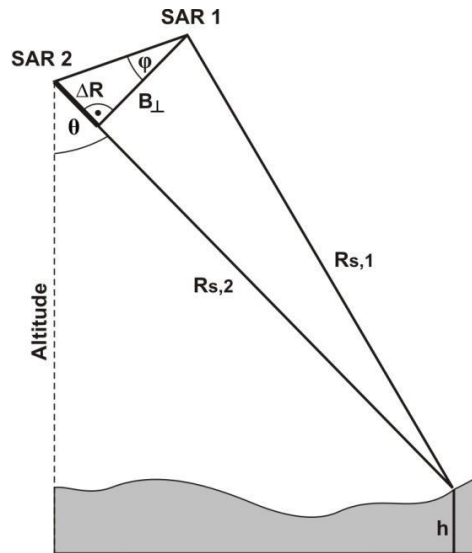
Fig.1.4 InSAR geometry including phase differences recorded at the two SAR acquisitions (SAR1 and SAR2). ΔR is the distance from SAR 2 to the target on the ground is longer than the distance from SAR 1 to the object. $B_\perp$ is the perpendicular baseline between two acquisitions.

References

[1] Cinicioglu S.F, Bozbey I, Oztoprak S, Kelesoglu M.K. An integrated earthquake damage assessment methodology and its application for two districts in Istanbul, Turkey. Engineering Geology 2007; 94: 145–165.

[2] Pessina, V., Fiorini, E., 2014.A GIS procedure for fast topographic characterization of seismic recording stations.Soil Dynamics and Earthquake Engineering 63, 248–258.

[3] Plank, S., 2014. Rapid Damage Assessment by Means of Multi-Temporal SAR — A Comprehensive Review and Outlook to Sentinel-1. Remote Sensing 6, 4870-4906.

[4] Hashemi, M., Alesheikh, A., Zolfaghari, M.R., 2014. A spatio-temporal model for probabilistic seismic hazard zonation of Tehran.Computers & Geosciences 58, 8–18.

[5] Borcherdt, R.D., 1994. New Developments in Estimating Site Effects on Ground Motion ATC-35-1.Report.

[6] FEMA, 2003a.HAZUSMH MR4 Earthquake Model User Manual.Department of Homeland Security.Federal Emergency Management Agency.MitigationDivision.Washington, D.C. 2012; www.fema.gov/library/viewRecord.do?id=3732.

[7] FEMA, 2003b.HAZUSMH MR4 Earthquake Model Technical Manual. Department of Homeland Security.Federal Emergency Management Agency.Mitigation Division.Washington, D.C. 2012; www.fema.gov/library/viewRecord.do?id=3732.

[8] Hashemi M, Alesheikh A.A. A GIS-based earthquake damage assessment and settlement methodology. Soil Dynamics and Earthquake Engineering 2011; 31: 1607–1617.

[9] Hassanzadeh R, Zorica N, AlaviRazavi A, Norouzzadeh M, Hodhodkian H.Interactive approach for GIS-based earthquake scenario development and resource estimation (Karmania hazard model). Computers & Geoscience 2013; 51: 324–338.

[10] Tempfli, K., Kerle, N., Huurneman, G., Jasnssen, L.L., 2009. Principiles of Remote Sensing (An introductory textbook). The International Institute for Geo-Information Science and Earth Observation.

[11] Fundamentals of Remote Sensing, 2013.Natural Resources Canada.

[12] Pulido, N., Tavera, H., Aguilar, Z., Nakai, S., Yamazaki, F., 2012. : Strong Motion Simulation of the M8.0 August 15, 2007, Pisco Earthquake; Effect of a Multi-Frequency Rupture Process. Journal of Disaster Research 8, 235-242.

[13] Maruyama, Y., Yamazaki, F., Matsuzaki, S., Miura, H., Estradac, M., 2012.Evaluation of Building Damage and Tsunami Inundation Based on Satellite Images and GIS Data Following the 2010 Chile Earthquake.Earthquake Spectra, 28, S165–S178.

[14] Liu, W.,Yamazaki, F., 2013. Detection of Crustal Movement From TerraSAR-X Intensity Images for the 2011 Tohoku, Japan Earthquake. IEEE geoscience and remote sensing letters 10, 199-203.

[15] Motagh, M., Hoffmann, J., Kampes, B., Baes, M., Zschau, J., 2007. Strain accumulation across the Gazikoy–Saros segment of the North Anatolian Fault inferred from Persistent Scatterer Interferometry and GPS measurements. Earth Planet. Sci. Lett. 255, 432–444.

[16] Ciampalini, A., Bardi, F., Bianchini, S., Frodella, W., Del Ventisette, C., Moretti, S., Casagli, N., 2014.Analysis of building deformation in landslide area using multisensory PSInSAR technique. International Journal of Applied Earth Observation and Geoinformation 33, 166–180.

[17] Ren, Z., Zhang, Z., Dai, F., Yin, J., Zhang, H., 2014 Topographic changes due to the 2008 Mw 7.9 Wenchuan earthquake as revealed by the differential DEM method. Geomorphology 217, 122–130.

2. A GIS based tool for topographic characterization of seismic stations in Iran

2.1 General remarks

This chapter deals with the integrated use of GIS tool "Topographic Position Index" and remotely sensed DEM in earthquake engineering and seismology. For better understanding of the subject, we should take a deeper look to the history and clarify some fundamental definitions.

The mapping was started from an ancient era and even now it is developing rapidly which deals with spatial information like the "Where" question. From the Neanderthal to the Human, all were asking same questions like "Where is my cave!? or "Where is the starting point?". These sorts of questions show that how much the mapping and the locations are important and can be helpful. Long before, (~ 250 B.C.), the Greek Eratosthenes used a checkerboard-like grid to locate positions on the Earth in order to answer all of the above questions, but probably René Descartés was the first person who discussed this issue widely and tried to pour the real world on a graph (i.e. coordinate system) after watching a fly walk on his ceiling and then he tracked the meandering path with his invented system. His system comprised of X-axis and Y-axis in which each element of the coordinate pair is the distance measured across a flat plane from the point. After this revolutionary achievement, the coordinates were a part of natural researches in many cases (Van Sickle 2004) [54]. The second distinct achievement came in the year 1968 when Roger Tomlinson convinced the scientific community that computers could be used to automate map analysis by emphasizing of the attributable term "geographic" and has created opportunities and challenges for the discipline of geoscience ever since (Tomlinson 1968) [53]. Thus, the creation of coordinates was a good opportunity for mankind to establish an easier communication and better understanding of surroundings, but it was not enough for what humans want to know about the environment until datums were created. Geospatial Information System (GIS) basically works with coordinates and datums. They enable geographic datasets to use common locations for integration (Booth and Mitchell, 2001) [8]. A coordinate system in GIS (coordinates and a datum) is a reference system used to represent the locations of geographic features and observations within a common geographic framework. Rather than being completely independent, GIS has gradually developed by connecting a number of discrete information into a whole box that is greater than the sum of its components. GIS has served an important role as an integrating technology in the past two decades, especially its applications with remote sensing data have increased (Burrough et al., 2000; De Reu et al., 2013; Drăguţ and Blaschke 2006; Iwahashi and Pike 2007; Luo et al., 2014; Raup et al., 2007; Song et al., 2012; Yu et al., 2012) [9, 15, 16, 25, 31,

49, 51, 58]. The flexible structure of GIS technology increases its applications and the development of GIS has relied on innovations made in many different disciplines.

Developments in remote sensing technologies have led to digital elevation models (DEMs) being freely available with worldwide coverage. DEMs created from these technologies (e.g. ASTER 30m or SRTM 90m) have enormous applications in soil sciences, earthquake studies, etc. (Liu et al., 2012; Pessina and Fiorini, 2014; Ren et al., 2014; Song et al., 2012) [30, 45, 50, 51]. For example in morphological sciences, diverse land classifications using Digital Elevation Models (DEM) have been suggested due to different methods which incorporate a range of topographic input variables (Hengl and Rossiter, 2003; Irvin et al., 1997; Giles, 1998; MacMillan et al., 2000; Miliaresis and Argialas, 1999; Prima et al., 2006) [21, 24, 19, 33, 36, 48]. These efforts focused on either homogenous (i.e. hill-slope regions) (Miliaresis and Argialas, 1999) [36] or heterogeneous regions (De Reu et al., 2013) [15]. Usually embedded math tools in GIS can easily changes theoretical formulas into actionable status by very diverse calculation methods which enable us to study various aspects of remote sensing data. For instance, Pike et al., (2009) [46] remarked that DEM-derived maps could be tricky, as the parameters can be generated by different procedures or sampling strategies and can vary with spatial scale. Another example, in seismic studies, Topographic Amplification Factor (TAF) due to irregular surface of terrain could be one of the reasons of earthquake wave amplification and unexpected damage of buildings or other tangible structures located on the top of hills in many previous studies. Moreover in most of previous earthquake-related studies, irregularity of the shape of the Earth or in other words "topography" has an enormous role in secondary-induced hazards like landslides (Chen et al., 2011; Carpentier et al., 2012) [13, 10]. Using high resolution ASTER data with the support of an ad hoc procedure of ArcGIS toolbox, Pessina and Foirini, 2014 did a morphological assessment of over 800 stations in Italy and Switzerland. Information of characterized stations could open new ways for seismology engineers to improve the formulation of new ground motion prediction equations. Also it could be helpful for governments or strategy-planners to find a way for reasonable urban growth directions and settlement plans. This study concentrates on application of a joint GIS-RS method for characterization of seismic stations in Iran. A semi-automatic indexing procedure of GIS is combined with remotely-sensed topographic data (ASTER). It could reveal impacts of naturally neglected topographic amplification of earthquake ground shaking in Iran where top hill ridges could amplify the seismic waves rather than investigation of earthquake source characterizations.

2.2 Study area

Here we again focus on Iran as a target area, but this time beside of the tectonic features, we discuss about the seismic networks established in Iran as well.

2.2.1. Seismotectonic setting and seismicity

As discussed in previous chapters, Iran is a vast country between Arabia (with northward movement) and Eurasia (slab) plates. In the last decade, many works have been conducted about tectonic features of Iran using space geodesy techniques like GPS constrains which show that continental convergence and active crustal shortening of the Arabian plate with respect to the Eurasian slab plate (Masson et al., 2006; McClusky et al., 2000; Tavakoli, 2007; Vernant et al., 2004) [34, 35, 52, 55]. The GPS-derived velocity (22±2 mm/yr) of the Arabia plate with respect to the Eurasia plate suggested by McClusky et al. (2000) [35] indicates counterclockwise rotation of anextensivepart of Middle East including Iran (adjacent parts of the Zagros and central Iran). Thus the convergence of these plates results in the emergence of many thrusts and strike slip faults in Iran with a considerable amount of casualties due to earthquake disaster as one of the earthquake prone countries in the world (Berberian, 2014) [6]. These faults are capable of producing a lot of earthquakes each year. However most of historical moderate/small events were missed. Statistical analysis of the events with five-year intervals confirms that the number and accuracy of events were increased from the 20th century until now (Zare et al., 2014) [61]. Range of magnitude of recent earthquake catalog in the Middle East reveals that maximum and minimum events in Iran are M=4.0 and M=8.1 respectively. Seismotectonic classifications differ from one country to another country. There is not a straightforward standard for seismotectonic classification so far. Different strategies benefit from different factors such as similar tectonic position, seismicity pattern and geological feature during the classification procedure. When we look to the past, two main approaches were conducted for the seismotectonic classification in Iran. The first one is based on geological featuresand the second one isbased on seismotectonic differences(Aghanabati, 2004) [1]. Nowroozi (1976) [43] created the first seismotectonic classification using seismotectonic difference such as over 600 earthquakes (1920-1972), geographical and geological information, regional geomorphology, as well as the information from salt domes, active faults and structural trends. In this study, according to available geophysical, geological, tectonic, and earthquake data, the region of interest is divided into six seismotectonic blocks (Mirzaei et al., 1998) (Fig. 2.1) [38] as follows:

1- Alborz & Azerbaijan: The heavily populated Alborz & Azerbaijan block is located in the west and south west of the Caspian Sea and includes the Alborz mountains extending to the Kopet Dag block in the east. The seismically active Alborz & Azerbaijan block experienced destructive earthquakes throughout history. Some of the major earthquakes in the recent decades are: The Hamadan earthquake (M 7) of 1957 (1130 people killed), Buin-Zahra earthquake (M 7.2) of 1962 (12000 people killed) and lastly the Ahar-Varzaghan twin earthquakes (M6.3 and M 6.4) of 2012 (300 people killed) (Neghabat and Liu, 1977; Zare et al., 2012) [41, 60] which occurred 60 km

away from the apparently active North Tabriz Fault with a recently suggested slip rate of 8.7±2.5 mm/yrcapable of producing an earthquake M 7.0-7.3 (Karimzadeh et al., 2013a) [27]. 2- Central Iran: This block covers an area in south of the Kopet Dag block and east of the Lut block and from the west its boundaries are limited by the Zagros thrust zone. Remarkable events in this zone are the Dasht-e-Bayaz earthquake (M 7.4) of 1968, the Kashan earthquake of 1903 (200 people killed) and the Torbat-e-Heydariyeh earthquake (M 5.7) of 1923 (2000 people killed) (Neghabat and Liu, 1977) [41]. 3- Zagros: It is statistically the most active block of Iran with a large number of recorded events which extends southwestward to the northern edge of Persian Gulf(Zare et al., 2014; Neghabat and Liu, 1977) [61, 41]. It stretches over 1300km and has a distinct trace on satellite images or topography maps (Fig. 2.1). Major earthquakes in this region are: the Lar earthquake (M6.9) of 1961 (60 people killed), the Bastak earthquake (M 6.4) of 1956 (255 people killed) and a bunch of large and moderate earthquakes in Shiraz and Qeshm island (Neghabat and Liu, 1977) [41]. 4- Makran: This block is a subduction zone which lies along the south part of the Lut block. The less populated Makran zone experienced a mega earthquake (M 8) in 1945 and recently the Saravan earthquake (7.8) of 2013 happened in the region (Karimzadeh et al., 2013b) [28]. 5- Lut: Dasht-e-Lut is a vast desert which comprises a major part of this region bounded by the Central Iran and the Makran block in north and south respectively. The lower elevation and recorded events in the Dasht-e-Lut suggest that the Lut Block is a relatively rigid block within this distributed deforming zone (Zare et al., 2014) [61]. 6- Kopet Dag: This region includes mountains located in the east of the Caspian Sea and south of the Central Iran block. The recorded events in the mountainous Kopet Dag block show existence of either reverse or strike slip faulting mechanisms in the past (Priestley, 1992) [47]. One of the major and destructive earthquakes in this region occurred in 1929 (M 7.4) with 3800 casualties in the epicentral area (Mirzaei et al., 1998) [38].
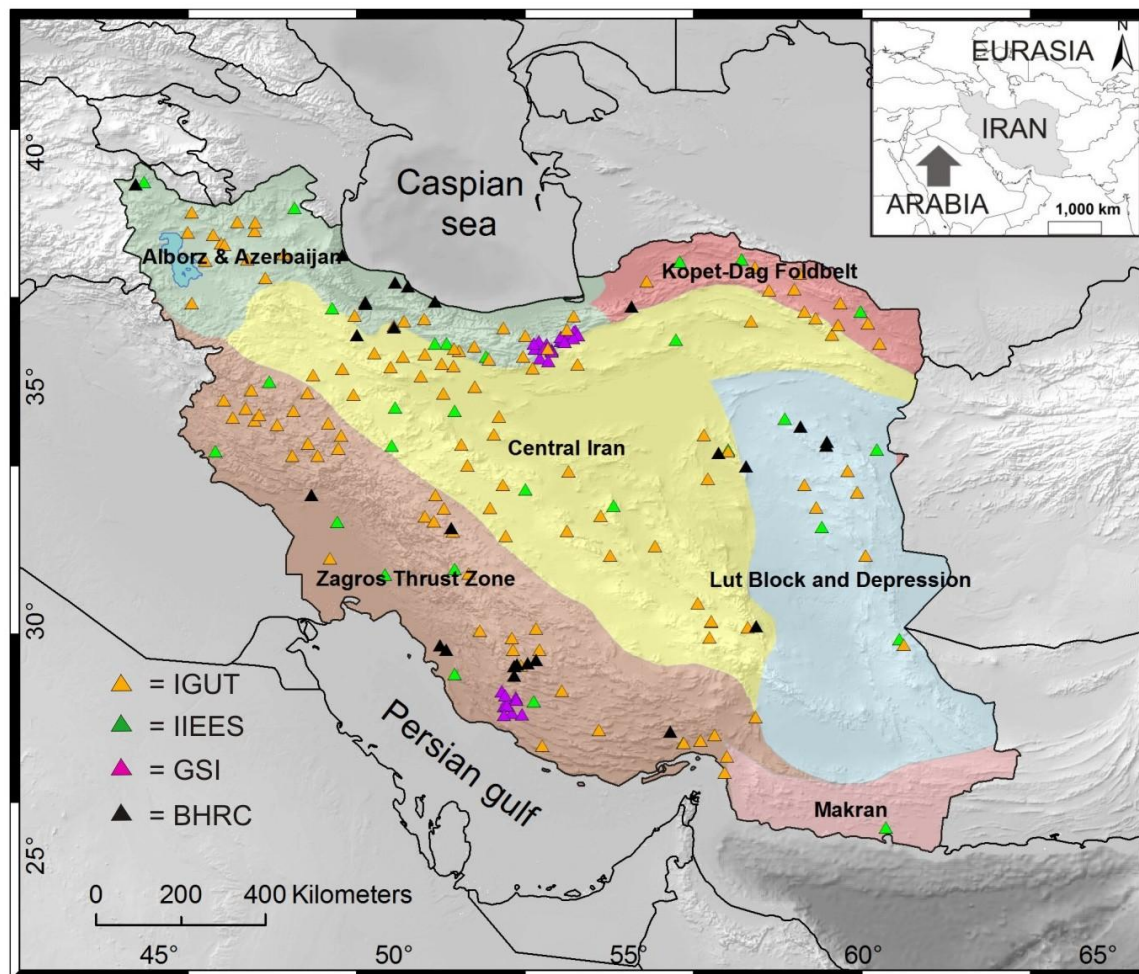
Fig.2.1 Main figure: ASTER shaded relief map showing Iranian seismotectonic blocks (1- Alborz & Azerbaijan, 2- Central Iran, 3- Zagros, 4- Makran, 5- Lut, and 6- Kopet Dag) and distribution of seismic record stations (for details see Nemati et al., 2013) [42]. IGUT = Institute of Geophysics University of Tehran. IIEES = International Institute of Earthquake Engineering and Seismology. GSI = Geological Survey of Iran.BHRC = Building and Housing Research Center.Inset: Location of the study area between Arabia and Eurasia plates.

2.2.2 Seismic Networks

In this study Iranian seismic stations (206 stations) are divided into 4 groups according to their operating organizations (Fig. 2.2). 1- The IGUT seismic network belongs to the Institute of Geophysics in the University of Tehran established in 1995 (120 stations with sub-networks). The main purpose of the network is fast and reliable announcements of both magnitude and location of earthquakes happening all around the country due to fair coverage of the stations. Stations in the IGUT network are equipped with three-component short-period SS1 seismometers and each sub-network has a Global Positioning System (GPS) receiver for timing. Thus, plenty of weak-motion waveform dataare providedthrough the short-period local seismographs (Motaghi and Ghods,

2012) [39]. As well as, earthquake catalog and instant information of earthquakes greater than M=1 can be obtained from the website (http://irsc.ut.ac.ir/). 2- The IIEES broad band network with 30 stations has been established by the International Institute of Earthquake Engineering and Seismology (1998) for mainly research purposes (e.g. monitor seismicity of the country, estimation of crustal velocity models, and study source characteristics). The stations in the IIEES network all are equipped with Güralp CMG-3T sensors, 24-bit CMGDM24 digitizers and GPS receivers. All the current broadband stations are powered by the 220V national electrical network. The developing network will benefit solar array power in order to reduce electrical power demand in the future. Information about earthquake seismic waveforms with magnitude greater than 4.5 and earthquake catalog are available on the website of the IIEES (www.iiees.ac.ir/english) (Ansari and Amini Hosseini, 2014) [4]. 3- The Geological Survey of Iran (GSI) temporarily operated 30 stations in north and south of Iran mostly for special purposes in Alborz and Zagros blocks to study the variability of ground motions (Fig. 2.1) (Nemati et al., 2013) [42]. 4- The strong motion network in Iran belongs to Building and Housing Research Center (BHRC). During the initial operation between 1973 and 1991, the network consisted of 274 accelerometers, but currently the number of total active stations is around 1140. Majority of the stations in the BHRC network are equipped with the solid state accelerometers SSA-2, with 3 channel digital recording sensors (Mirzaei and Farzanegan 2003) [37]. Once using the aggregation of microtremore measurements and wave velocity profiles (V_s and V_p), Zare et al. (1999) [59] presented a site characterization of 26 BHRC stations. In this study characterization of the stations selected by Zare et al. (1999) [59] are only taken into consideration.

Over 80% of the current stations have been installed in highly populated Alborz & Azerbaijan, Central Iran and Zagros blocks (Fig. 2.2). This distribution is based on the tectonic setting of Iran and the higher seismicity of these blocks. Nevertheless, the number of broadband stations is not sufficient for seismic monitoring of other parts of Iran especially in NW and NE Iran. The IIEES has a network-developing plan which indicates that for a better monitoring of earthquakes (M > 2) in thenetwork, for each magnitude increment the average maximum station distance is calculated to be 200km and the minimum number of stations for $0.2° \times 0.2°$ grids should be 100 stations in the future (Ansari and Amini Hosseini, 2014) [4].
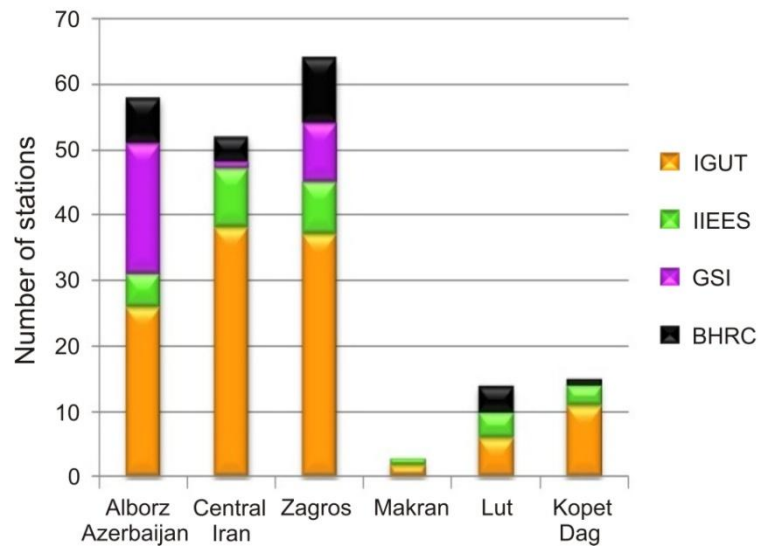
Fig.2.2 Number of distributed stations in each seismotectonic blocks. IGUT = Institute of Geophysics University of Tehran. IIEES = International Institute of Earthquake Engineering and Seismology. GSI = Geological Survey of Iran. BHRC = Building and Housing Research Center.

2.3 Materials and methods

2.3.1. Topographic Amplification Factor (TAF)

At each epicenter, so called "source effects" are the focal mechanism, size and direction of wave propagation (Allen and Gerald, 2007) [2]. The produced seismic waves after seismic activity start to travel through a medium that affect the amplitude and damping shear wave velocity of the propagating seismic waves and they eventually are affected by soil conditions, near-surface geology, and topography when they reach to the Earth's surface (Anggraeni, 2010) (Fig.2.3) [3].
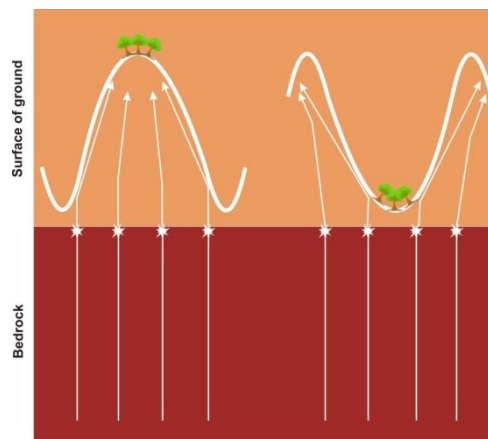
Fig.2.3 Schematic definition of topographic amplification/damping for seismic waves reaching to the surface of ground.

As discussed, the Topographic Amplification Factor (TAF) due to irregular shape of the Earth could be one of the reasons of seismic wave amplifications beside other factors like near-surface geology and etc. Severalstudies have been done about TAF effects, for instance through field experiments (Davis and West, 1973) [14] and analysis of instrument records (Celebi, 1987) [12]. Also remote sensing data have been used for TAF effects and the obtained results prove that seismic waves are dispersed at the topographic discontinuities, leading to amplification of seismic response at some ridges (Pessina and Fiorini 2014) [45]. From an observational perspective, TAF is usually mixed with near-surface geology effects, thus it is often difficult to separate amplification phenomenon to separate factors. In order to improve previous studies some simulated approaches were carried out by using finite element and boundary element methods (Geli et al., 1988) [18]. However, these methods suffer from some drawbacks like one-dimensional results and simple modeling. Athanasopoulos et al. (1999) [5] and Boore (1972) [7] suggested more complex-realistic models using finite elements methods in computational techniques could be used for the simulation of wave propagation. However, memory use of processing and timing were not reasonable. Because of the above-explained reasons, standard seismic building codes have usually neglected the TAF effects. Among the few codes containing TAF, the Eurocode8 recommends S_T as the frequency-independent amplification factor which was adopted by the Italian seismic code into four classes of topographic amplification based on the height and the slope angle (Table 2.1). Identification of T3 and T4 classes would not be possible using straight ArcToolbox functionsbecause ridge and crest positions are trickier and more complex. Thus, for identification of ridge areas, a multi-function procedure (i.e. Focal Statistics, Flow Direction and Flow Accumulation, Block Statistics, Con, Thin and Reclassify) or an extension like what Pessina and Fiorini (2014) [45]presented is needed.

Table 2.1 Topographic Amplification Factor deduced from Eurocode 8 and Italian code (Cauzzi et al., 2012) [11].

Topographic classes	Description	Amplification factor
T1	Flat surface; isolated slopes and cliffs with average slope angle i < 15∘	1
T2	Slopes with i > 15∘	1.2
T3	Ridges with crest width significantly less than the base width and 15∘ < i < 30∘	1.2
T4	Ridges with crest width significantly less than the base width and i > 30∘	1.4

2.3.2 Elevation data

New advances in remote sensing technologies have made available Digital Elevation Models which form topographical data for scientific objectives including hydrology, geology, civil

applications and seismology. SRTM 90m is one of the frequently used DEMs including elevation data over 80% of the Earth's land area (Nikolakopoulos et al., 2006) [40]. Karimzadeh et al. (2014) [29] used a couple of influential local parameters including ASTER topography map for simulation of ground shaking map in Tabriz, Iran. Hestholm et al. (2006) [23] used an elevation model for simulation of a moving source along the locally steep surface topography. Ma et al. (2007) [32] investigated effects of large-scale surface topography on the near-fault ground motions by simulating a M=7.5 earthquake on the Mojave segment of the Andreas fault, the San Gabriel mountains played a natural insulator role for Los Angeles. Simply put, the large-scale topography (e.g. mountains) can protect some areas from ground shaking and scatters surface waves. However a counterexample of the San Gabriel mountains could be possible, even canyons or other features could affect the propagation of seismic waves but evidently the crests or the hills mostly amplify seismic waves rather than scattering in small scales. Sensitivity analyses through GIS extensions to verify the correlationbetween the ridge calculation and the raster resolution were carried out and the validation of the results have proven that a realistic morphological identification and proper description for seismic stations are directly associated with DEM resolution (Pessina et al., 2010; Pessina and Fiorini, 2014) [44, 45]. De Reu et al. (2013) did a topographic classification for a geo-archaeological project in NW Belgium using a DEM-based analysis on high-density LiDAR (Light Detection And Ranging) data between 2001 and 2004. Ridge assessment on DEM with different resolutions ($10*10$ m^2, $20*20$ m^2 and $40*40$m^2) was carried out by Pessina and Fiorini (2014) [45] and an ad hoc GIS tool (multi-function procedure via ArcToolbox) was created for the fast detection of ridges using ASTER data in Italy and Switzerland. Noticeable specifications of ASTER data for researchers like multiple imagery over the same area, convenient access and high-resolution near-global coverage makes it different than other elevation data sources. The ASTER database is comprised of 22600 tiles and in this paper over 300 ASTER GDEM V2 (1°-by-1°) tiles for land facet evaluation of Iran using an extension tool of ArcGIS are freely obtained and merged together using a georeferenced mosaicking tool for covering of the whole study area (http://gdem.ersdac.jspacesystems.or.jp). Each GDEM tile bin provides two files, an elevation model file and a quality assessment (QA) file. Both files comprised of 3601*3601 matrices, corresponding to the 1°-by-1° data area. The mosaic-output (30m posting) created for entire Iran is oriented to the WGS84 and Earth Gravitational Model 96 (EGM96) in GeoTiff format.

2.3.3 Topographic Position Index (TPI) and data processing

Known as Topographic Positioning Index (TPI),has a clever and simple algorithm which measures the difference between elevation of a central cell of a DEM (Z_0) and the average

elevation value of the neighborhood around the cell ($\bar{Z}$) according to a radius (R) which is defined by user's purpose (Fig. 2.4) (Gallant and Wilson, 2000; Weiss, 2001) [17, 57]:

$$TPI = Z_0 - \bar{Z} \qquad (2.1)$$

$$\bar{Z} = \frac{1}{n_R} \sum i \in R^{Z_i} \qquad (2.2)$$

Positive values depict that the central cell is higher than its surrounding and negative values depict that it is lower. The higher-cell or lower-cell along withthe slope of the cell can be used to classify the cell into slope positions. If it is considerably higher than the surrounding neighborhood, then it is likely to be at/or near the top of a hill or ridge. On the contrary, significantly low values mean that the cell is at/or near the bottom of a valley. TPI values close to zero represent either a flat area or a mid-slope area, so the cell slope can be used to distinguish the two. The range of TPI values also depends on R values (Grohmann and Riccomini, 2009) [20]. Large R values mainly reveal major landscape units, while smaller values highlight smaller features, such as minor valleys and ridges. Thus, TPI basically depends on the scale of the projects (Fig. 2.4). For example the same point at the crest of a mountain might be considered a ridge to a highway construction project or a flat surface to a benchmark station construction. The classifications produced by this tool depend entirely on the scale you use to analyze the landscape (Jenness et al., 2013) [26]. Therefore in order to characterize the record stations in Iran territory, a small-scale project has been assumed and coefficient factor in all stations is considered to be one (Fig.2.4). Although different algorithms and techniques are suggested for topographic classifications (Burrough et al., 2000; Iwahashi and Pike, 2007; Hengl and Reuter, 2009) [9, 25, 22], but this study goes through the presented method of Weiss (2001) [57] which classifies the landscape into six discrete slope position classes (1- ridge area, 2- upper slope, 3- steep slope, 4- gentle slope, 5-lower slope and 6- valley) using a Standard Deviation (SD) of TPI (Table 2.2).

For the study area, the grid processing consists of spatial pixels extracted from ASTER data for ridge areas is considered irrespective of secondary hazards. Usually the TPI analysis can be done within a normal physical memory (or RAM) but this may not always be possibleafter merging a large number of ASTER tiles into one large GeoTiff image which represent relatively complex features that contain millions of pixels (columns = 79206 and rows = 68402). In other words, the out of memory error is a common error during large geo-processing. This issue can be solved using a powerful computer with 64GB memory (RAM), multi-core (quad-core-i7) processing and a 1TB HDD to make a suitable interaction between elevation data and TPI analysis (e.g. for data loading into ArcGIS environment, geo-processing and results storage) (Fig. 2.5). The TPI raster was calculated using a circular style for 50m and 100m neighborhood sizes (Fig. 2.4) (see Jenness et al., 2013 [26] for different neighborhood styles) and the results for six classes are presented in the next section.

$$\overline{Z} = \frac{1}{n_R} \sum i \in R^{Z_i}.$$

$$R \sim 50\,m\,;100\,m$$
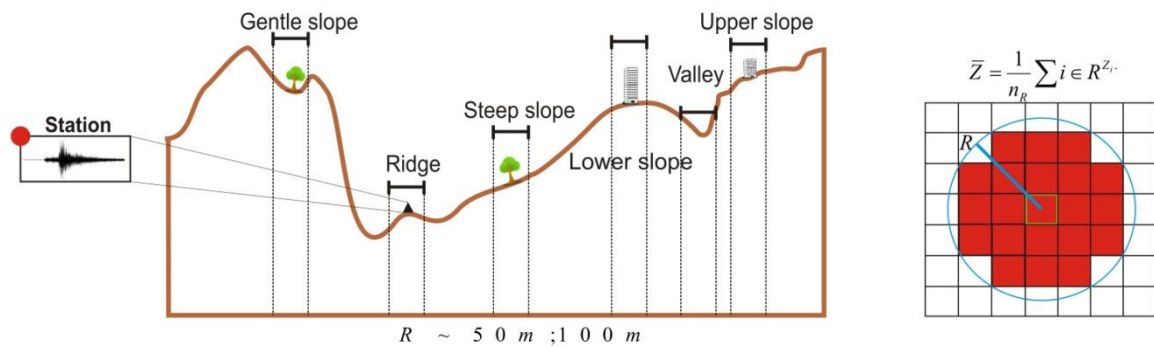
Fig.2.4 Left figure: Schematic definition of a small-neighborhood topographic position classification based on Weiss (2001). Right figure: An example of a circular neighborhood defined by a specific radius length for TPI analysis.

Table 2.2 Classification of the landform into slope position classes based on Weiss (2001).

Landform classification	Description
Ridge	$Z_0 > 1SD$
Upper slope	$SD \geq Z_0 > 0.5SD$
Steep slope	$0.5SD \geq Z_0 \geq -0.5SD$ and slope $> 5\circ$
Gentle slope	$0.5SD \geq Z_0 \geq -0.5SD$ and slope $\leq 5\circ$
Lower slope	$-0.5SD > Z_0 > -1SD$
Valley	$Z_0 < -1SD$
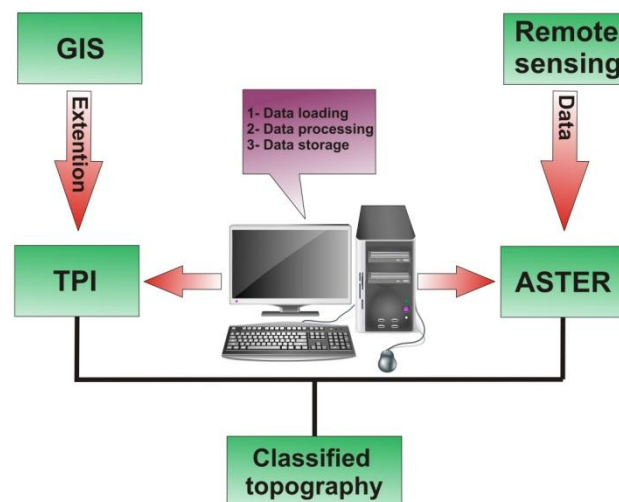
Fig. 2.5 Semi-automatic flowchart of topographic classification structured by remote sensing and GIS.

2.4 Results and discussions

Fig. 2.6 shows the statistical results in percentage terms of the topographic positions and effects of neighborhood radius on topographic classification. The valley and ridge are the largest categories with percentages ranging between approximately 31% (50m), 36% (100m), 31% (50m) and 33% (100m) respectively. For radius 50m, the rest of the categories are lower slope (5%), gentle slope (22%), steep slope (4%), upper slope (7%) and for radius 100m each of the four categories are 4%, 17%, 7% and 3% respectively. By increasing the radius of 50m to 100m, the trend lines move down for lower, gentle and upper slopes. The ridge and valley categories mostly are detected in the Alborz & Azerbaijan, Zagros and Central Iran block due to the mountainous nature of these blocks. Nevertheless, some categories were not recognized very well. For example unexpected lower percentage of lower or gentle slopes in Lut and Central Iran blocks which contain two main deserts of Iran remains a question why these categories were not detected properly. It seems that for both radius sizes (50 and 100m), detectable lower slope is unsatisfactory and it depends to the extent of certain landscape features.
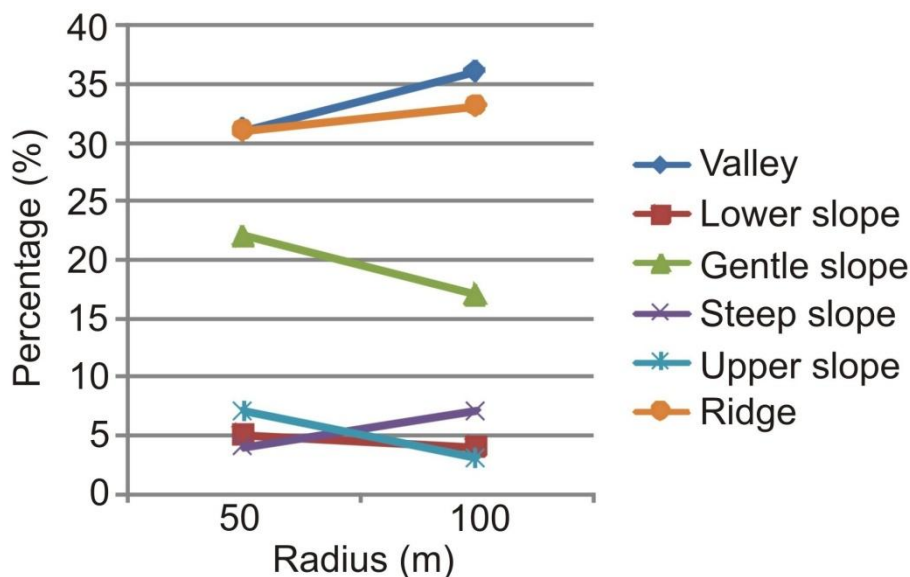
Fig.2.6 Percentage of topographic position classes based on TPI analysis for radii 50m and 100m.

Individual analysis of the landscape in radius size 50m shows that for IGUT stations, about 43% of the stations are classified as gentle slopes, 18% as ridges, 16% as upper slopes. Twenty-three percent of the remaining stations are distributed between valley, lower slope and steep slope classes. At the same radius, 43% of the IIEES stations are classified as ridges, 13% as lower slopes, 13% as gentle slopes and the rest of the stations are distributed between the remaining 3 categories (valley, steep slope and upper slope). At the GSI network (with almost homogeneously distribution between recognized categories), thirty-three percent of the stations are classified as valleys, 20% as gentle slopes, 17% as ridges, 13% as steep slopes, 10% as upper slopes and 7% as

lower slopes (see details in Fig. 2.7). Overall, 23% of the all stations are located in ridge areas based on TPI analysis with 50m radius. The ridge position manifests itself in the radius 100m more than radius 50m, so that 72.5% of the IGUT stations are recognized as ridges. At the IIEES network, 63% of the stations are placed in ridge positions. But at the GSI network, 57% of the stations are recognized as valleys, 20%, 13%, 7%, and 3% are classified as ridges, steep slopes, upper slopes and lower slopes respectively. As said before, TPI is a scale-dependent analysis and generally as the neighborhood size (radius) changes, the obtained results also change. Although the chosen radii (50m and 100m) are small-scale, the interpretation of the classified stations depends on defined ground motion equations and standard procedures used in station implementations. In the BHRC network, the upper slope stations and the steep slope stationswere the largest categories (27% and 19%) (see details in Fig. 2.7).
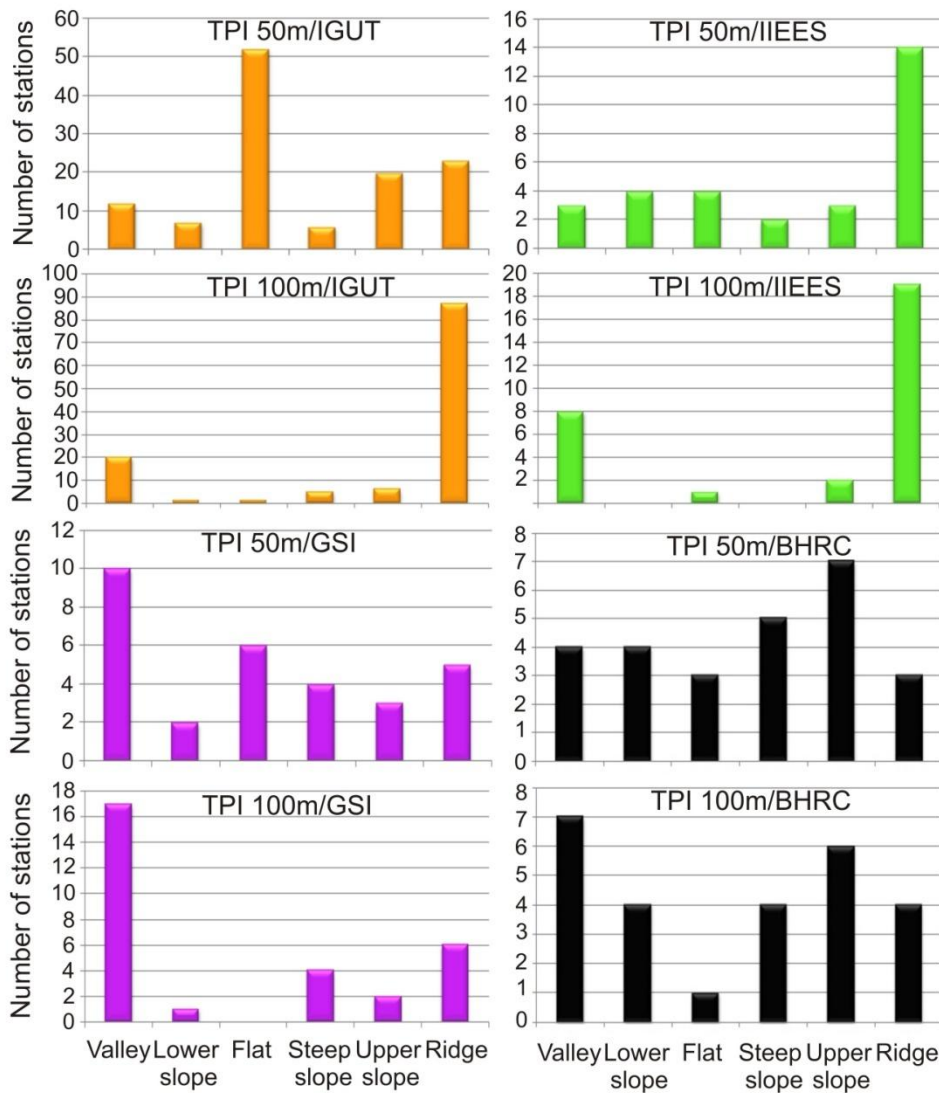
Fig.2.7 Number of seismic stations based on TPI analysis for different topographic position classes and different neighborhood sizes (50m and 100m).

Fig. 2.8a illustrates the number of classified stations, showing different classification at each seismotectonic block for TPI 50m. At each of the high populated blocks (Alborz & Azerbaijan, Central Iran and Zagros) most of stations are placed on flat position. For example at the Alborz & Azerbaijan block, 19 stations (~ 37%) are classified as flat position, of which 12, 2 and 5 stations belong to the IGUT, IIEES and GSI respectively. Twelve stations are classified as valleys, of which 2 stations belong to the IGUT, 1 station belongs to the IIEES and 9 stations belong to the GSI. Only 9 stations are located on ridge areas (5 IGUT, 2 IIEES and 2 GSI stations). In Central Iran, 16 stations (~33%) are classified also as flat position, of which 14 stations belong to the IGUT and 2 stations belong to the IIEES and also 9 out of the 11 stations which are located in ridge areas, belong to the IGUT and 2 of them belong to the IIEES. At the Zagros block also flatand ridge stations are dominant, 21 stations (~ 39%) are classified as flat position of which 20 out of 21 are IGUT stations and 1 is a GSI station. The number of ridge stations is 13 of which 6 stations belong to the IGUT, 4 stations belong to the IIEES and 3 stations belong to the GSI. Additionally it should be noted that each of the other three blocks (Makran, Lut and Kopet dag) have fewer stations, mostly the stations are located on ridge areas. Although the number of "ridge stations" increases in TPI 100m for each of six blocks due to scale-dependent nature of TPI analysis but this trend is more observable in major blocks of which in the Alborz & Azerbaijan block 55%, in Central Iran 66%, in Zagros 66% of the stations are located on ridge positions. The individual comparison of the TPI 50m and TPI 100m for each of the IGUT, IIEES and GSI networks illustrates that the number of "ridge stations" has been increased 29.5%, 20% and 3% respectively. The most variable or even uncertain categories in the IGUT stations are the flat position, decreasing from 43% (50m) to 1% (100m) and the ridge positions, increasing from 19% (50m) to 73% (100m). Also the most variable position of seismic stations of TPI categories in the IIEES and GSI stations are the lower slope and flat position (decrease from 13% to 0% and 20% to 0% respectively) and the valley, which increases from 10% to 27% and 33% to 57% respectively. The most stable categories in the IGUT network are the lower slope decreasing from 5% to 1% and steep slope increasing from 1% to 4%. Also in the IIEES and GSI stations, the most stable categories are steep and upper slopes. In the IIEES network, steep and upper slopes only vary 7% and 3% respectively.This percentage for GSI stations is 0% and 3%, which shows that the classified outputs are much more close to the local topographic reality.However, after TPI neighborhood size consideration, a drastic change between the number of stations in flat and ridge positions has been observed in the Alborz & Azerbaijan, Central Iran and Zagros blocks, while in Makran, Lut and Kopet Dag blocks, the number of stations does not change drastically (Fig. 2.8a and b) (more details are presented at Table 4.3 in Appendix 1).
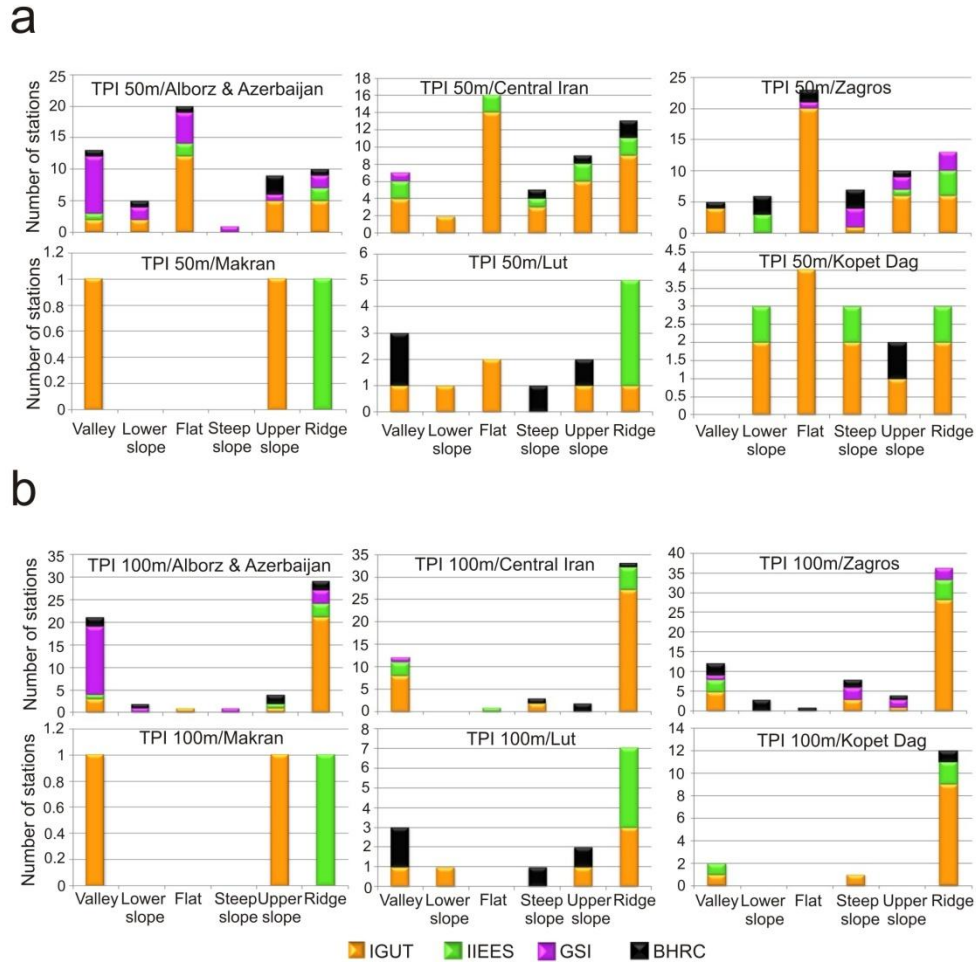
Fig. 2.8 Number of seismic stations based on TPI analysis for different topographic positions at each seismotectonic block (neighborhood size: 50m and 100m).

The V_s^{30} (average shear wave velocity) is an important factor in site characterization which can be estimated either from borehole measurements or indirect methods like topographic data. A regular borehole dataset of the stations is lacking. Thus, the V_s^{30} map of Iran derived from topographical data based on Iranian seismic codeis used for direct testing of the correspondence with topographic slope positions (valley, lower slope, flat, steep slope, upper slope and ridge) at 206 locations (Fig. 2.9) (Wald and Allen, 2007) [56]. We do not expect a physical relationship between two dependent variable (TPI and V_s^{30}). Rather, we present the percentage of topographic slope and V_s^{30} values for each class ($V_s^{30} \cap Slope$) (Fig. 2.10). As shown in Fig. 2.10a and b, there is no recordings associated with soft soils (class IV < 175 m/s), thus the percentages of only three classes for each network is presented. In the GSI network, 17%, 63% and 20% of the stations are located in classes I, II and III respectively. In the IGUT network, classes I, II and III represent 14%, 72% and 14% of the total database respectively. In the IIEES network, 13%, 73% and 14%

of the whole stations are located in classes I, II and III respectively. As with the previous networks, in the BHRC network, the majority of the stations are located in class II (65%) while the remaining stations are placed in class III.
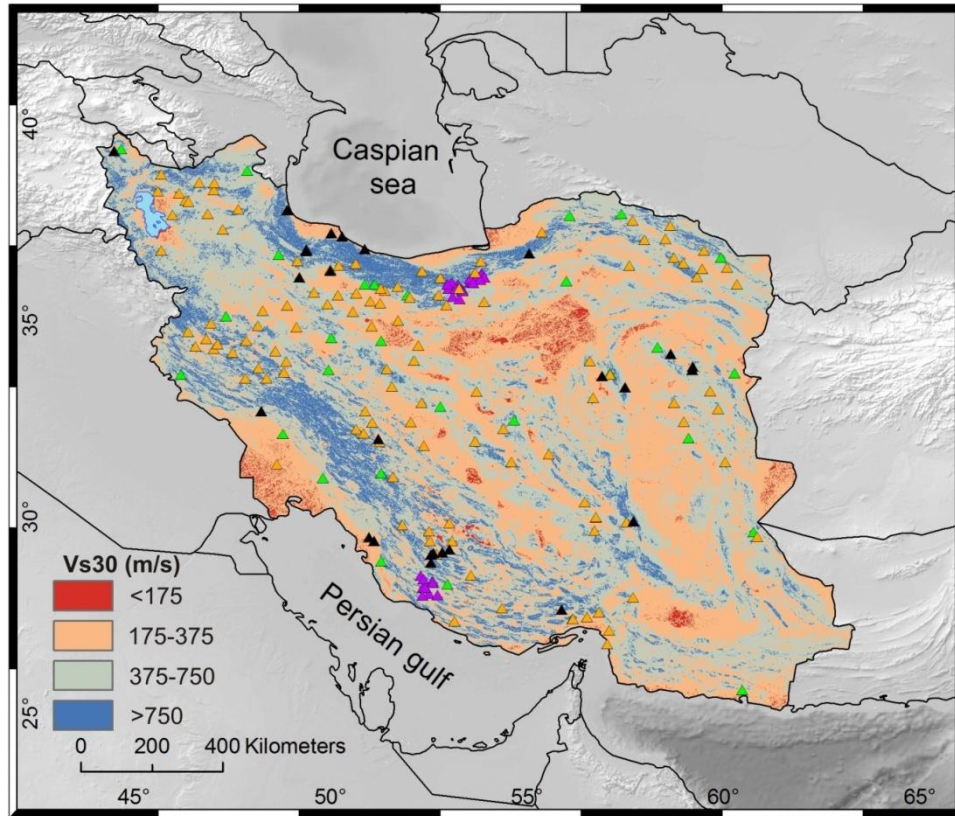
Fig. 2.9 V_s^{30} map of Iran derived from topographic slope (Wald and Allen, 2007) [56].
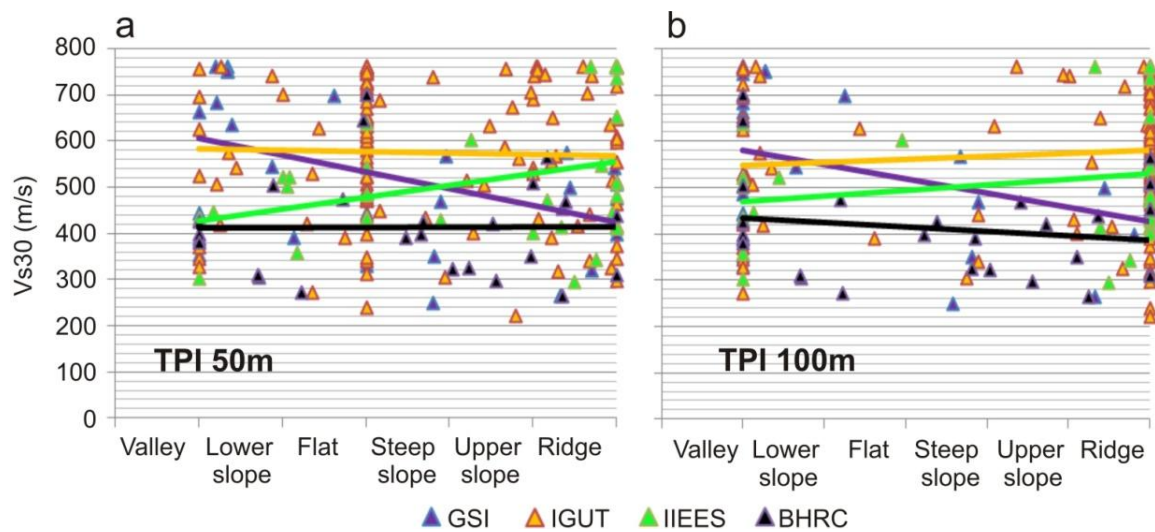
Fig. 2.10 Comparison of V_s^{30} (m/s) and topographic slope positions (a) in TPI50m and (b) in TPI100m.

Lines are individual linear regressions for the V_s^{30} for each network.

After landform classification of the study area, the cells of Voronoi diagrams by central location of the seismic stations (for the IGUT and IIEES networks) are presented in Fig. 2.11. These diagrams are dividing the entire study area into a number of regions (Voronoi tessellation), assuming the existing stations as"seed points". In other words, for each seed (a set of points) there will be a corresponding region consisting of all points are close or closer to the center of that seed than to the center of any other seed in the distribution. The diagrams allow us to establish new stations based on seed stations, more convenient and flexible to develop systematic seismic networks in the future. For example, the cells with varying sizes and complex distributions are identified in terms of topographic positions for both the IGUT and IIEES networks.
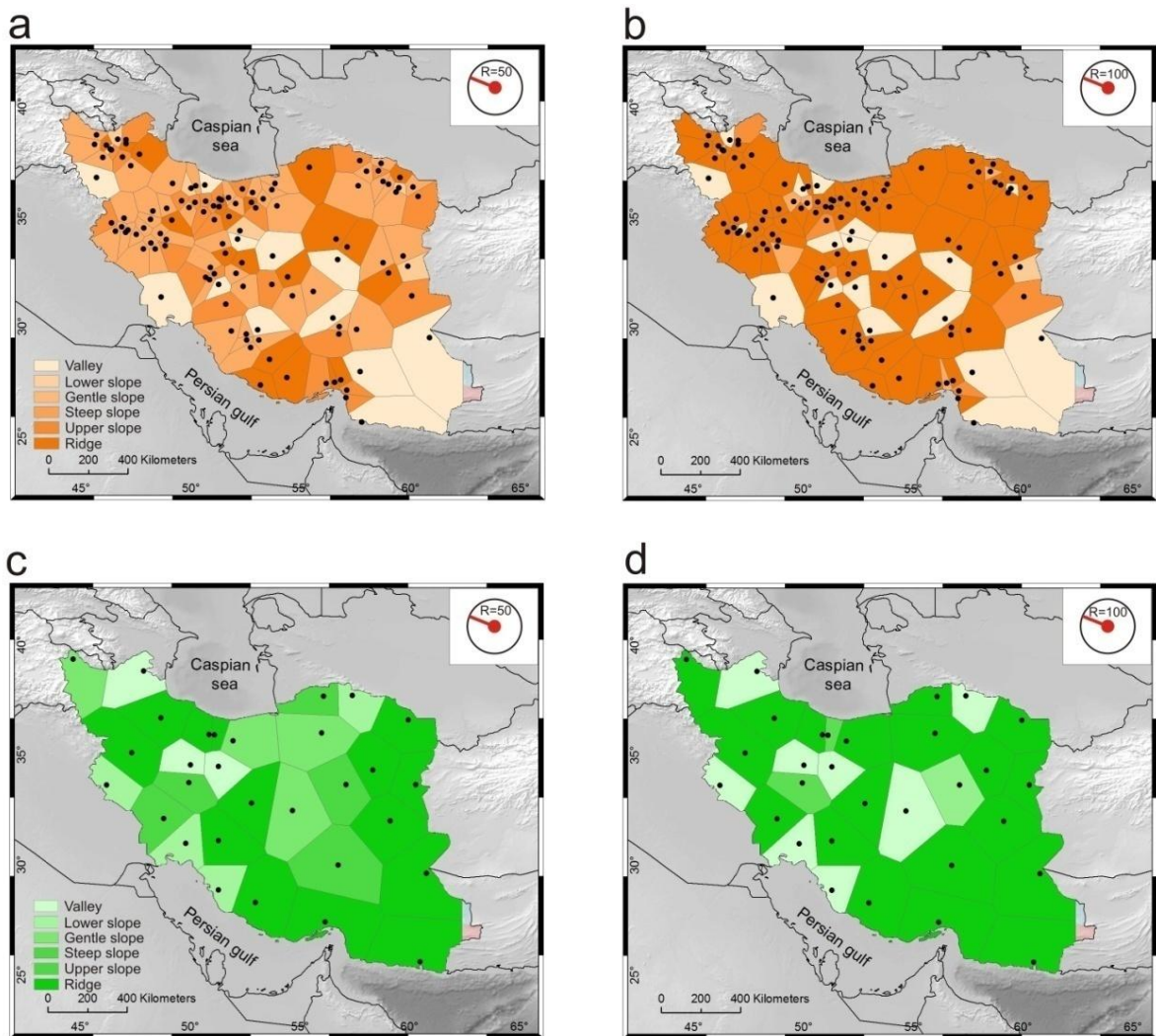
Fig.2.11 (a) and **(b)** Voronoi polygons of IGUT network (R = 50m and 100m) and **(c)** and **(d)** Voronoi polygons of IIEES network (R= 50m and 100m), corresponding black dots show center of Voronoi polygons (seismic station).

2.5 Summary and conclusion

Understanding and defining the seismic network's goal is the first and most important step toward establishing a physical network. The defined goal for each seismic network can differ significantly. For example the IGUT network provides weak-motion waveform data from the short-period local seismographs while less-densely the IIEES network provides complete seismic information from about 0.01 Hz to 50 Hz and therefore allows a much broader range of studies than the short-period records. The GSI network's main purpose was the monitoring of general seismicity (e.g. monitoring of special seismotectonic features, of important civil engineering structures, of man-induced seismicity and etc.). Also, the number of required stations depends on the background noise of the stations, relative signal strength, seismometry, recording equipment, processing techniques, and analysis procedures. Ansari and Amini Hosseini (2014) [4] presented an optimum configuration of IIEES stations through the number of stations in different radii of each hypothetical event and corresponding azimuthal gap for understanding of the network coverage. This paper also suggested a new network configuration of IGUT and IIEES networks through Voronoi diagrams and land classifications. The large size of the digital elevation model limited our analysis between TPI50m and TPI100m whilefor optimum results in TPI analysis,the wide range of neighborhood sizes from 50m to 1500m has to be taken into account. The correlation of the topographic slope position map and V_s^{30} map indicates majority of Iranian stations are located in soil classes II and III, regardless of which seismic network they belong to. Information of characterized stations could open new ways for seismology engineers toimprove the formulation of new ground motion prediction equations with respect to topographic position of record stations and topographic amplification factor.This paper also suggested a new network configuration of the IGUT and IIEES networks through Voronoi diagrams and land classifications. The Voronoi tessellations generated by central location of seismic stations would be a better idea for establishing new stations according to the mentioned criteria and taking their topographic positions into account. Once the information of the classified topography of the region through the Voronoi distribution, their location and their description is provided, determination of minimum number of stations required to cover the entire country would be much easier.

Generating TPI maps using accurate DEMs with different radii is one of the useful/fast approaches for landscape characterization and slope position classification. In this paper for characterization of the record stations, at the first step TAF assumed as an independent site effect in Iranian seismic networks, then using a merged ASTER data, a TPI classification carried out under defined criteria by Weiss (2001) which classifies the landscape into six discrete slope position classes. A circular neighborhood method by a radius length extending outward from the cell center has been used for TPI raster maps. In this study various radii from 50m to 1000m (50m increment) were tested but for seismological purposes only radii 50m and 100m were taken into account. As shown in Fig. 2.12, the ridge position manifested itself in radius 100m more than

radius 50m. By increasing the radius, the number of "ridge stations" increased which means that the TPI is entirely a scale-dependent approach. The TPI results are the first topographic classification of the study area that shows that the valley and ridge classes were the largest categories in Iran territory for both 50m and 100m radii. Although these classes were detected well in the Alborz & Azerbaijan, Central Iran and Zagros blocks lower/gentle slopes are not detected well in the Lut and Central Iran which shows TPI analysis has some shortcomings for detection of more complex textures.
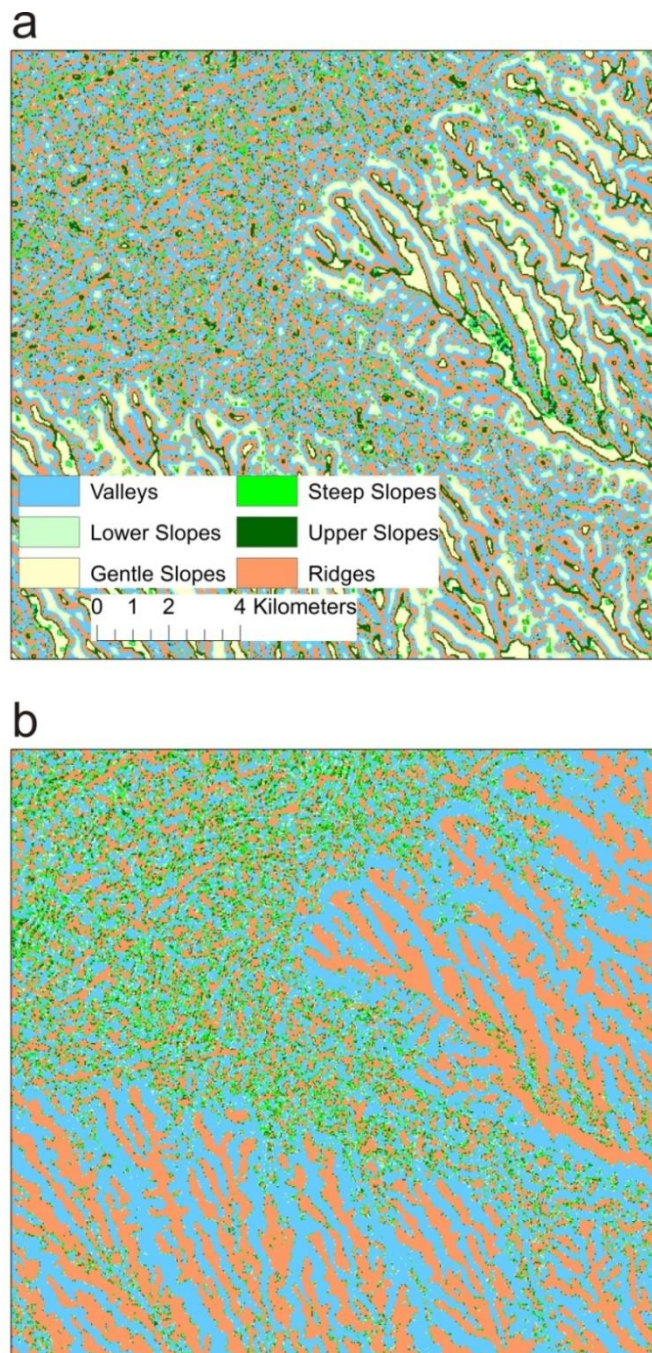
Fig. 2.12 Distribution of topographic positions with TPI analysis for **(a)** radius 50m and **(b)** radius 100m.

References

[1] Aghanabati, A., 2004. Geology of Iran.Geological Survey of Iran press, Tehran, Iran p. 586.

[2] Allen, R.M., Gerald, S., 2007. Earthquake hazard mitigation: New directions and opportunities, In "Treatise on Geophysics". Elsevier 4, 607–648.

[3] Anggraeni, D., 2010. Modelling the impact of topography on seismic amplification at regional scale.Ph.D thesis, ITC, Netherlands.

[4] Ansari, A., Amini Hosseini, K., 2014. Broadband Seismic Network of Iran and Increasing Quality of Seismic Recordings. Seismological Research Letters 85, 878–888.

[5] Athanasopoulos, G.A., Pelekis, P.C., Leonidou, E.A., 1999. Effects of Surface Topography on Seismic Ground Response in the Egion (Greece) 15-6-1995 Earthquake. Soil Dynamics and Earthquake Engineering, 18, 135–149.

[6] Berberian, M., 2014. Earthquakes and Coseismic Surface Faulting on the Iranian Plateau, Part II: Dynamic Phenomena Associated with the Earthquake on the Iranian Plateau. Elsevier publications.

[7] Boore, D.M., 1972. A note on the effect of simple topography on seismic SH waves, Bulletin of the Seismological Society of America. 62, 275–284.

[8] Booth, B., Mitchell, A., 2001. Getting Started with ArcGIS™, ESRI publications 124–128.

[9] Burrough, P.A., van Gaans, P.F.M., MacMillan, R.A., 2000. High-resolution landform classification using fuzzy k-means. Fuzzy Sets and Systems (113), 37–52.

[10] Carpentier, S., Konz, M., Fischer, R., Anagnostopoulos, G., Meusburger, K., Schoeck, K., 2012.Geophysical imaging of shallow subsurface topography and its implication for shallow

landslide susceptibility in the Urseren Valley, Switzerland. Journal of Applied Geophysics 133, 132–142.

[11] Cauzzi, C., Fah, D., Pessina, V., Faccioli, E., Smerzini, C., 2012. Topographic amplification from recorded earthquake data and numerical simulations.and numerical simulations. 15th WCEE, Lisboa.

[12] Celebi, M., 1987. Topographical and geological amplification determined from ground motion and aftershock records of the 3 March 1985 Chile earthquake. Bulletin of the Seismological Society of America 77, 1147–1167.

[13] Chen, H., Lin, G., Lu, M., Shih, T., Horng, M., Wu, S., Chuang, B., 2011. Effects of topography, lithology, rainfall and earthquake on landslide and sediment discharge in mountain catchments of southeastern Taiwan. Geomorphology 133, 132–142.

[14] Davis, L. L., West, L.R., 1973. Observed effects of topography on ground motion. Bulletin of the Seismological Society of America 63, 283–298.

[15] De Reu, J., Bourgeois, J., Bats, M., Zwertvaegher, A., Gelorini, V., De Smedt, P., Chu, W., Antrop, M., De Maeyer, P., Finke, P., Van Meirvenne, M., Verniers, J., Crombé, P., 2013.Application of the topographic position index to heterogeneous landscapes. Geomorphology 186, 39–49.

[16] Drăgut, L., Blaschke, T., 2006.Automated classification of landform elements using object-based image analysis. Geomorphology 81, 330–344.

[17] Gallant, J.C., Wilson, J.P., 2000. Primary topographic attributes. In: Wilson, J.P., Gallant, J.C. (Eds.), Terrain Analysis: Principles and Applications. Wiley, New York, 51–85.

[18] Geli, L., Bard, P.,Jullien, B., 1988. The effect of topography on earthquake ground motion: A review and new results. Bulletin of the Seismological Society of America 78, 42–63.

[19] Giles, P.T., 1998. Geomorphological signatures: classification of aggregated slope unit objects from digital elevation and remote sensing data. Earth Surface Processes and Landforms 23, 581–594.

[20] Grohmann, C.H., Riccomini, C., 2009. Comparison of roving-window and search-window techniques for characterising landscape morphometry.Computers & Geosciences 35, 2164–2169.

[21] Hengl, T., Rossiter, D.G., 2003. Supervised landform classification to enhance and replace photo-interpretation in semi-detailed soil survey. Soil Science Society of America Journal 67, 1810–1822.

[22] Hengl, T., Reuter, H.I. (Eds.), 2009. Geomorphometry: concepts, software, applications. Developments in Soil Science, 33. Elsevier, Amsterdam.

[23] Hestholm, S., Moran, M., Ketcham, S., Anderson, T., Dillen, M., McMechan G., 2006. Effects of free-surface topography on moving-seismic-source modeling.Geophysics,71, 159-166.

[24] Irvin, B.J., Ventura, S.J., Slater, B.K., 1997. Fuzzy and isodata classification of landform elements from digital terrain data in Pleasant Valley, Wisconsin. Geoderma 77, 137–154.

[25] Iwahashi, J., Pike, R.J., 2007. Automated classifications of topography from DEMs by an unsupervised nested-means algorithm and a three-part geometric signature. Geomorphology 86, 409–440.

[26] Jenness, J., Brost, B., Beier, P., 2013. Land Facet Corridor Designer, USDA Forest Service Rocky Mountain Research Station.

[27] Karimzadeh, S., Cakir, Z., Osmanoğlu, B., Schmalzle, G., Miyajima, M., Amiraslanzadeh, R., Djamour, Y., 2013a.Interseismic strain accumulation across the North Tabriz Fault (NW Iran) deduced from InSAR time series. Journal of Geodynamics 66, 53–58.

[28] Karimzadeh, S., Amiraslanzadeh, R., Miyajima, M., 2013b.Quick report of earthquake (Mw7.5) on 16th April, SE Iran. Japan Society of Civil Engineers (JSCE).

[29] Karimzadeh, S., Miyajima, M., Hassanzadeh, R., Amiraslanzadeh, R., Kamel, B., 2014.A GIS-based seismic hazard, building vulnerability and human loss assessment for the earthquake scenario in Tabriz.Soil Dynamics and Earthquake Engineering 66, 263–280.

[30] Liu, J., J. Mason, P., Yu, E., Wu, M., Tang, C., Huang, R., Liu, H., 2012. GIS modelling of earthquake damage zones using satellite remote sensing and DEM data. Geomorphology 139-140, 518–535.

[31] Luo, L., Wang, X., Liu, C., Guo, H., Du, X., 2014. Integrated RS, GIS and GPS approaches to archaeological prospecting in the Hexi Corridor, NW China: a case study of the royal road to ancient Dunhuang. Journal of Archaeological Science 50, 178–190.

[32] Ma, S., Archuleta, R.J., Page, M.T., 2007.Effects of Large-Scale Surface Topography onGround Motions, as Demonstrated by a Study of the San Gabriel Mountains, LosAngeles, California.Bulletin of the Seismological Society of America 97, 2066–2079.

[33] MacMillan, R.A., Pettapiece, W.W., Nolan, S.C., Goddard, T.W., 2000.A generic procedure for automatically segmenting landforms into landformelements using DEMs, heuristic rules and fuzzy logic. Fuzzy Sets and Systems 113, 81–109.

[34] Masson, F., Djamour, Y., Vangorp, S., Chéry, J., Tavakoli, F., Tatar, M., Nankali, H., 2006. Extension in NW Iran inferred from GPS enlightensthe behavior of the south Caspian basin, Earth and Planetary Science Letters 252, 180-188.

[35] McClusky, et al., 2000.Global Positioning System constraints on plate kinematics and dynamics in the eastern Mediterranean and Caucasus.Journal of Geophysical Research.105, 5695–719.

[36] Miliaresis, G.C., Argialas, D.P., 1999. Segmentation of physiographic features from the global digital elevation model/GTOPO30. Computers & Geosciences 25, 715–728.

[37] Mirzaei, H., Farzanegan, E., 2003. Iran Strong Motion Network. Asian Journal of Civil Engineering 4, 173-186.

[38] Mirzaei, N., Mengtan, G., Yantai, C., 1998. Seismic source regionalization for seismic zoning of Iran: major seismotectonic provinces. Journal of Earthquake Prediction Research 7, 465–495.

[39] Motaghi, K., Ghods, A., 2012. Attenuation of Ground-Motion Spectral Amplitudes and Its Variations across the Central Alborz Mountains. Bulletin of the Seismological Society of America 102, 1–13. doi: 10.1785/0120100325

[40] Nikolakopoulos, K.G., Kamaratakis, E.K., Chrysoulakis, N., 2006. SRTM vs ASTER elevation products.Comparison for two regions inCrete, Greece.International Journal of Remote Sensing. 27, 4819–4838.

[41] Neghabat, F., Liu, S.C., 1977.Earthquake regionalization of Iran. Proc. 6th WCEE, Delhi, India 2, 531–536.

[42] Nemati, M., Hatzfeld, D., Gheitanchi, M.R., Talebian, M., Mirzaei, N., Sadidkhouy, A., 2013. Seismotectonic of the Eastern Alborz with a Point of View to the South of Damghan MW=5.7 Earthquake. Scientific Quarterly Journal, Geosiences 22, 87–98.

[43] Nowroozi, A.A., 1976. Seismotectonic provinces of Iran. Bulletin of the Seismological Society of America 66, 1249–1276.

[44] Pessina, V., Fiorini, E., Paolucci, R., GIS-based identification of topographic sites in Italy with significant ground motion amplification effects. In: Proceedings of the 5th international conference on recent advances in geotechnical earthquake engineering and soil dynamics. SanDiego; 2010.

[45] Pessina, V., Fiorini, E., 2014.A GIS procedure for fast topographic characterization of seismic recording stations.Soil Dynamics and Earthquake Engineering 63, 248–258.

[46] Pike, R.J., Evans, A.A., Hengl, T., 2009. Geomorphometry: a brief guide. In: Hengl, T., Reuter, H.I. (Eds.), Geomorphometry. Concepts, Software, Applications.Developments in Soil Science. Elsevier, Amsterdam, 3–30.

[47] Priestley, K., 1992. Regional seismic studies in central Asia.Scientific report No. 1, Philips Laboratory 18–30.

[48] Prima, O.D.A., Echigo, A., Yokoyama, R., Yoshida, T., 2006.Supervised landform classification of northeast Honshu from DEM-derived thematic maps. Geomorphology 78, 373–386.

[49] Raup, B., Kaabb, A., S. Kargel, J., P. Bishop, M., Hamilton, G., Lee, E., Paul, F., Rau, F., Soltesz, D., Singh Khalsa, S.J., Beedle, M., Helm, C., 2007.Remote sensing and GIS technology in the Global Land Ice Measurements from Space (GLIMS) Project. Computers & Geosciences 33, 104–125.

[50] Ren, Z., Zhang, Z., Dai, F., Yin, J., Zhang, H., 2014 Topographic changes due to the 2008 Mw 7.9 Wenchuan earthquake as revealed by the differential DEM method. Geomorphology 217, 122–130.

[51] Song, Y., Gong, J., Gao, S., Wang, D., Cui, T., Li, Y., Wei, B., 2012. Susceptibility assessment of earthquake-induced landslides using Bayesian network: A case study in Beichuan, China. Computers &Geosciences 42, 189–199.

[52] Tavakoli, F., 2007.Present-day deformation and kinematics of the active faults observed by GPS in the Zagros and east of Iran, PHD Thesis.

[53] Tomlinson R.F (1968)A Geographic Information System for Regional Planning.In Land Evaluation Stewart, G.A. (Ed.) 200–210.

[54] Van Sickle J (2004) Basic GIS Coordinates CRC Press LLC.

[55] Vernant, P., Nilforoushan, F., Hatzfeld, D., Abbassi, M.R., Vigny, C., Masson, F., Nankali.H., Martinod, J., Ashtiani, A., Bayer, R., Tavakoli, F., Chéry, J., 2004.Present-day crustal deformation and plate kinematics in the Middle East constrained by GPS measurements in Iran and northern Oman. Geophysical Journal International 157, 381–398. doi:10.1111/j.1365-246X.2004.02222.x

[56] Wald, D., Allen, T., 2007.Topographic Slope as a Proxy for SeismicSite-Conditions (*Vs30*) and Amplification Around the Globe. USGS open report.

[57] Weiss, A.D., 2001. Topographic position and landforms analysis.Poster Presentation, ESRI Users Conference, San Diego, CA.

[58] Yu, L., Porwal, A., Holden, E., C.Dentith., M., 2012. Towards automatic lithological classification from remote sensing data using support vector machines. Computers &Geosciences 45, 229–239.

[59] Zare, M., Bard, P., Ghafory-Ashtiany, M., 1999.Site characterizations for the Iranian strong motion network.Soil Dynamics and Earthquake Engineering 18, 101-123.

[60] Zare, M., Kalantari, A., Ansari, A., Haghshenas, E., Davoudi, M., Mostafazadeh, M., 2012 Reconnaissance report of Varzeghan twin earthquakes (Ahar county - Eastern Azerbaijan) of International Institute of Earthquake Engineering and Seismology (IIEES) (In Persian).

[61] Zare, M., Amini, H., Yazdi, P., Sesetyan, K., Demircioglu, M., Kalafat, D., Erdik, M., Giardini, D., Asif Khan, M., Tsereteli N., 2014. Recent developments of the Middle East catalog. Journal of Seismology 18, 749–772.

3. Initial hazard assessment and coulomb stress changes in NW Iran

3.1 General remarks

The study area is located on the Turkish–Iranian plateau whereongoing Arabian–Eurasian convergence is partitioned betweenthrusts and strike-slip faults in NW Iran and eastern Turkey (Copleyand Jackson, 2006; Jackson, 1992; Fig. 3.1) [12,30]. One major structure is the North Tabriz Fault (NTF) encompassed in a region of intense deformation and seismicity located between two fold-and-thrust belts of the Caucasus to the north and the Zagros Mountains to the south, spanning a length of 150 km in NW-SE direction in NW Iran (Berberian and Arshadi, 1976; Jackson, 1992; Fig. 3.1) [9, 30]. The NTF is located~40–45 km south-southwest of the Ahar region struck by the Mw 6.5 and Mw 6.3 earthquake sequence in August 11, 2012 (Fig. 3.2). Field observations conducted by Geological Survey of Iran show oblique right-lateral strike-slip surface faulting on a WNW-ESE trending rupture, consistent with focal mechanism solutions. Geodetic and paleoseismic studies yield conflicting estimates of shear strain across the NTF (Djamour et al., 2011; Hessami et al., 2003a) [14, 22]. While slip rate estimates based on offset streams and displaced historical structures such as traditional water channels (qanats) and other water pipelines yield 2–4 mm/year right-lateral horizontal movement across the NTF (Hessami et al., 2003a; Karakhanian et al., 2004) [22, 31], GPS measurements suggest much higher slip rates reaching 7–10 mm/year (Djamour et al., 2011; Masson et al., 2006; Reilinger et al., 2006; Vernant et al., 2004) [14, 41, 50, 65]. Fault locking depths could not be estimated with a high level of accuracy due to sparse distribution of the GPS vectors around the NTF and their relatively higher errors due to limited (<4) number of measurements on some campaign sites (Djamour et al., 2011; Masson et al., 2006) (Table 3.1) [14, 41]. The average distance between GPS stations is about 50 km (Djamour et al., 2011) [14].The study area is also ideal for the InSAR technique owing to its arid to semi-arid climate and thus its sparse vegetation cover. We model the InSAR data to deduce the slip rate and locking depth of the NTF using an elastic dislocation model, and present evidence for land subsidence in the Tabriz basin, a large intramountain basin bounded by Lake Urmia to the west and the NTF to the east-northeast between the Zagros and Talysh mountains (Fig. 3.2). The Tabriz basin hosts some important industrial structures, such as a thermal power plant, a petrochemical site and the Tabriz-Miandoab water lifeline, which may be threatened by the subsidence.
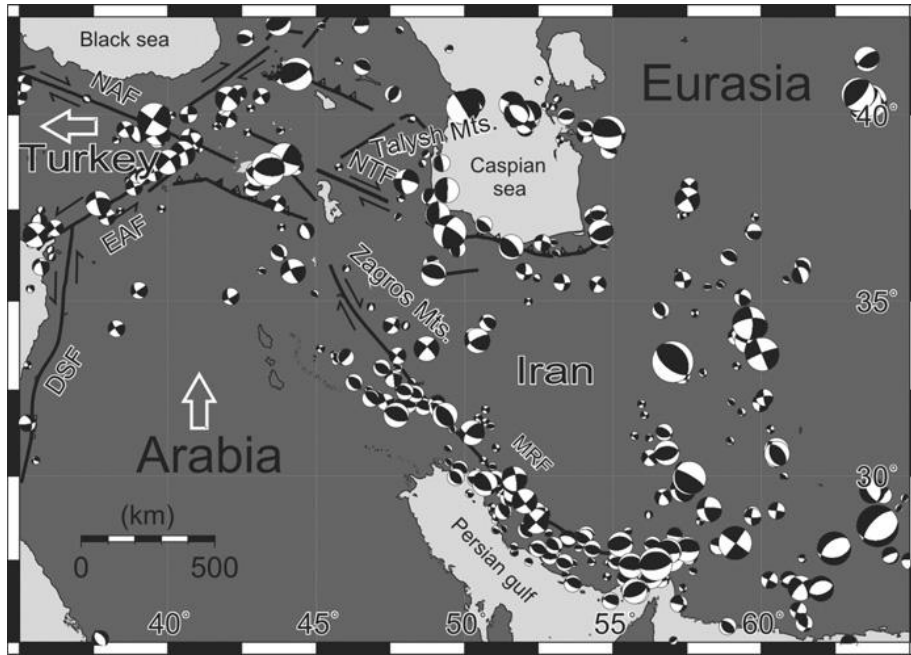
Fig.3.1 Seismotectonic map of the study region. NTF, North Tabriz Fault; NAF, NorthAnatolian Fault; EAF, East Anatolian Fault; DSF,Dead Sea Fault; MRF, Main RecentFault. Simplified major faults (black lines) around the Arabian–Eurasian collisionzone with focal mechanisms ofmajor earthquakes between 1976 and 2012 fromthe Global CMT (http://www.globalcmt.org/). White arrows sketch the motion ofArabian and Anatolian plate relative to Eurasia.
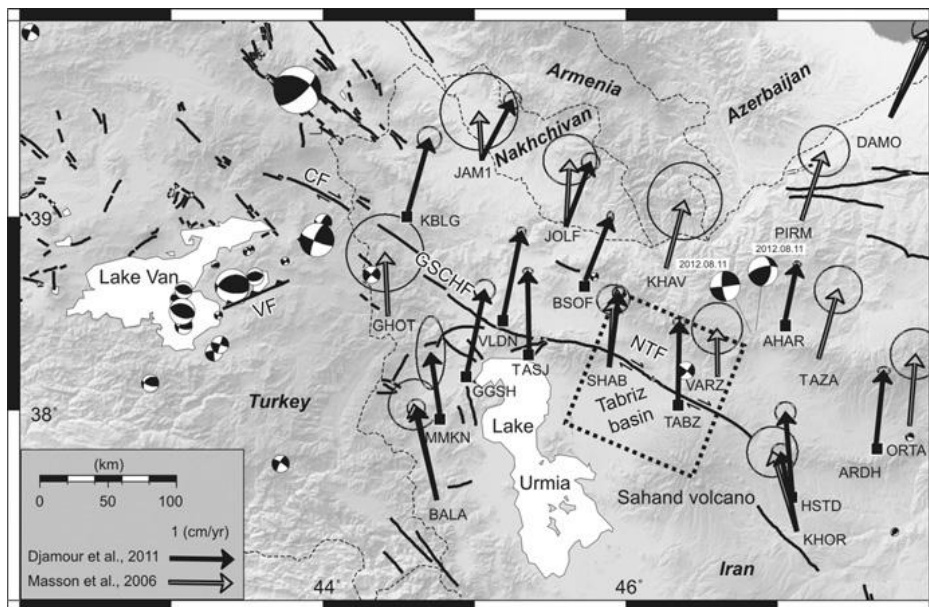
Fig.3.2 Morphotectonic map of the study area within the Turkish–Iranian plateaushowing active faults (black lines), focal mechanisms and GPS velocity fields relativeto Eurasia with 95% confidence ellipses (with 4 letter site names) on shaded relieffrom SRTM-3 arc second data. ContinuousGPS stations are indicated with blacksquares at vector tails. Black dashed square shows the frame of the SAR imagesstudied, covering major part of the Tabriz basin and the NTF. GSCHF, Gailatu-SiahChesmeh-Khoy Fault; VF, Van Fault (2012 Van rupture); CF, Chalderan Fault; NTF,North Tabriz Fault.

Table 3.1 Latitude, longitude, east and north GPS components (V_E and V_N); Corr = correlation coefficient between the east and north uncertainties. (M) = Masson et al., 2006 [41]; (D) = Djamour et al., 2011 [14].

Station name	Lat.	Long.	V_E	V_N	Corr.
AGKA (M)	37.169	48.005	10.8	-1.5	0.02
ARBI (M)	38.477	48.231	11.0	3.5	0.05
ATTA (M)	37.156	50.102	13.5	-2.7	0.03
BADA (M)	36.764	48.814	10.5	-1.7	0.06
BALA (M)	37.534	44.750	15.6	-3.8	0.02
BIJA (M)	36.232	47.930	12.3	-3.7	0.06
DAMO (M)	39.513	47.744	14.3	6.0	0.05
GHOT (M)	38.489	44.428	10.3	-0.5	0.01
HASH (M)	37.764	48.922	10.1	0.2	0.04
JAM1 (M)	39.297	45.049	7.8	-0.5	0.01
JOLF (M)	38.952	45.605	10.9	0.6	0.02
KHAV (M)	38.736	46.265	11.0	3.0	0.02
KHOR (M)	37.368	47.123	13.0	-4.0	0.02
MIAN (M)	36.908	46.162	12.5	-3.5	0.06
ORTA (M)	37.929	47.869	11.5	1.0	0.02
PRIM (M)	38.984	47.157	11.3	3.7	0.02
SHAB (M)	38.228	45.887	10.9	0.7	0.05
TAZA (M)	38.270	47.271	11.2	3.2	0.02
VARZ (M)	38.178	46.603	7.8	-0.1	0.02
BALA (D)	37.534	44.750	15.00	3.38	0.010
GGSH (D)	38.207	38.207	13.15	2.80	-0.002
HSTD (D)	37.576	47.094	13.00	1.10	-0.001
KHOR (D)	37.368	47.123	12.87	-2.63	0.009
MIAN (D)	36.908	46.162	13.54	-2.16	0
MMKN (D)	37.985	44.771	9.88	-1.52	0
MNDB (D)	36.930	46.009	14.59	-4.58	-0.001
SHAB (D)	38.228	45.887	11.98	1.60	0.004
TABZ (D)	38.056	46.343	12.76	0.22	-0.002
JAM1 (D)	39.297	45.049	9.64	5.04	0.003
JOLF (D)	38.952	45.605	10.52	4.01	0.008
SHAB (D)	38.228	45.887	11.98	1.60	0.008
TASJ (D)	38.316	45.361	12.81	-0.27	-0.006
VLDN (D)	38.492	45.193	13.79	2.87	-0.004
AHAR (D)	38.468	47.050	9.13	1.93	-0.006
ARBI (D)	38.477	48.231	11.65	4.53	0
ARDH (D)	37.829	47.650	11.88	1.23	-0.004
BSOF (D)	38.674	45.732	10.31	4.07	-0.004
DAMO (D)	39.513	47.744	13.75	7.15	-0.003
GOSM (D)	38.706	48.419	12.24	5.07	0.003
JERM (D)	39.837	45.661	10.48	5.02	-0.015
KBLG (D)	39.031	44.565	11.90	3.41	-0.002

3.2 Interseismic slip rate of the North Tabriz Fault using InSAR

3.2.1 North Tabriz Fault (NTF)

The NTF is a right-lateral strike-slip fault that accommodates part of the convergence and forms the northern boundary of the Tabriz Basin (TB) with a clear surface expression on the topography (Karakhanian et al., 2004) [31]. It is the southeastern continuation of the Gailatu-Siah Chesmeh-Khoy and Chalderan faults that ruptured in 1976 with a Mw 7.1 earthquake in Turkey near the Iranian border (Fig. 3.2). Although discontinuous, this right-lateral system of strike-slip faults

appears to be the southeastern continuation of the North Anatolian Fault into NW Iran (Djamour et al., 2011; Jackson, 1992; Westaway, 1990) [14, 30, 67]. Historical documents going back two millennia (Berberian and Arshadi, 1976) [9] and instrumental records demonstrate that NW Iran and Eastern Turkey have been struck by numerous destructive earthquakes, the last one being the Mw 7.1, October 23, 2011 Van earthquake associated with reverse slip on a NE-SW trending fault (Akoglu et al., 2012; Fig. 3.2) [3]. Historical documents suggest that the last two large earthquakes on the NTF took place within 60 years in the 18th century on its adjacent segments (Ambraseys and Melville, 1982; Berberian and Arshadi, 1976) [4, 9]. The first event occurred in 1721 and had a magnitude of Ms 7.3. Initiating at 37.90°N, 46.70°E (Berberian, 1994) [8], it ruptured to the southeast along the NTF more than 39 km. The second earthquake in 1780 (Ms 7.4) broke its northwestern section with an epicenter located at 38.12°N, 46.29°E and producing a surface rupture of ~100 km long (Ambraseys and Melville, 1982; Berberian, 1994) [4, 9]. Although the direction and termination of these ruptures are not well known, the epicenters of the events and studies by Karakhanian et al. (2004) [31] suggest that the SAR images analyzed in this study cover most of the 1780 rupture and possibly some sections of the 1721 event (Fig. 3.2). Therefore, the southern segment of the NTF, in particular, poses relatively higher seismic hazard, as it has not produced any large earthquake for nearly three centuries. A future earthquake on any of the two rupture segments would have a large impact for Tabriz as suggested by the historical documents reporting similar damages for the two events (Berberian, 1994) [8]. Unlike most of the studied faults elsewhere in the world (Elliot et al., 2008; Wright et al., 2001) [15, 68], the low interseismic strain accumulation rate along the NTF is challenging.

3.2.2 SAR data and analysis

As already said, the InSAR technique combines radar images of the same region acquired at different times (i.e., repeat pass interferometry) or simultaneously but from a different angle of view (i.e., single pass interferometry) to obtain the interferometric phase, which gives a measure of the radar-to-ground range difference between the two images (Gabriel et al., 1989) [17]. While single pass interferometry is mostly used for constructing digital elevation models (DEM) (i.e., Shuttle Radar Topographic Mission), repeat pass interferometry is generally used for detecting surface movements. More details can be found in several review articles such as Massonnet and Feigl, 1998 and Bürgmann et al., 2000 [10, 43]. Extracting surface deformation that occurred during the time interval covered by the two images in line of sight (LOS) direction requires removal of the phase contributed by topography and orbital separation, which can be done using DEMs and accurate estimates of the state vector of the satellite. Since its application to the 1992 Landers earthquake (Massonnet et al., 1993) [42], the technique with its wide spatial coverage and

high accuracy (sub cm), has been widely used to study crustal deformation due to the earthquake cycle (i.e., coseismic, postseismic and interseismic) (Bürgmann et al., 2000; Cakir et al., 2012; Wright et al., 2001) [10, 11,68] along numerous active faults of the world during the last two decades. The main limitation to the accuracy of InSAR measurements is due to atmospheric artifacts, DEM errors, orbital residual and poor coherence (Zebker et al., 1997) [69]. To minimize these errors, a relatively new and advanced technique, i.e., Multi Temporal InSAR technique has been developed. This technique uses multi-temporal stacks of SAR images to generate time series of ground deformations for individual targets, named as Permanent Scatterers (PS) and small baseline InSAR (SBAS) (Berardino et al., 2002; Ferretti et al., 2001) [7, 16]. Currently, there are two broad categories of multi temporal InSAR techniques (Sousa et al., 2011) [58]; 1) PS methods including those that use coherence estimation based on a temporal model of deformation (Ferretti et al., 2001) [16] and those based on spatial correlation (Hooper, 2008) [27], and 2) small baseline (SBAS) methods (Berardino et al., 2002; Schmidt and Bürgmann, 2003) [7, 55]. Studies show that multi temporal InSAR techniques can resolve surface displacement of individual features at a level of about 0.5 mm/yr using all data collected over the target area by a SAR satellite.

To investigate the surface motions, we used the Stanford Method for PS technique (StaMPS) that uses both PS and SBAS InSAR techniques (Hooper, et al., 2004, 2007, 2008; Sousa et al., 2011) [25-27, 58]. The most recent version of StaMPS (StaMPS/MTI) can also combine both sets of results (PS and SBAS) to improve phase unwrapping and the spatial sampling of the signal of interest (Sousa et al., 2011) [58]. This technique recognizes potential persistent scatterer candidates using amplitude dispersion index (ADI). In addition to persistent scatterers, StaMPS also detects and uses slowly decorrelating filtered phase pixels (SDFP). The number of stable points (SP = PS + SDFP) candidates increases with increasing ADI. Number of persistent scatterer candidates has a significant role in detecting interseismic movements. However, there is a tradeoff between number of persistent scatterer candidates and number of unreliable targets as larger ADI values result in more unreliable points. Generally persistent scatterers density varies with terrain (i.e., 0-10 persistent scatterers/km^2 in mountainous areas and about 100 persistent scatterers /km^2 for urban areas).

In this research, ASAR SLC (Single Look Complex) images from a descending orbit (T49), I2 swath mode, collected by Envisat satellite of ESA (European Space Agency) between May 2003 and January 2010 have been used (Table 3.2). Width and length of the obtained data frame are 100 kilometer which covers major parts of the NTF and TB(see Fig. 3.2). Processes have been done using StaMPS/MTI (Hooper et al., 2010) which emphasis on DORIS computer code (Hanssen 2001; Kampes and Usai 1999) [21, 33] and focusing step is skipped, since the modality of the obtained images is SLC. Although conventional D-InSAR is a suitable approach to obtain

good results for coseismic studies but its temporal decorrelation, particularly in areas with dense and tall vegetation has a disadvantage for long term phenomena like land subsidence. StaMPS/MTI is a multi-temporal PS-InSAR techniqueto measure deformation signals through identifying Persistent Scatterers (PS) so that the amount of obtained PS can specify how much the PS-InSAR technique is successful (see details in Hooper et al., 2004) [25].Simply put, discrimination of coherent and incoherent radar signal is the core idea behind PS-InSAR which means that an individual recognized PS has an interpretablecharacteristic in time (Sousa et al., 2011). StaMPS benefits Amplitude Dispersion Index (ADI) to identify a bunch of pixels that includes all of the PS pixels. The ADI is defined by Ferretti et al (2001) [16] as follow:

$$D_A = \frac{\sigma_A}{\mu_A}$$
(3.1)

where σ_A is standard deviation and μ_A is mean amplitude values. The value of ADI is typically 0.4, but it is reasonable setting between 0.4 and 0.42 which usually contributes on PS selection and basically eliminated areas over water and those pixels located in tall vegetations (Ferretti et al., 2001; Sousa et al., 2011) [16, 58]. Playing with the threshold could affect processing time and it depend computer performance. Here, ADI is assumed to be 0.42 and the scene is subdivided into 25 patches with 200 and 1000 overlapping pixels in the range and azimuth directions respectively.

Using combination of PS-InSAR and Small Baseline (PSI+SBI), Thirty nine interferograms derived from a pool of 17 ASAR images with respect to their small baselines near 400 metersand also before PS processing step, coherence threshold is assumed to be greater than 0.3 (Fig. 3.3). Three of the images (No. 1, 2 and 3) are not included into the PS processing step because of first, their too long perpendicular baseline and second, temporal baseline which can drastically affect PS selection quality as a function of coherence (Fig.3.3).

Topographic phase component contained within inetrferograms is removed using an ASTER (http://jspacesystems.or.jp/ersdac/GDEM/) digital elevation model with spatial resolution about 30 meter (~ 1 arc second). Precise orbit data (VOR_DOR) have been converted to delft orbit data (ODR) using a matlab code for estimating exact position of the satellite, but usually our estimation is imperfect, because the orbital error is not completely removed. The most popular method to solve this issue is the subtraction of an estimated linear trend (or phase ramp) from the interferogram. By fitting a linear plane to the interferograms, deramp value of each interferogram is determined. Each of Interferograms (I_{ij}) comprises of master (i) and slave (j) images in a specific epoch, including an orbital phase ramp (r_{ij}) which is based on the position error in a specific epoch. The orbital errors can be assumed as contributing a phase ramp (Eq3.2), in a

specific epoch. Thus, the phase ramp in interferogram I_{ij} is the difference between the phase ramps between period of i and j (Eq3.3). Accordingly r_{ij} is determinable by fitting a linear plane to I_{ij} and use these planes to determine the coefficients a, b, c at each epoch. These are then used to calculate and remove an orbital phase ramp from each interferogram (I'_{ij}) (Fig. 3.3).

$$r_{ij} = a_i x + b_i y + c_i \text{ (3.2)}$$

$$r_{ij} = r_i - r_j = (a_i - a_j)x + (b_i - b_j)y + (c_i - c_j) \tag{3.3}$$

Table 3.2 List of the obtained SAR data (L1), their acquisition date, perpendicular baseline with respect to the master image and mean coherence values.

Image No.	Orbit	Year	Month	Day
1	6115	2003	05	02
2	6616	2003	06	06
3	8620	2003	10	24
4	9121	2003	11	28
5	10123	2004	02	06
6	11125	2004	04	16
7	11626	2004	05	21
8	14131	2004	11	12
9	20143	2006	01	06
10	20644	2006	02	10
11	25153	2006	12	22
12	25654	2007	01	26
13	26155	2007	03	02
14	26656	2007	04	06
15	27157	2007	05	11
16	32167	2008	04	25
17	39181	2009	08	28
18	40183	2009	11	06
19	40684	2009	12	11
20	41185	2010	01	15
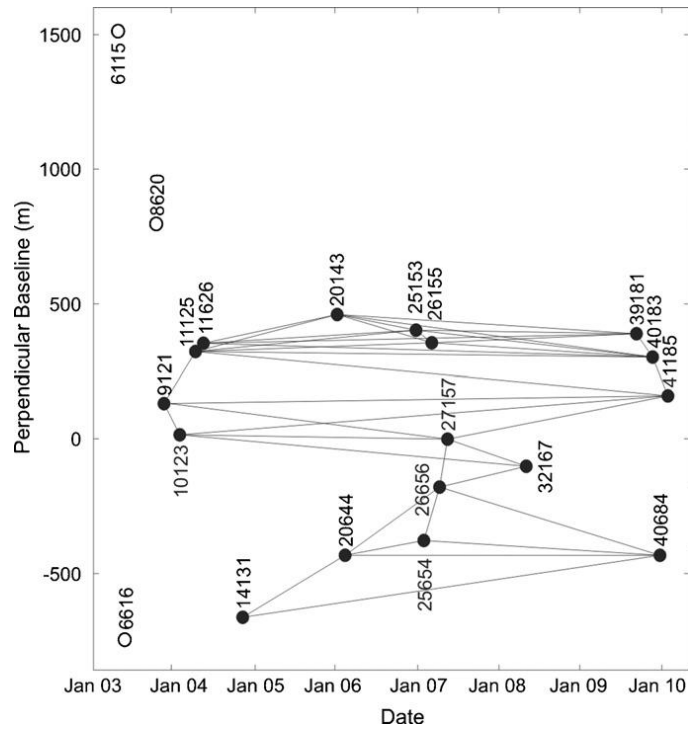
Fig.3.3 Temporal (up to 7 years) and spatial (up to 400 m) baselines for the ENVISATASAR interferograms (lines) and orbit numbers analyzed between November 2004and January 2010. Note that three scenes (open circles) are not used in the timeseries analysis as they fail to provide adequate coherence.

In our processing we use 0.42 for ADI and divide the scene in 5x5 patches with 200 and 1000 overlapping pixels (~4 km.) in the range and azimuth directions, respectively. Large overlaps between the patches ensure reliable merging of them at later stages of processing. In this study, we use a SBAS style network minimizing the perpendicular, temporal and Doppler baselines to maximize the correlation of generated interferograms and increasing the number of observable ground points. Unlike the SBAS approach described by Berardino et al. (2002) [7], StaMPS uses the full resolution (i.e., SLC) images instead of multi-looked scenes.

Fig.3.4 shows the mean LOS velocity field obtained from SBAS time series using 39 interferograms corrected for DEM errors using the v-d option in StaMPS (see details in StaMPS manual). Owing to the arid to semi-arid climate of the region an abundant number of SP (> 110,000) are found in the rural areas as well as the urban sites. To eliminate orbital residuals, a best-fitting least-squares plane is removed from the LOS velocity field using the SP on the gentle slopes of Sahand volcano east of the Tabriz basin and south of the NTF to avoid regions of land subsidence in the alluvial plane, shear strain in the near field, and potential atmospheric effects correlated with rugged high topography to the north. The most prominent feature in the LOS velocity field is the circular regions with yellow-to-red color where the fastest surface displacements occur between 2003 and 2010. Their circular pattern indicates rapid subsidence of

up to 20 mm/yr is restricted mainly to the Quaternary fine-grained alluvial plane of the Tabriz basin which will be discussed in the section 2.4.

Surface change due to the tectonic motion is detected in the LOS velocity field (Fig. 3.4). While the color contrast in LOS velocity between the southern (mostly green) and northern (mostly blue) sides of the NTF reveals the differential motion between the two blocks, the gradual color change across the fault attests to the interseismic strain accumulation. Therefore, the SAR data can be used in estimating the locking depth and slip rate of the NTF.
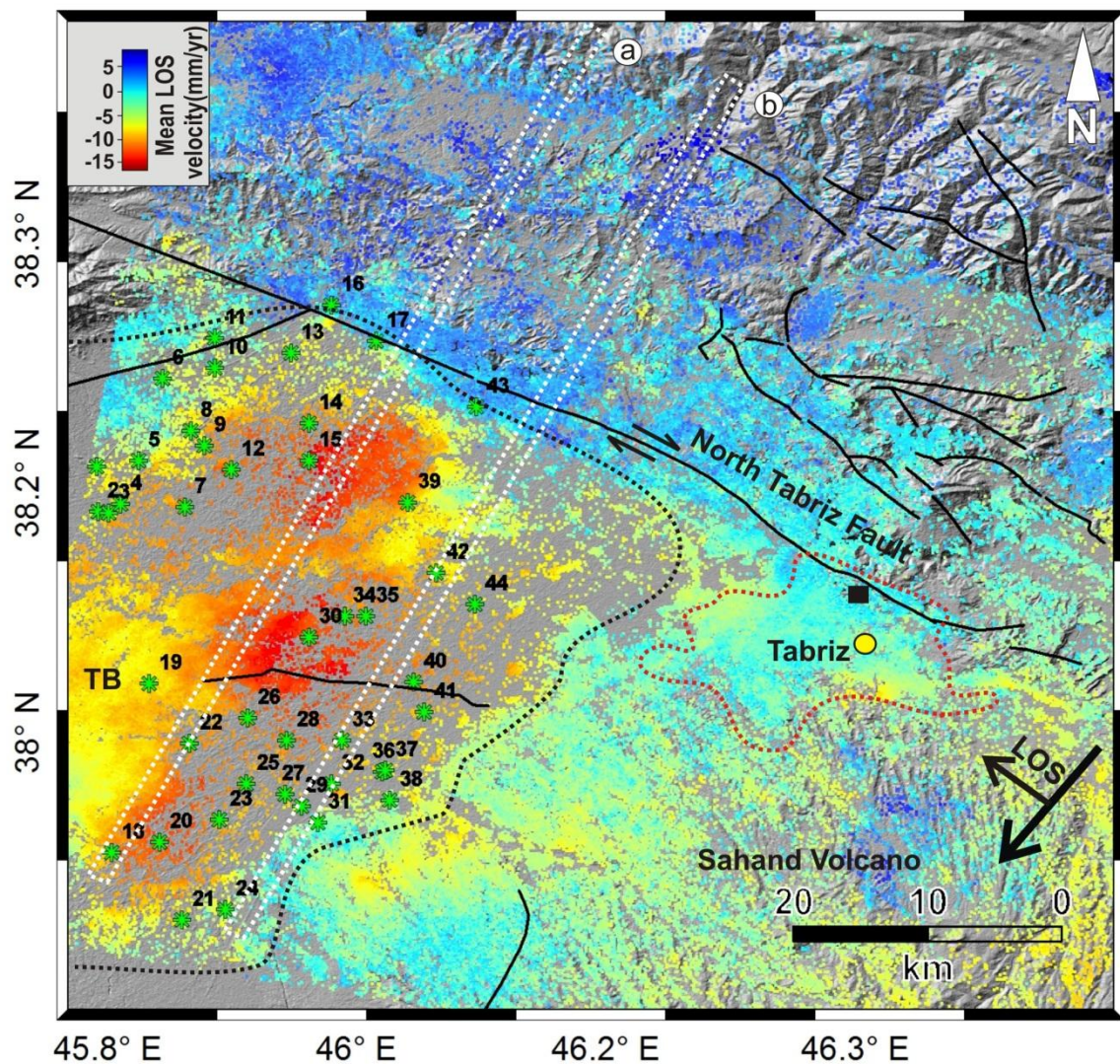
Fig.3.4 Mean LOS deformation rate between 2003 and 2010 along the North Tabriz Fault (NTF) plotted on ASTER shaded relief image with the location of water wells (green stars) excavated in Tabriz Basin, and active faults (black lines). The dashed back and red polygons indicate Tabriz Basin and Tabriz city respectively. Black lines are active faults in the region. The yellow circle is the location of GPS permanent station in Tabriz. White profiles "a" and "b" with 2km sampling width are plotted in the next section (section 2.4).

3.2.3 NTF slip rate and locking depth

Modeling of the InSAR data is carried out using screw dislocations for an infinitely long vertical fault in an elastic half space (Cakir et al., 2012; Motagh et al., 2007; Savage and Burford, 1973; Segall, 2002; Tatar et al., 2012) [11, 46, 54, 57, 63]. The locking depth, slip rate and shift in reference point velocity are estimated within 95% confidence limits using a Levenberg–Marquart nonlinear optimization algorithm with no *a priori* bounds.
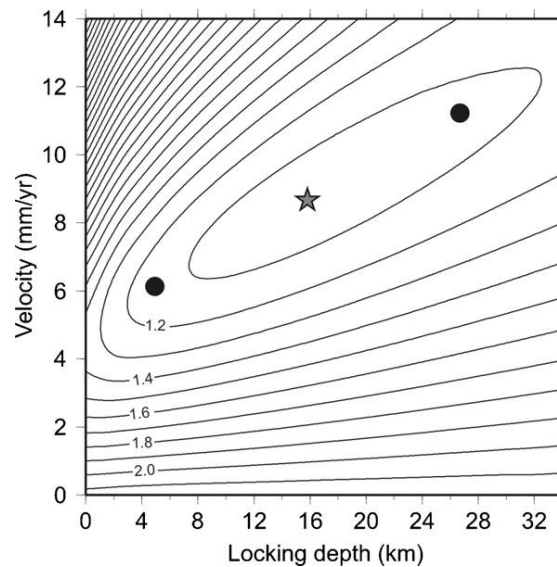
Fig.3.5 Contour map of RMS misfit (mm) between InSAR and GPS observations models with varying locking depths and slip rates. Star indicates the best misfit model. Black circles show upper and lower bounds of 95% confidence interval.

The fault position is defined by the surface trace of the NTF (Karakhanian et al., 2004) [31]and is kept fixed during the inversion. The mean LOS velocity field is converted to fault parallel mean InSAR velocities field assuming that the LOS range changes are due to purely horizontal motion on the NTF (Lyons and Sandwell, 2003) [39]. Far away from subsidence affected area, a mean PS velocity and its standard deviation are calculated at every km along the profile with the fault parallel component of the GPS vectors within a distance of 100 km on each side of the NTF. Although noisy, the mean SBAS velocity change across the fault reveals the typical arctangent pattern of interseismic strain accumulation for strike-slip faults (Motagh et al., 2007; Wright et al., 2001) [46, 68]. Joint inversion of the PS (88 points) and the GPS (11 points) data (Djamour et al., 2011; Masson et al., 2006) [14, 41] weighted by the uncertainty in each GPS data point and standard deviation of SBAS data yields a slip rate of 8.7 ± 2.5 mm/yr for the NTF, in good agreement with previously estimated slip rates of 7 to 10 mm/yr from GPS measurements (Djamour et al., 2011; Masson et al., 2006; Reilinger et al., 2006; Vernant et al., 2004) [14, 41, 50,

65] As illustrated in Fig. 3.5, the locking depth is poorly constrained and is 15.8 ± 10.8 km, similar to the estimates of Djamour et al. (2011) [14] that range between 6 and 26 km.

3.3 Non-tectonic deformations in Tabriz Basin (TB)

3.3.1 Land subsidence in Iran

Land subsidence is a kind of non-tectonic deformation or well-known as a major environmental problem in some countries as it can cause serious damages to the urban components such as: structures, buildings and sanitary sewers as a long-term deformation (Motagh et al., 2007; Dehghani et al., 2009; Lubis et al., 2011) [46, 13, 38]. It may occur due to various reasons such as earthquakes, mining, over extraction of oil, natural gas or groundwater and some urban activities (e.g. metro and tunnel constructions, etc.).

Precipitation rate and natural recharges in arid or semi-arid countries like Iran are relatively lower than the global average (Sedighi et al., 2010)[56] which shows importance of underground waters for agricultural or industrial activities. Interest of Iranians for ground water extraction goes back more than thousands of years ago when the Qanat system was invented for constant water extraction. In Iran Qanat system is a traditional underground tunnels excavated into the hillside which provides water demand for agriculture and population. In the recent decades the country is faced with serious challenges in the water sector. The accumulated water behind dams and underground water (Qanat) cannot rectify demand of industrial, agriculture and urban purposes (Madani 2014) [40]. Thus a large number of deep wells (> 50m depth) have been excavated in different parts of the study area (Razzaghmanesh et al., 2006) [49].

Iran has six major hydrological basins as follows:

1- Persian Gulf basin, 2- Central basin, 3- Urmia basin, 4- Sarakhs basin, 5- Hamoon basin and 6- Khazar basin (Fig. 3.6). Almost half the country's renewable water resources are located in the Persian Gulf basin which is about one fourth of the country's land area. Central basin as the biggest basin in term of land area has less than one third of the renewable water resources (FAO 2009). Excessive water (or other fluids) withdrawal have caused land subsidence throughout the country (Alipour et al., 2008; Anderssohn et al., 2008; Dehghani et al., 2009; Motagh et al., 2008) [2, 5, 13, 47] due to pore fluid pressure decreasing between granules in unconsolidated sediments (weak materials) (Hoffmann and Zebker, 2001; Bell et al., 2008) [24, 6]. Balancing between downfall and water extraction could be helpful to control or mitigate the probable hazards in the future (Motagh et al., 2008) [47]. In this study we investigate large-scale surface deformation associated with groundwater tablechanges using the Synthetic Aperture Radar Interferometry

(InSAR) and piezometric data in the Tabriz Basin (~3000 km^2) which is a sub-basin of Urmia basin located between 37º57'N-38º20'N and 45º39'E-46º20'E.The Tabriz basin (TB) is located in the west of Urmia Lake and from the east its boundaries are limited by the city of Tabriz (Fig.3.6). The investigated area contains various structures (mostly Quaternary alluvium) from different ages (Devonian to Quaternary)because of a marine regression happened in Pliocene period, as well as a turning into a continental condition. Plio-Pleistocene indicated volcanic activities, with lava flows in southern part of the Tabriz Basin. Thus, the Sahand volcano engrossed south part of the Tabriz city. This mountain is surrounded by volcanic sediments and alluvial tuffs which cover Pliocene marls and sandstones of below layers. These volcanic tuffs are enlarged in a vast area (~1000 km^2) and overlie the Pliocene beds to the south of the TB (Moghaddam and Najib 2006) [44].
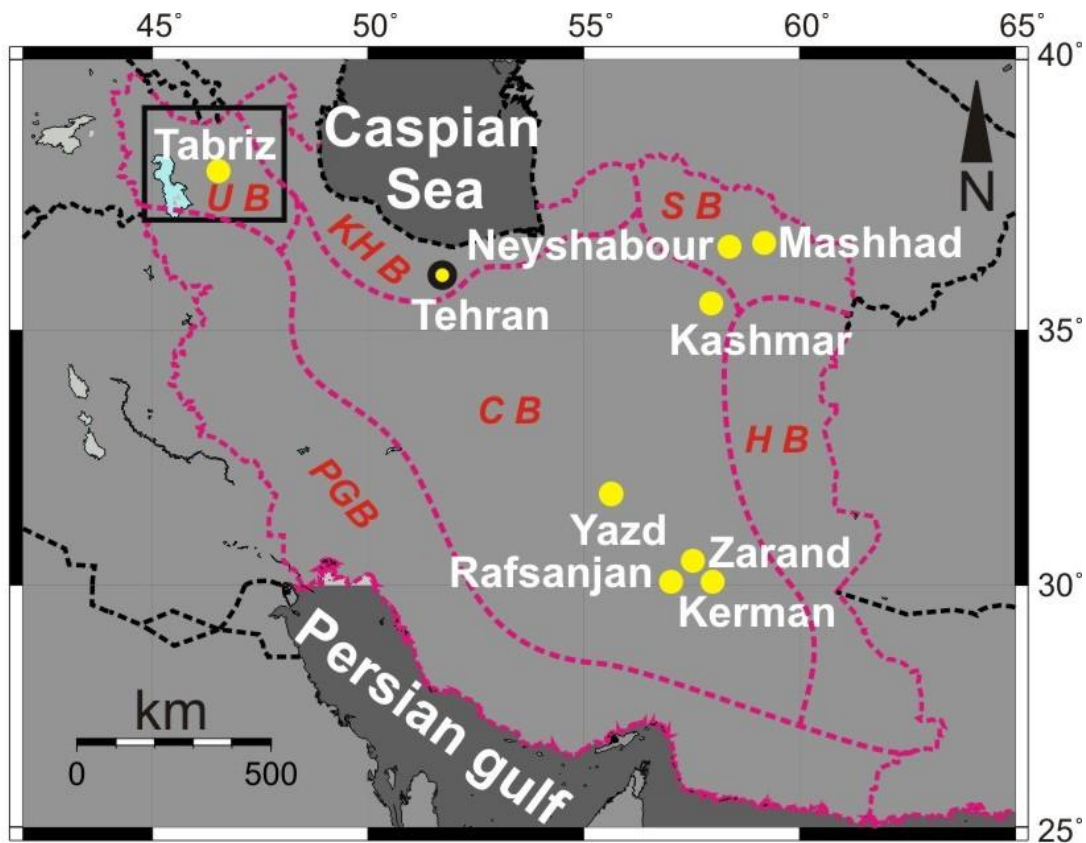
Fig.3.6 Six major basins in Iran divided by the pink dashed polygons. PGB = Persian Gulf Basin; UB = Urmia Basin; KHB = Khazar Basin; SB = Sarakhs Basin; HB = Hamoon Basin; CB = Central Basin. The yellow circles showing important cities subjected by land subsidence phenomenon.

Some important industrial structures, such as thermal power plant, petrochemical center and Tabriz-Miandoab water lifeline are situated in the TB (Karimzadeh and Ahmadi 2013) [34]. More than 40 wells have been excavated to extract groundwater for agriculture and industrial needs (e.g.

coolingmajor components of the thermal power plant which supplies the electricity of NW Iran).
Furthermore, statistical studies show that water-extraction rate in the TB is about 5 million cubic
meters per year while the allowable threshold is around 3 million cubic meters for each year

(Razzaghmanesh et al., 2006) [49].

Table 3.3 Subsidence rate deduced through InSAR technique in some cities of Iran (see Fig. 3.6 for their location).

Region	Cumulative subsidence amount (cm)	Period (years)	InSAR Approach	Reference
Mashhad	30	2003-2005	Conventional stacking	Motagh et al., 2007
Mashhad	86	2004-2007	WLS adjustment	Akbari and Motagh, 2011
Tehran	45	2003-2007	Conventional time series	Alipour et al., 2008
Neyshabour	19	2004-2005	SBAS	Dehghani et al., 2009
Rafsanjan	19	2005- 2006	Conventional	Motagh et al., 2008
Kashmar	6	Apr 2005 - July 2005	Conventional	Anderssohn et al., 2008
Kerman- Zarand	20	2003-2004	Conventional	Motagh et al., 2008
Yazd	9	2003-2004	Conventional	Motagh et al., 2008

In Iran, different InSAR strategies have taken into account in order to detect the land subsidence
in the major basins. Alipour et al., 2008 [2] studied the land subsidence of Tehran plain using 46
Envisat ASAR data obtained in descending (Track 378 & 419) and ascending (Track 414) orbits
between 2003 and 2007. Motagh et al., 2008 [47] studied Mashhad land subsidence (in Sarakhs
basin) through a pool of Envisat images between 2003 and 2005 using a conventional (stacked
method) InSAR method to compare the obtained results with the measurements from precise land
leveling. After that, Akbari and Motagh (2011)[1] suggested a weighted least square (WLS)
method for the same region which is based on an appropriate combination of differential
interferograms produced by image pairs with a small baseline (orbital separation) in order to limit
the spatial decorrelation phenomena. Dehghani et al., 2009 [13] produced InSAR time series
through 14 Envisat ASAR (2004-2006) data and a small baseline method (SBAS) for a small
historical city Neyshabour subjected to land subsidence again in Sarakhs basin. Anderssohn et al.,
2008 [5]used a total of 22 Envisat ASAR data for the time interval from July 2003 to March 2006
in the descending satellite track 435 using conventional InSAR to study land subsidence in
Kashmar valley in Hamoon basin (for details see Table 3.3). In this study, immature land
subsidence in the TB is investiagted using Persistent Scatterer Synthetic Aperture Radar
Interferometry technique (PS-InSAR) combined with the small baseline InSAR (SBI) to construct

the InSAR time series in a region of 10000 square kilometers. In this paper, the study area isideal for InSAR studies due to its arid and semi-arid climate. Thus, its sparse vegetation will not be an obstacle for phase interferometry analysis.

3.3.2 Groundwater level in Tabriz Basin (TB) and watershed analysis

An aquifer system is an interbedded, saturated and made up of different parts that expresses as two forms of permeable (aquifer) and impermeable (aquitard). Drops in groundwater levels caused some bearers for the bulked material to move from under pressure pore to the granular skeleton of an aquifer system, resulting land subsidence. On the contrary, recharging aquifer leads to increase in pore pressure thereby causing ground uplift (Lu and Danskin, 2001) [37]. Lack of proper water recharging of wells and irregular water withdrawal are two main factors of aquifer system compaction in Iran (Dehghani et al., 2009; Motagh et al., 2008) [13, 47]. Although, seasonal aquifer recharge in NW Iran is higher than the rest of Central Iran, the NW has undergone subsidence due to excessive ground water extraction over the last decades (Sedighi et al., 2010 and Moghtased-Azar et al., 2012, Kabiri et al., 2012) [56, 45, 32]. There are probably hundreds of illegal deep wells used mainly for agricultural purposes in the region. In this study over 40 deep wells are recognized and plotted in Fig. 3.7, but information of these wells are mostly lacking. Only piezometric measurements of six wells (1, 3, 5, 15, 26 and 30) are collected monthly by the Regional Water Organization. Water level measurement with a piezometer is based on liquid pressure above a specific datum.For example, ina washing machine, the height of the water in the tub is measuredindirectly by measuring the pressure atthe bottom of the tub. Accordingly in an aquifer, piezometric measurements also can be calculated from screen depth and piezometer's elevation.

In order to delineate areas affected by subsidence, a sophisticated image segmentation method is proposed. Having adequate and reasonable classes of the wells needs a watershed transform analysis. A watershed is the ridge (or upper slope) area that flow(i.e. water) goesto a pour arealike a drainage basin. As already discussed, it can be part of a larger watershed and can also contain sub-watersheds(e.g. Tabriz basin as a sub-basin of Urmia basin). In this paper watersheds are delineated through an ASTERdigital elevation model in a couple of steps as follows:

At the first step the flow direction which is the steepest downslope neighbor of each pixel is calculated for the study area. Then in the second step, flow accumulation is calculated. In fact, flow accumulation is the accumulated weight of all pixels traveling into each downslope cell. The results came from second step will be helpful in the third step to find some arbitrary pour points. The pour point, is a point on the surface at which water flows out of an area(e.g. a river mouth) and typically it could be the lowest point in a sub-basin or whatever is defined as a boundary.

After snapping these points by the flow accumulated map at the fourth step, watershed areas can be calculated as shown in Fig. 3.7. It must be noted that a threshold value (number of pixels that make a stream) should be specified at the fourth step (Fig. 3.7).
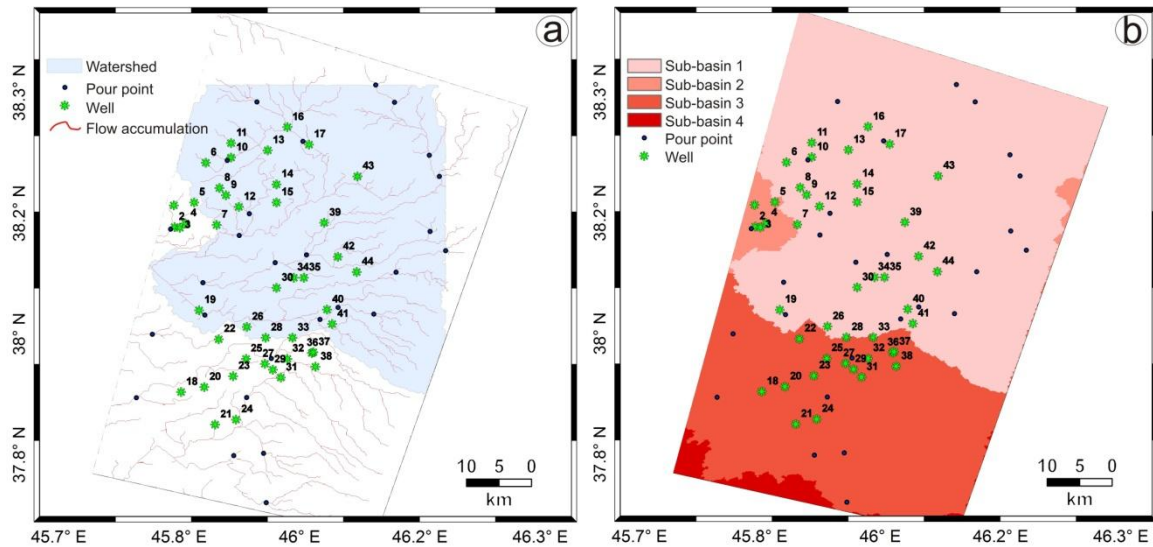
Fig.3.7 (a) Water accumulation map of TB derived from ASTER digital elevation model. Blue polygon shows major watershed of the study area; **(b)** Sub-basins in TB based on flow accumulation map and pour points (blue points).

The wells are classified into 2 groups based on above-mentioned sophisticated segmentation method which classifies sub-basins based on amount of accumulated water at each sub-basin. Sub-basin 1: Wells 15, 26 and 30 which show significant subsidence in the core of the subsidence patterns. Sub-basin 2: Wells of 1, 3 and 5 which do not show sensible deformation located in the outside margins of the subsidence patterns. Normally, the sub-basin 1 and 4 have minimum and maximum amount of water accumulation due to general slope of the region from NE to SW. This usually can be one of the reasons of higher water level in the wells of sub-basin 2 than sub-basin 1.

3.3.3 InSAR and water level results

Results from PS-InSAR indicate that over 100000 PS velocities have been recorded and the land subsidence patterns at the TB are emerging at three oval-shaped patterns in sub-basin 1 near W15, W26 and W30 (Fig. 3.4). The dark blue PSs are abundant at the north block of the North Tabriz Fault which is associated with interseismic slip rate of the fault (Karimzadeh et al., 2013; Rizza et al., 2013) [34, 52]. With Fig. 3.4, two profiles with 2km PS sampling width in the TB are drawn from north to south, perpendicular to the North Tabriz fault as a major tectonic feature of the study region. 1- Profile "a" which crosses from first subsidence bowl in the north. 2- Profile "b"

which crosses from inner margin of the TB (Fig. 3.8). The effect of atmospheric phase delay sometime is considerably large and usually shows itself from the temporal variation of the stratified troposphere (e.g., Hanssen, 2001) [21]. Consequently phase patterns typically mimic the topography. It means that in areas with high correlation between topography and InSAR, it is difficult to separate atmospheric and deformation signal. In the study region, the subsidence rates (gray points) are almost independent from the topography (redline) which is shown in Fig. 3.4. Absence of correlation between the mean PS subsidence rates and topography along the profiles demonstrates that atmospheric effects are too small.
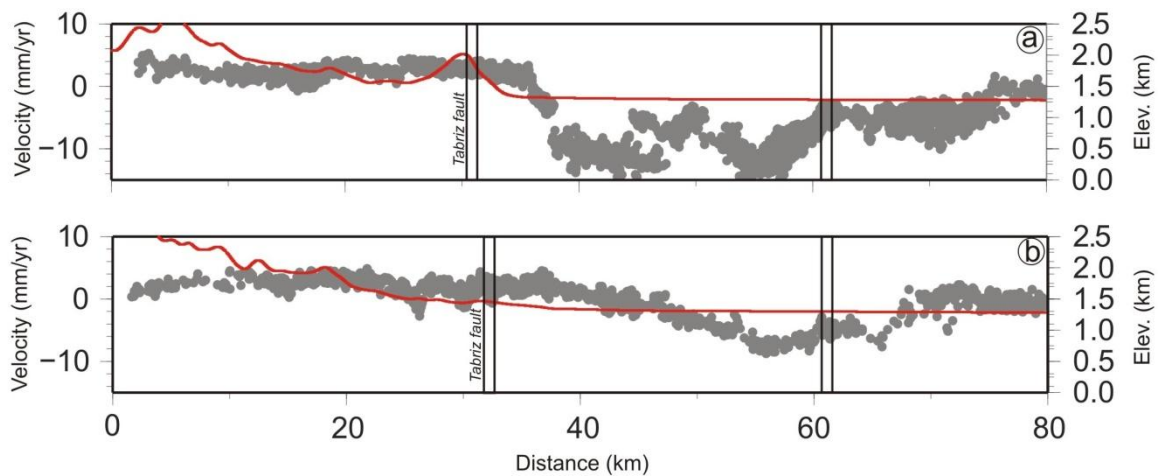
Fig.3.8PS and topography profiles showing subsidence rate and topographic variation in the TB (see the locations in Fig. 3.4).

The related piezometric data are collected from 2001 to 2010 monthly but because of road constructions and some civil projects at the TB, observations were stopped in some wells (e.g., W15). Pizeometric measurements of the wells 15, 26 and 30 located in sub-basin 1are showing land subsidence subsequently in some epochs (Fig. 3.9). However some piezometric fluctuations do not confirm InSAR time series which means that subsidence is not only a function of water level fluctuations and needs more supplementary data and field observations. Also must be considered that InSAR time series by few images/year cannot show a very high correlation. For example between 2007 and 2009, decline of water level at the W30 is almost lower than the relevant InSAR time series. One reason could be by hydrogeological structures of the region (high permeability) which should be investigated in future works. Nevertheless, seasonal variations show good correlation between pizeometric levels and InSAR deformations (Fig. 3.9). InSAR time series show the cumulative subsidence for the W30 is around 40 mm between 2004 and 2010.
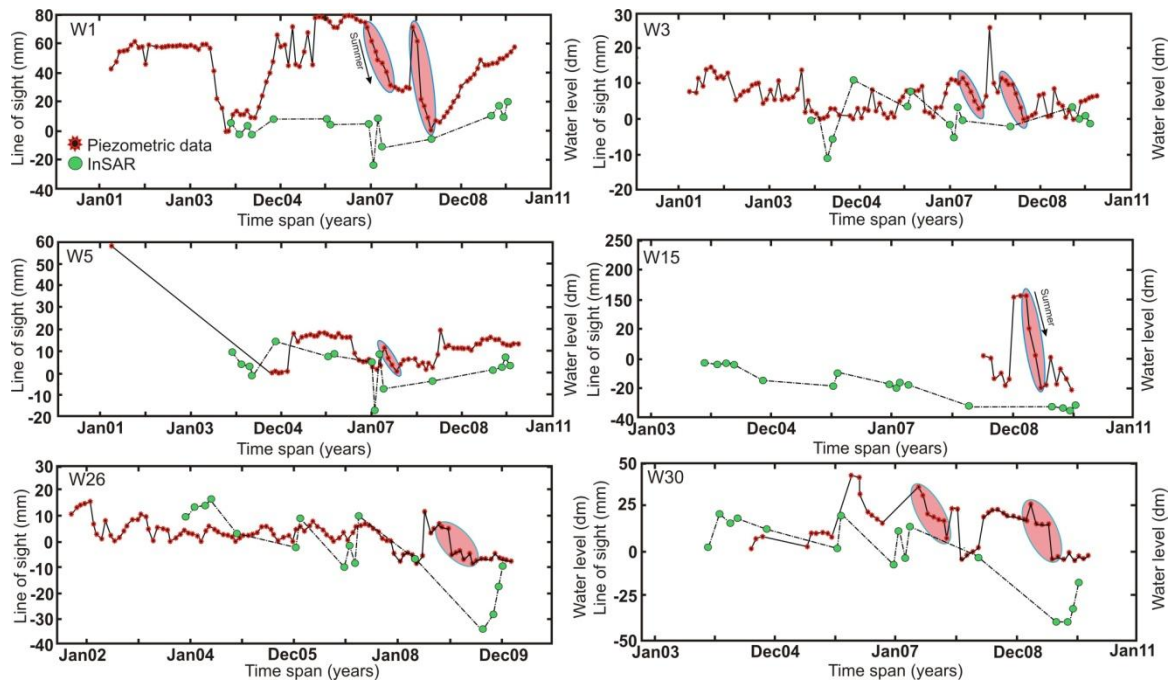
Fig.3.9 Water level fluctuation and InSAR time series at the piezometric wells (1, 3, 5,15, 26 and 30). InSAR results show at W1, W3 and W5 (sub-basin 2) seasonal deformation has been occurred but they do not show considerable subsidence between 2004 and 2010while W15, W26 and W30 which are located in the sub-basin 1(lesser water accumulation) have maximum ground subsidence between 2007 and 2009. Some seasonal changes are between 2007 and 2009 are shown by pink ellipsoids.

3.3.4 Storage coefficient

Several studies have already suggested relationships between land subsidence and the properties of the aquifer system (e.g. Galloway et al., 1998; Kim et al., 2010; Lu and Danskin, 2001; Nwankwor and Egboka, 1992; Riley, 1969)[18, 35, 37, 48, 51], but in this study the knowledge of the aquifer cycle is lacking. Thus, a onedimensional model is applied. The model directly depends on subsidence/uplift amount to groundwater level variation by the storagecoefficient (S_k).This is a simple model considers that the compaction is uniaxial and vertical and it is useful when there is not geomechanical knowledge of the studied system. Then, the proposed model by Tomás et al. (2010)[64] is followed:

$$S_k = \frac{\Delta D}{\Delta h} \quad (3.4)$$

where ΔD is the land subsidence associated to a Δh piezometric level decrease. In order to determine S_k values, a unique hydrological system at depth has been assumed corresponding to

where groundwater is pumped, without alternated aquitards and aquifers. The piezometric levels of the classified wells located in the Fig. 3.4 are used.

For the sub-basin 1 in the center of the subsidence patterns, W15 shows 2m water level declining and0 mm subsidence between 2008and 2010 which means that the storage coefficient is zero. At the period between 2004 and 2010, W26 and W30 show 1.5m and 0.1m water level declining, 22mm and 40mm subsidence, respectively. Also the yielded storage coefficient form W26 and W30 are 0.146 and 0.4 respectively (see details in Table 3.4). Water decline in W26 and W30 is lower than W15 in epoch 2008-2010. One reason could be existence of an unknown fault between W26 and W30 (see Fig. 3.4) which confines water penetration to another layers (Anderssohn et al., 2008). However futher investigation is needed about the below layers; another reason could be related with the large amount of the fine grained materials which have main roles in charging intervals (Haddadan and Zohrab 1994) [20]. For wells of the sub-basin 2 located in the western margin of the subsidence pattern minor uplift or subsidence have been observed (Fig. 3.9). Declining trend associated with the InSAR time series of W15 has been accelerated between 2006 and 2009 while for W26 and W30 it happened from 2007 to 2009. At the end of 2009 and early 2010 minor uplift probably comes from seasonal recharges. If the subsidencecontinues with the same acceleartion of 2007-2009 epoch, the subsidence patterns would be expanded to the outer margins of the TB in near future.

Table 3.4 Total subsidence/uplift, water level and storage coefficients (S_k) at the excavated wells of TB.

ID	Time period (yr)	Subsidence/Uplift (mm)	Mean 7-year displacement rate (mm/yr)	Water level (m)	S_k
Sub-basin 1					
W15	2008-2010	0	-5.7	-2	0
W26	2004-2010	-22	-2.8	-1.5	0.146
W30	2004-2010	-40	-5.7	-0.1	0.4
Sub-basin 2					
W1	2004-2010	+14	+2	+5	0.0028
W3	2004-2010	0	0	+0.6	0
W5	2005-2010	-11	-1.5	+1.27	-0.0866

3.3.5 GPS vs InSAR

Information of geodetic measurements near of the subsidence region are lacking except one permanent GPS station in the Tabriz city which belongs to National Cartographic Center (NCC).

It is established on a pillar extending deep intothe ground to provide stability(Djamour et al., 2011) [14]. On the other hand, number of PSsis sparse in some areas. Therefore, they were not reliable for comparison with the GPS continuous station (TABZ). To resolve this inconsistency, the InSAR results are refined, and the uncertainties in gap areas must be reduced for a flawless comparison between GPS and InSAR timeseries. The Kriging interpolation is a powerful statistical method in soil and earth sciences which allows us to convert "modality" of a dataset from discrete points into a grid data. Here,a simple Kriging method to predict the unknown PS value on the surface is used. The unknown *PS* value at coordinates38º03'21"Nand 46º20'34"E (location of TABZ GPS station) can be calculated with the following general equation:

$$PS(Lon_i, Lat_j) = \sum_{\alpha=1}^{n} W_{ij\alpha} \times PS_\alpha \qquad (3.5)$$

Where n is the number of known values; PS_α. $W_{ij\alpha}$ is a set of weight factors for known PS. The weight factors are calculated by finding the semi-variogram values for all distances between input points and the semi-variogram values for all distances between an unknown PS and all input points; a set of simultaneous equations must then be solved. Points closer to an unknown PS take greater weight, while those farther away bear a lesser weight. The Kriging approach assumes that the distance ofcontributed points reflects a spatial correlation.Using this idea the gap area in the surface can be calculated. It fits a function to a specific number of pointswithin a specific radius (here assumed to be 50 meters) to determine a reliable output value for the precise location of TABZ station. The comparison confirms that land subsidence has not been entered into the urban areas (Fig. 3.10).
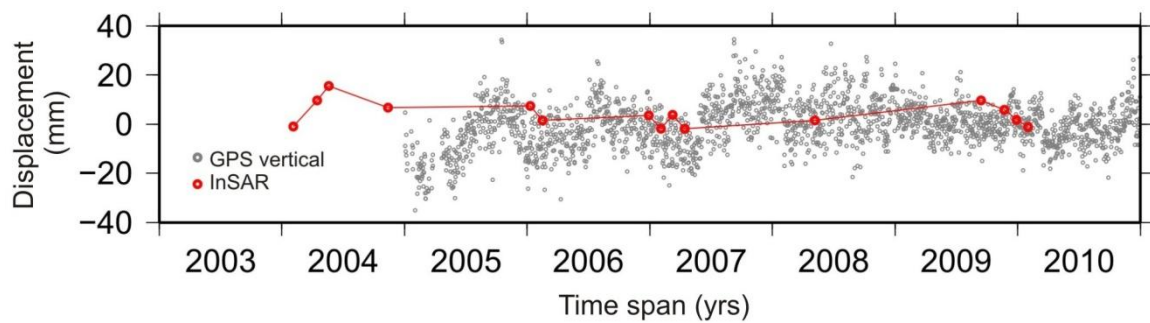
Fig.3.10 Comparison of InSAR and GPS (converted to LOS rate) times series in the Tabriz station (TABZ).

3.4 Coulomb Failure Stress and Ahar double earthquakes

3.4.1 Coulomb Failure Stress

An earthquake can be triggered by stress changes related with other earthquakes of active faults in the vicinity of a seismic region, which can induce or postpone seismic activities on a specified fault. This concept has been raised numerous investigations whether scientists could predict earthquakes or not. Although exact prediction of earthquakes are not possible yet, using Coulomb Failure Stress (ΔCFS) indicates the trends of potential seismic origins in studied region, to get through outstanding problems in this regard. For example, westward-progressive cluster of earthquakes that ruptured 1000 km of the North Anatolian Fault (NAF) in Turkey during 1939 and 1992 made an opportunity to study next large events. However, it occurred earlier than estimated time, with 1999 Izmit and Düzce earthquakes in expected areas where an increase in ΔCFS had been estimated (Stein et al., 1997) [60]. Furthermore, ΔCFS calculations reveal that 9 out of 10 ruptures along NAF surpassed to failure by the preceding events. However, timing and slip distribution for earthquakes have complex mechanisms and an accurate assessment by ΔCFS analysis depends on fault geometry and reliable seismological data.

In rock mechanics, Coulomb Failure Stress (ΔCFS) is one of the vast used criteria to characterize of rock failure (Jaeger and Cook 1979) [29]. Recently it has been applied in earthquake-related studies and led more reliable findings and better description of probabilistic hazards (Stein and Lisowski 1983; Stein et al., 1997; Toda et al., 1998; Takeo et al., 2011) [59-62]. The ΔCFS calculation stands on some parameters such as: fault geometry (strike/dip/rake), friction coefficient of the crust (King et al., 1994) [36], width and length of ruptured fault (usually called source fault) and geometry of neighbor faults (usually called receiver faults). The ΔCFS distribution caused by a source fault on receiver faults of surrounding area can be defined by the following simple form:

$$\Delta CFS = \Delta\tau_s + \mu'\Delta\sigma_n \quad (3.6)$$

In which $\Delta\tau_s$ is change in shear stress (positive in the direction of slip), $\Delta\sigma_n$ is the change in normal stress (positive in tension), and μ' is the friction coefficient with a range of 0.0-0.8 (King et al.,1994) [36]. Pore pressure level plays a significant role on the friction coefficient, but because of poor information of crust in Iran, it is assumed to be constantly 0.4 in the calculations of ΔCFS (see more details in King et al., 1994) [36]. Poisson's ratio as a dimensionless parameter usually is 0.5 for an incompressible volume, for each three events, Young's modulus has been fixed with default parameters of Coulomb software.

3.4.2 Ahar double earthquakes and coseismic stress changes

As mentioned already, interaction of 22±2 mm/yr between the northward motion of the Arabia plate relative to Eurasia at N8°±5°E hosts numerous thrust and strike-slip faults in different parts of Iran (Fig. 3.11). Iran can be considered as a wide boundary between Arabia and Eurasia plates as an intense seismic country located in the middle part of Alpine-Himalayas belt which starts from easternEurope and runs to Tibet. In this sub-section Coulomb Failure Stress (ΔCFS) changes of catastrophic Ahar double earthquakes is presented. Fault rupture parameters and focal mechanisms identified by CMT and NEIC catalogues, as well as aftershocks locations according to local seismic network of International Institute of Earthquake Engineering and Seismology (IIEES) are imported to Coulomb analysis (Fig. 3.12).
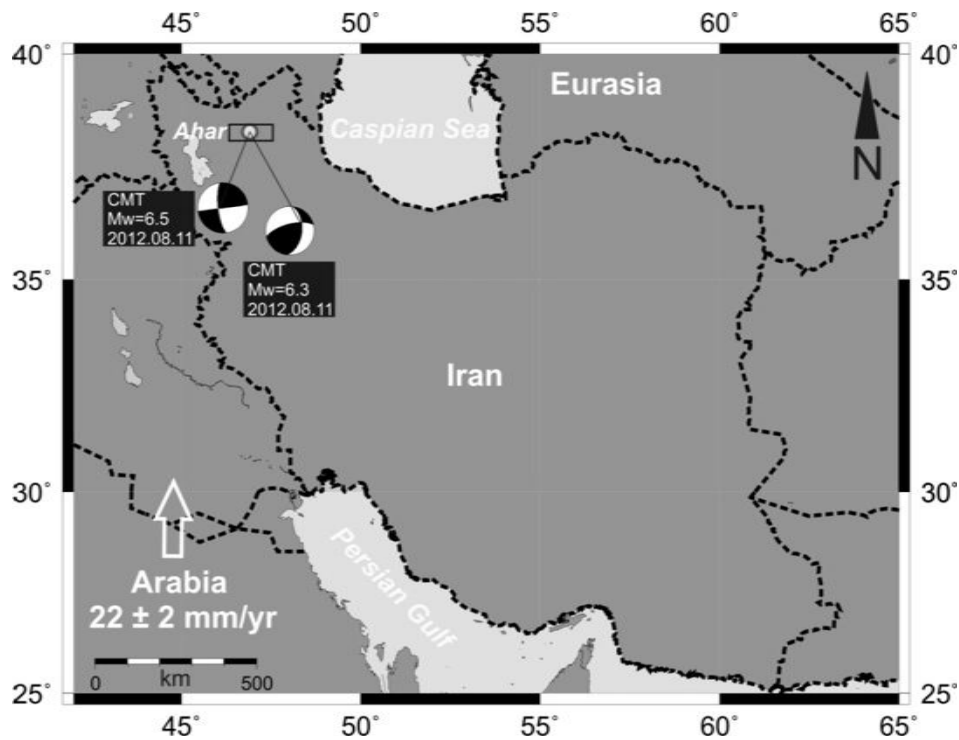
Fig.3.11 Map of Iran demonstrating Arabia-Eurasia convergence and focal mechanisms of Ahar double earthquakes.

Table 3.5 Location and source parameters of the earthquakes studied.

Event name and date	Event catalogue	Mw	Lat.	Lon.	Depth	Strike	Dip	Rake
Ahar 2012.08.11	CMT IIEES	6.5	38.55	46.87	10-15	82	89	164
Ahar 2012.08.11	CMT IIEES	6.3	38.58	46.78	10-15	256	67	135

For each event, length and width of ruptures determined by empirical relations as below:

$$\log(RLD) = -2.44 + 0.59 \times Mw \quad (3.7)$$

$$\log(RW) = -1.01 + 0.32 \times Mw \quad (3.8)$$

$$\log(AD) = -2.44 + 0.59 \times Mw \quad (3.9)$$

Where Mw is earthquake magnitude, RLD is subsurface rupture length (km), RW is downdip rupture width (km), and AD is average displacement (m) (Wells and Coppersmith 1994) [66]. Ahar city in NW Iran experienced two moderate sized earthquakes within 10 minutes killing more than 300 people (Hosseini 2012) [28]. Aligning roughly in E-W direction and separated in space about 10 km. The first event has a Mw of 6.5 and the second 6.3. The fault rupture observed in the field is about 25 km long and subdivided for each 4 km regarding of slip variation of epicenter, and edges and contributed in ΔCFS analysis. The source is 25 km long for first and about 20 km for the second one. There were not major difference in ΔCFS results of altered earthquake depth of 10 km (as a report of CMT) and 15 km (as a report of IIEES)(Table 3.5). Also locations of aftershocks reveal that thrust faults are dominant receiver faults in the area. Though, Ahar twin earthquakes were destructive and probability of earthquake triggering on North Tabriz Fault as a strike-slip structure needs further analysis and more reliable seismological data.
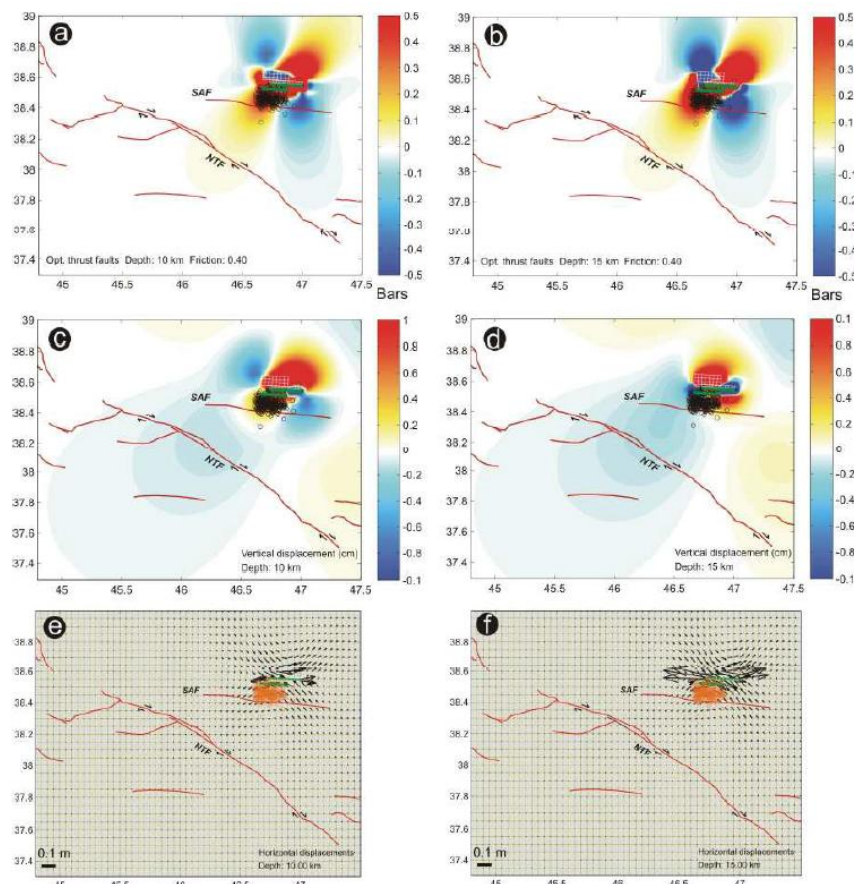
Fig. 3.12 NTF = North Tabriz Fault; SAF = South Ahar Fault. **(a)** and **(b)** : Coulomb Failure Stress of

optimum thrust fault for depth of 10 km and 15 km. **(c)** and **(d)** : vertical displacements **(e)** and **(f)** : horizontal displacements for depth of 10 and 15 reported by CMT and IIEES. Red lines are active faults, green lines are ruptured faults and black circles are aftershocks. In Fig. 3.12e and f, the orange circles are representing aftershocks.

3.5 Conclusion

The rate at which a fault slips determines the seismic hazard that it represents because average earthquake recurrence intervals tend to decrease as slip rates increase (Roberts et al., 2004) [53]. Thus, higher geodetic slip rates imply shorter recurrence interval for large earthquakes on the NTF as opposed to those determined by paleoseismic studies based on trenching (Hessami et al., 2003a) [22]. Therefore, estimating the rate of interseismic strain accumulation across the NTF is critical in determining earthquake potential and seismic hazard for the city of Tabriz, the fourth most populous city in Iran with a population of over 1.5 million.Hence, we used a multi temporal InSAR technique to deduce the slip of the North Tabriz Fault using 17 ENVISAT ASAR images acquired during a period of 6 years between 2004 and 2010. Elastic dislocation modeling of the InSAR data yields an average slip rate of 8.7 ± 2.5 mm/yr, in agreement with previous geodetic estimates based on recent GPS measurements. This supports the inference of Djamour et al. (2011) [14] that earthquake recurrence intervals for large earthquake (Mw 7 to 7.3) on the NTF are about 250-300 years, much shorter than that (821 ± 176 years) estimated by Hessami et al. (2003a,b) [22, 23] with paleoseismic investigations (see Wells and Coppersmith [1994] for the empirical relationship between average coseismic slip and magnitude for strike slip earthquakes). Therefore, an elapse time of 232 and 291 years since the two last major earthquakes nearby Tabriz on the NTF implies a high potential for a large earthquake in the next several decades.The obtained results demonstrated once again that interseismic strain accumulation with a sub-centimeter rate can be successfully detected and measured by multi temporal InSAR techniques (Gourmelen et al., 2011) [19] in arid to semi-arid regions. Therefore, SBAS or similar time series techniques can be applied to other sections of this fault system in Turkey and Iran.

PS-InSAR results show the maximum land subsidence is occurred in the well 30 (~40 mm) at the center of subsidence pattern which was growing between 2004 and 2009. Water level measurements and PS-InSAR results are used in order to show relationship between land subsidence, seasonal recharge and amount of water removal, but lack of enough geodetic observations (i.e. GPS or even precise leveling) in the study area restricts extensive interpretation of large-scale deformations. Only one thing, the subsidence ratewas accelerated in W15, W26 and W30 (sub-basin 1) between 2007 and 2009 according to InSAR time series.With respect to the country's climate, seasonal water fluctuations (water recharge and discharge) are relatively correlated with seasonal climate condition of the above-mentioned wells (W15, W26 and W30). A few examples with drastic slope between 2007 and 2009 are shown in Fig.3.9 by pink ellipsoids.

Even, in some cases before 2007, you can see water level declines toward summer. For example in W26 water level declines periodically every summer, but these trends have more acceleration after 2007 when land subsidence accelerates as well. In W1 and W3, in both summers 2007 and 2008, water level goes down because of extra agricultural activities and lack of rain precipitation. After that, because these wells are located in sub-basin 2, naturally they receive larger amount of water with the onset of snow season and accordingly water level goes up. It must be noted that unit-scale on Y-axis is different between water level and InSAR observations, thus visual comparison of these two kinds of observation does not sound reasonable.

The storage coefficients are able to determine characterizations of aquifer system. In this study, the storage coefficients are calculated from the subsidence rate using a simple relation (subsidence rate/water level rate), where one condition for inelasticity of the deformation is that the groundwater level (h) is greater than a maximum recorded level (h_{max}). As shown in Fig. 3.9, the levels in W15, W26 and W30 are not continuously declining and accordingly InSAR time series of these wells show small amount of uplift in January 2010. Simply put, if the level h_{max} is continuously going down, it indicates the inelasticity of the deformation, which can be then considered as permanent, but the above-mentioned wells are not subjected under this circumstance. Additionally the comparison of GPS and InSAR time series confirms that the land subsidence has not been occurred in the urban area.

In the past decades, earthquakes, thought to be random events, have been shown to exhibit periodicity in their cycles and location of aftershocks. Earthquakes can be triggered as a result of stress changes induced by other earthquakes, the most common examples of this being aftershocks. Though ΔCFS calculation is limited by inability data and less assumptions, it is an approaching way to predict location of earthquakes. We used the derived earthquake magnitudes by various catalogues together with the empirical scaling laws and relationships of Wells and Coppersmith (1994) [66] to estimate ruptured areas. Geological surveying of ruptured area concludes reliable results for our analysis. As well as, coordinates of earthquakes and aftershocks must be determined well. However for Ahar case, the location of earthquakes and aftershocks which have been presented by different catalogues, are not the same and could lead to misinterpretation. Thus, dense seismic network is essential for better assessments. Both main-shocks and aftershocks could affect ΔCFS, but in this study ΔCFS calculated only for main-shocks.

References

[1] Akbari, V., Motagh, M., 2011, Improved ground subsidence monitoring using small baselines SAR interferograms and a weighted least square inversion algorithm. Geoscience and Remote Sensing Letters, IEEE. 9, 437-441.

[2] Alipour S, Motagh M, Sharifi M, Walter T.R (2008)InSAR Time Series investigation of Land Subsidence due to Groundwater Overexploitation in Tehran, Iran. IEEE second workshop.

[3] Akoglu, A.M., Jonsson, S., Cakir, Z., Ergintav, S., Dogan, U., Feng, G., Zabcı, C., 2012. The Surface Deformation and Source Parameters of the October 23rd, 2011, Mw 7.1 Van (Turkey) Earthquake from InSAR, GPS and Field Observations. EGU General Assembly, Vienna, Austria.

[4] Ambraseys, N.N., Melville, C.P.,1982. A History of Persian Earthquakes. Cambridge University Press, New York.

[5] Anderssohn J., WetzelH-U., Walter T.R., Motagh M., Djamour Y., Kaufmann H., 2008, Land subsidence pattern controlled by old alpine basement faults in the Kashmar Valley, northeast Iran: results from InSAR and levelling. Geophysical Journal International.1-8.

[6] Bell J.W., Amelung F., Ferretti A., Bianchi M., Novali F., 2008. Permanent scatterer InSAR reveals seasonal and long-term aquifer-system response to groundwater pumping and artificial recharge, Water Resources Research, VOL. 44, W02407, doi:10.1029/2007WR006152.

[7] Berardino, P., Fornaro, G., Lanari, R., Sansosti E., 2002. A new algorithm for surface deformation monitoring based on small baseline differential SAR interferograms. IEEE Trans. 245 Geosci. Remote Sens. 40, 2375–2383.

[8] Berberian, M.,1994. Natural hazards and the first earthquake catalogue of Iran. VOL1, 266–270.

[9] Berberian, M., Arshadi, S., 1976.On the evidence of the youngest activity of the North Tabriz Fault and the seismicity of Tabriz city. Geol. Surv. Iran. 39, 397–418.

[10] Bürgmann, R., Rosen, P., Fielding, E., 2000. Synthetic aperture radar interferometry to measure Earth's surface topography and its deformation.Annu. Rev. Earth Planet. Sci. 28, 169–209.

[11] Cakir, Z., Ergintav, S., Ozener, H., Dogan, U., Akoglu, A., Meghraoui, M., Reilinger, R., 2012. Onset of aseismic creep on major strike slip faults. Geology v. 40; no. 12, 1115–1118.).

[12] Copley, A., Jackson J., 2006. Active tectonics of the Turkish-Iranian Plateau.Tectonics 25, TC6006.

[13] Dehghani, M., ValadanZoej, M.J., Entezam, I., Mansourian, A., Saatchi, S., 2009.InSAR monitoring of progressive land subsidence in Neyshabour, northeast Iran.Geophys. J. Int. 178, 47–56.

[14] Djamour, Y., Vernant, P., Nankali, H.R., Tavakoli, F., 2011. NW Iran-eastern Turkey present-day kinematics: Results from the Iranian permanent GPS network. Earth Planet. Sci. Lett. 307, 27–34.

[15] Elliott, J.R., Biggs, J., Parsons, B., Wright, T.J., 2008. InSAR slip rate determination on the Altyn Tagh Fault, northern Tibet, in the presence of topographically correlated atmospheric delays. Geophys. Res. Lett. 35, L12309.

[16] Ferretti, A., Prati, C., Rocca, F., 2001. Permanent scatters in SAR interferometry. IEEE Trans. Geosci. Remote Sens. 39(1), 8–20.

[17] Gabriel, A.K., Goldstein, R.M., Zebker, H.A., 1989. Mapping small elevation changes over large areas: Differential radar interferometry.J.Geophys.Res.94(B7): 9183–9191.

[18] Galloway D.L, Hudnut K.W, Ingebritsen S.E, Phillips S.P, Peltzer G, Rogez F, Rosen P.A (1998) Detection of aquifer system compaction and land subsidence using interferometric synthetic aperture radar, Antelope Valley, Mojave Desert, California. Water Resources Research 34 (10), 2573–2585.

[19] Gourmelen, N., Dixon, T.H., Amelung, F., Schmalzle, G., 2011. Acceleration and evolution of faults: An example from the Hunter Mountain–Panamint Valley fault zone, Eastern California. Earth Planet. Sci. Lett. 337–344.

[20] Haddadan M, Zohrab E (1994) Hydrogeology map of Tabriz. Geological Survey of Iran, 1:50000.

[21] Hanssen R.F (2001) Radar Interferometry: Data Interpretation and Error Analysis. Kluwer Academic, Dordrecht.

[22] Hessami, K., Pantosi, D., Tabassi, H., Shabanian, E., Abbassi, M., Feghhi, K., Solaymani, S., 2003a. Paleoearthquakes and slip rates of the North Tabriz Fault, NW Iran: preliminary results. Ann. Geophys. 46, 903–915.

[23] Hessami, K., Jamali, F., Tabassi, H., 2003b, Major active faults of Iran: Tehran, Iran, International Institute of Earthquake Engineering and Seismology, 1 sheet, scale 1:2,500,000.

[24] Hoffmann J., Zebker H.A, 2001, Seasonal subsidence and rebound in Las Vegas Valley, Nevada, observed by synthetic aperture radar interferometry, Water Resources Research, VOL. 37, NO. 6, 1551–1566.

[25] Hooper, A., Zebker, H., Segall, P., Kampes, B., 2004.A new method for measuring deformation on volcanoes and other natural terrains using InSAR persistent scatterers.Geophys. Res. Lett. 31, L23611.

[26] Hooper, A., Segall, P., Zebker, H., 2007.Persistent Scatterer InSAR for Crustal Deformation Analysis, with Application to Volcán Alcedo, Galápagos, J. Geophys. Res. 112, B07407, doi:10.1029/2006JB004763.

[27] Hooper, A., 2008. A multi-temporal InSAR method incorporating both persistent scatterer and small baseline approaches. Geophys. Res. Lett. 35, L16302.

[28] Hosseini, S. K., (2012). Two source faults of Ahar-Varzaghan Earthquakes, August 11, 2012,NWIran.Earthquake Research Center Ferdowsi University of Mashhad.

[29] Jaeger, J. C., and Cook, N. G. W., (1979).Fundamentals of Rock Mechanics.3rd edition.

[30]Jackson,J.,1992.Partitioningof Strike slip and Convergent Motion Between Eurasia and Arabi a in Eastern Turkey and the Caucasus.J. Geophys. Res. 97 (B9) 12471–12479.

[31] Karakhanian, A., Trifonov, G., Philip, H., Avagyan, A., Hessami, K., Jamali, F., Bayraktutan, M., Bagdassarian, H., Arakelian, S., Davtian, V., Adilkhanyan, A., 2004. Active faulting and natural hazards in Armenia, eastern Turkey and Northern Iran. Tectonophysics 380, 189–219.

[32] Kabiri, K., Pradhan, B., Sharifi, A., Ghobadi, Y., Pirasteh, S., 2012. Manifestation of Remotely Sensed Data Coupled With Field Measured Meteorological Data for an Assessment of Degradation of Urmia Lake, Iran. VOL6, Asia Pacific Conference on Environmental Science and Technology (APEST), Kuala Lumpur, Malaysia.

[33] Kampes, B., Usai, S., 1999. Doris: The delft object-oriented radar interferometric software. In: Proc. 2nd International Symposium Operationalization of Remote Sensing. http://citeseerx.ist.psu.edu/viewdoc/summary?doi=10.1.1.46.1689.

[34] KarimzadehS,CakirZ,OsmanoğluB,SchmalzleG,MiyajimaM,AmiraslanzadehR (2013) InterseismicstrainaccumulationacrosstheNorthTabrizFault(NWIran) deducedfromInSARtimeseries.Journal of Geodynamics, 66, 53–58.

[34] Karimzadeh S., Ahmadi F. (2013). Using Advanced Space-borne Radar Technology for Detection and Measurement of Land Subsidence and Interseismic Slip Rates, the Case Study: NW Iran. Studies in Surveying and Mapping Science, 1: 1-9.

[35] Kim, S.-W., Wdowinski, S., Dixon, T.H., Amelung, F., Kim, J.W., Won, J.-S., 2010. Measurements and predictions of subsidence induced by soil consolidation using persistent scatterer InSAR and a hyperbolic model. Geophysical Research Letters 37, L05304.

[36] King, G. C. P., Stein, R.S., Lin, J., (1994). Static stress changes and the triggering of earthquakes.Bulletin of the Seismological Society of America, 84, 935-953.

[37] Lu Z., Danskin W.R., 2001, InSAR analysis of natural recharge to define structure of a ground-water basin, San Bernardino, California, Geophysical Research Letters, VOL. 28, NO. 13, PAGES 2661-2664.

[38] Lubis A.M, Sato T, Tomiyama N, Isezaki N, Yamanokuchi T (2011) Ground subsidence in Semarang-Indonesia investigated by ALOS–PALSAR satellite SAR interferometry. Journal of Asian Earth Sciences, 40, 1079–1088.

[39] Lyons, S., Sandwell D., 2003.Fault-creep along the southern San Andreas from InSAR, permanent scatterers, and stacking.J. Geophys.Res.108, 2047, 24 PP.

[40] Madani, K., 2014. Water management in Iran.what is causing the looming crisis?. Journal of Environmental Studies and Sciences, 4, 315–328.

[41] Masson, F., Djamour, Y., Van Gorp, S., Chery, J., Tatar, M., Tavakoli, F., Nankali, H., Vernant P., 2006. Extension in NW Iran driven by the motion of the South Caspian Basin.Earth Planet. Sci. Lett.252, 180–188.

[42] Massonnet, D., Rossi, M., Carmona, C., Adragna, F., Peltzer, G., Feigl, K., Rte, T., 1993.The displacement field of the Landers earthquake mapped by radar interferometry. Nature, 364, 138–142.

[43] Massonnet, D., Fiegl, K.L., 1998. Radar Interferometry and its application to changes in the earth's surface. Rev. Geophys. 36(4), 441–500.

[44] Moghaddam A.A, Najib M.A (2006) Hydrogeologic characteristics of the alluvial tuff aquifer of northern Sahand Mountain slopes, Tabriz. Iran Hydrogeology Journal, 14, 1319–1329.

[45] Moghtased-Azar, K., Mirzaei, A., Nankali, H.R., Tavakoli, F., 2012. Investigation of correlation of the variations in land subsidence (detected by continuous GPS measurements) and methodological data in the surrounding areas of Lake Urmia.Nonlin. Processes Geophys. 19, 675–683.

[46] Motagh, M., Hoffmann, J., Kampes, B., Baes, M., Zschau, J., 2007. Strain accumulation across the Gazikoy–Saros segment of the North Anatolian Fault inferred from Persistent Scatterer Interferometry and GPS measurements. Earth Planet. Sci. Lett. 255, 432–444.

[47] Motagh, M., Walter, T.R., Sharifi, M.A., Fielding, E., Schenk, A., Anderssohn, J., Zschau, J., 2008. Land subsidence in Iran caused by widespread water reservoir overexploitation. Geophys. Res. Lett. 35, L16403.

[48] Nwankwor G.I., Egboka B.C.E (1992) Leakage properties of the multi-aquifer system underlying the Greater Onitsha water scheme borehole field, Anambra State, Nigeria. Hydrological Sciences Journal 37 (6), 557–566.

[49] Razzaghmanesh, M., Salemi, T., Seraj, M., 2006.Ground water quality and quantity of Tabriz plain.National Conference on Irrigation and Drainage Network Management (In Persian).

[50] Reilinger, R., McClusky, S., Vernant, P., Lawrence, S., Ergintav, S., Cakmak, R., Ozener, H., Kadirov, F., Guliev, I., Stepanyan, R., Nadariya, M., Hahubia, G., Mahmoud, S., Sakr, K., ArRajehi, A., Paradissis, D., Al-Aydrus, A., Prilepin, M., Guseva, T., Evren, E., Dmitrotsa, A., Filikov, S.V., Gomez, F., Al-Ghazzi, R., Karam, G., 2006. GPS constraints on continental deformation in the Africa Arabia-Eurasia continental collision zone and implications for the dynamics of plate interactions.J.Geophys.Res. 111, B05411.

[51] Riley F.S (1969) Analysis of Borehole Extensometer Data from Central California. International Association of Scientific Hydrology Publication,89, 423–431.

[52] Rizza M, Vernant P, Ritz J.F, Peyret M, Nankali H, Nazari H, Djamour Y, Salamati R, Tavakoli F, Chery J, Mahan S.A, Masson F (2013)Morphotectonic and geodetic evidence for a constant slip-rate over the last 45 kyr along the Tabriz fault (Iran). Geophysical Journal International, 193, 1083–1094.

[53] Roberts, G.P., Cowie, P.A., Papanikolaou, I., Michetti, A.M., 2004. Fault scaling relationships, deformation rates and seismic hazards: an example from the Lazio-Abruzzo Apennines, central Italy. J. Struct. Geol. 26, 377–398.

[54] Savage, J., Burford, R., 1973.Geodetic determination of relative plate motion in Central California.J. Geophys. Res. 78, 832–845.

[55] Schmidt, D.A., Bürgmann, R., 2003. Time dependent land uplift and subsidence in the Santa Clara valley, California, from a large InSAR data set. J. Geophys. Res., 108, doi:10.1029/2002JB002267.

[56] Sedighi M, Nankali H.R, Arabi S, Tavakoli F (2010) Subsidence Detection in Salmas Area Using InSAR and Geodetic Techniques. Geospatial Engineering Journal, 1(4).

[57] Segall, P., 2002. Integration of geologic and geodetic estimates of fault slip rates on the San Andreas system. Int. Geol. Rev. 44, 62–82.

[58] Sousa, J.J., Hooper, A.J., Hanssen, R.F., Bastos, L.C., Ruiz, A.M., 2011. Persistent scatterer InSAR: a comparison of methodologies based on a model of temporal deformation vs. spatial correlation selection criteria. Remote Sens. Environ. 115 (10), 2652–2663.

[59] Stein, R.S., and Lisowski, M., (1983). The 1979 Homestead Valley earthquake sequence, California:control of aftershocks and postseismic deformation. Journal of Geophysical Research 88,6477-6490.

[60] Stein, R. S., Barka, A. A., and Dieterich, J. H. (1997). "Progressive failure on the North AnatolianFault since 1939 by earthquake stress triggering." Geophysical Journal International, 128,594-604.

[61] Takeo, I., Kunihiko, S., Hiroshi, T., Yoshiko, Y., and Kenji, S., (2011). Correlation betweenCoulomb stress changes imparted by large historical strike-slip earthquakes and current seismicityin Japan. Earth Planets Space, 63, 301–314.

[62] Toda, S., Stein, R. S., Reasenberg, P. A. Dieterich, J. H., and Yoshida, A., (1998). Stress transferredby the 1995 Mw = 6.9 Kobe, Japan, shock: effect on aftershocks and future earthquakeprobabilities. Journal of Geophysical Research, 103, 543-565.

[63] Tatar, O., Poyraz, F., Gursoy, H., Cakir, Z., Ergintav, S., Akpinar, Z., Kocbulut, F., Sezen, F., Türk, T., Hastaoglu, K.O., Polat, A., Mesci, B.L., Gursoy, O., Ayazlı, I.E., Cakmak, R., Belgen, A., Yavasoglu, H., 2012. Crustal deformation and kinematics of the Eastern Part of the North Anatolian Fault Zone (Turkey) from GPS measurements. Tectonophysics 518–521, 55–62. Toksoz, M.N., Arpat, E., Saroglu, F., 1977.East Anatolia earthquake of 24 November, 1976. Nature 270, 423–425.

[64] Tomás, R, Herrera, G, Delgado, J, Lopez-Sanchez, J.M, Mallorquí, J.J, Mulas, J (2010)A ground subsidence study based on DInSAR data: calibration of soil parameters and subsidence prediction in Murcia City (Spain). Engineering Geology 111, 19–30.

[65] Vernant, P.,Nilforoushan, F., Hatzfeld, D., Abbassi, M.R., Vigny, C., Masson, F., Nankali, H., Martinod, J., Ashtiani, A., Bayer, R., Tavakoli F., Chery, J., 2004.Present-day crustal deformation and plate kinematics in the Middle East constrained by GPS measurements in Iran and northern Oman.Geophys. J. Int. 157, 381–398.

[66] Wells, D.L., Coppersmith, K.J., 1994. New empirical relationships among magnitude, rupture length, rupture width, rupture area, and surface displacement. Bull. Seismol.Soc. Am. 84, 974–1002.

[67] Westaway, R., 1990. Block Rotation in Western Turkey 1. Observational Evidence.J.Geophys. Res. 95, B12, 19857–19884.

[68] Wright, T., Parsons, B., Fielding, E., 2001.Measurement of interseismic strain accumulation across the North Anatolian Fault by satellite radar interferometry.Geophys. Res. Lett. 28, 2117–2120.

[69] Zebker, H.A., Rosen, P.A., Hensley S., 1997, Atmospheric effects in interferometric synthetic aperture radar surface deformation and topographic maps.J. Geophys.Res.102(2), 7547-7563.

4. A GIS based tool for seismic microzonation and damage assessment (Tabriz city)

4.1 General remarks

One of the basic necessities of disaster management for cities during (co-), after (post-) or even before (pre-) an earthquake is the provision of a well-enriched geodatabase. This database helps engineers and urban planners to predict future events, which allows them to design better strategies for the future of cities. A spatially based earthquake scenario to plan for quick responses is the basis of urban preparation and earthquake disaster management using decision-making techniques.

Disasters, such as earthquakes, floods and fires, significantly affect the community and infrastructures. Most natural phenomena are characterized by short action, but their impacts, such as that on buildings or other tangible structures, persists for years. The presented analytical risk models enhance the ability and resilience of experts and urban planners against natural disasters. A glimpse of the hazard-damage assessment models shows that each of the models uses specific parameters and formulation approaches and can be categorized in two main classes: (1) worldwide models and (2) local (case-based) models. A principal example for the first category is the Prompt Assessment of Global Earthquake for Response (PAGER) operated by USGS, which reports economic losses and estimates the people exposed to varying levels of ground shaking. It can give a report within 30 minutes after a significant earthquake (usually for events greater than magnitude 5.5) [1]. However, the information on the extent of shaking is not accurate in the first hours after an earthquake due to the spatial variability of ground motion. The use of seismic data and intensity reports typically improves this information (for details see [1-3]). HAzards United States (HAZUS) is an example of the second category. It is a multi-hazard model for the three main natural disasters in the US, i.e., earthquakes, winds and floods, that was developed by the Federal Emergency Management Agency (FEMA) [4,5]. It operates on the Arc Map interface and estimates physical damages (i.e., buildings, pipeline networks) and social damage (i.e., casualties) based on damage functions and census tract areas, respectively. It has been used for the pre-disaster mitigation of most counties in the United States, such as Yuba in California, Harris in Texas, etc. [6,7]. Çinicioğlu et al. [8] presented an integrated damage-causing model including (1) ground shaking as a primary effect, (2) landslide, liquefaction and seismic bearing capacity as collateral effects. This method considered each effective phenomenon separately and in combination for two districts, Bakırköy and Ömerli, in Istanbul city. Ansal et al. [9] presented a seismic microzonation and earthquake damage scenario for Zeytinburnu in Istanbul. They first generated different microzonation maps with respect to ground shaking parameters (i.e., fault

orientation, magnitude, fault geometry) for the selected earthquake scenario. To evaluate the seismic vulnerability for buildings, they calculated the site-specific short period (T=0.2) and long period (T=1) spectral accelerations and PGAs. Second, region-specific vulnerability curves were used to estimate building damage in Zeytinburnu. Third, the natural gas pipeline damage was estimated via empirical correlations (PGV vs. pipeline damage) and gas pipeline inventories. Armaş [10] presented a multi-criteria vulnerability assessment for an earthquake model of Bucharest city in Romania that uses several raster indicators. Each indicator (i.e., acceleration value of an earthquake and/or population) provides spatial information on a set of defined criteria (i.e., environmental or social vulnerability). They are processed and classified in "criteria trees" according to their weight to vulnerability. Cole et al. [11] estimated the rate of expected building damage in three quarters of Shanghai in China using attenuation Gumbel relationships and a building damage factor. Hashemi and Alesheikh [12] modified the intensity of earthquakes to investigate the impacts of ground shaking on building damages, population vulnerability and street blockage in district 10 of metropolitan Tehran, Iran. Hassanzadeh et al. [13] presented a user-friendly Karmania Hazard Model (KHM) for Kerman city in Iran. KHM features an interactive environment that combines spatial data layers and the vulnerability coefficients of buildings and the population to the estimate rate of building damage, causalities and required resources for survivors and injured people. It was conceptualized and developed by a group of researchers at the Kerman Disaster Management Center (KDMC) and was validated based on the (1) Seismic intensity, (2) rate of damaged buildings and number of deaths and (3) the report of post-earthquake demands for the Bam earthquake. In this study, the ArcGIS package enabled us to transform parameters into actionable information. All parameters, such as the geological characteristics, predominant period of soil and shear wave velocity, geoid gradient, types of sediment, alluvial thickness and ground water table, are converted to shape files, classified and finally integrated in a relational geodatabase to evaluate the damage of structures and rate of fatalities and injuries in district two of Tabriz city. Next, we present the post-earthquake demands of the study area. The results indicate that 69.5% of buildings are totally destroyed, and the rate of fatalities is approximately 33%, which we attribute to the high damage level in section 4.However,this rate is generally related to the structural system and occupancy level of a residential building, which are two important criteria in each vulnerability project.

4.2 Characterization of the study area

Metropolitan Tabriz, with a population of over 1.5 million people,consists of 10 regions. In terms of land area, it is the second largest city of Iran, which contains approximately 25 km^2 of old architecture [14]. The city developed between the Eynali and Sahand mountains in the North and South, respectively. According to the topography of the study area, the slope slightly decreases from east to west and opens to the Tabriz basin. The city, which is the capital of the Eastern-

Azerbaijan province, is situated in NW Iran at 38.08ºN, 46.25ºE. The GPS constrains and earthquake focal solutions of past earthquakes in NW Iran performed by Jackson 1992 [15] and McClusky et al. [16] indicate that a convergence of 22±2 mm/yr between the northward motion of the Arabian plate relative to the Eurasian plate results in the emergence of numerous thrust and strike-slip faults in this region (Fig. 4.1).
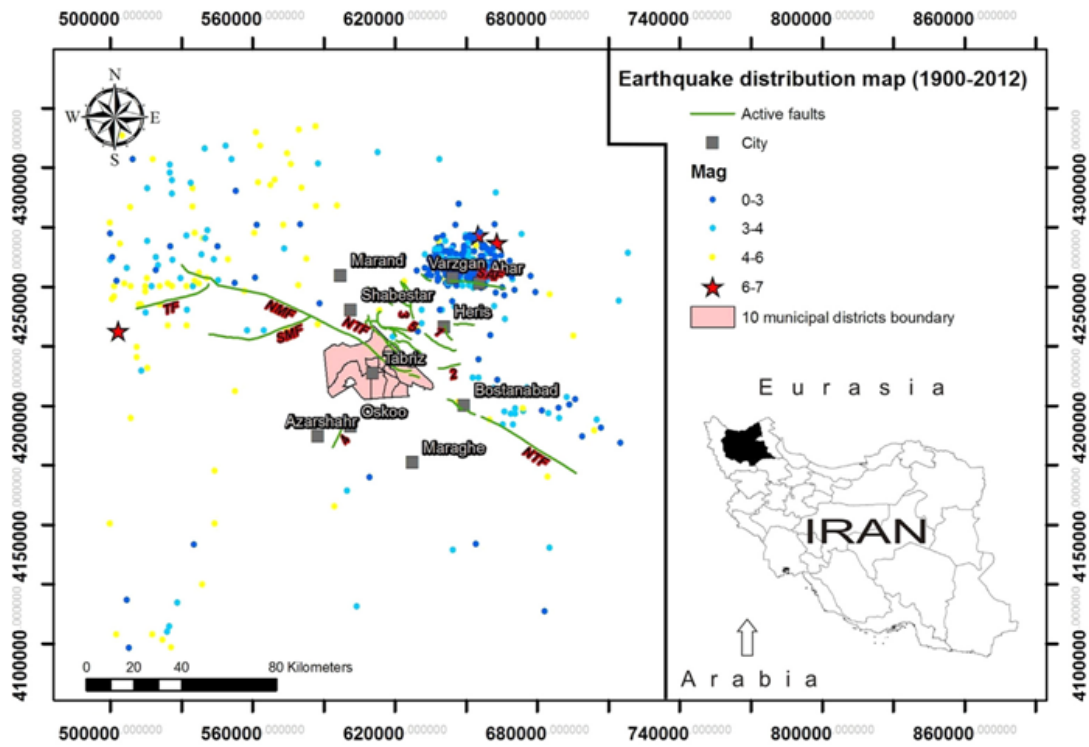
Fig.4.1 Summarized structuralmapoftheEast-AzerbaijanprovinceofIranadoptedfromHessamietal. [21].
Seismicityisbasedon Berberian [22],
CentroidMomentTensorandtheInternationalInstituteofEarthquakeEngineeringandSeismologycatalogsbetwee n1900and2012.North
TabrizFault(NTF);SouthMishoFault(SMF);NorthMishoFault(NMF);TasujFault(TF);andSouthAharFault(SA F).

Westaway [17] and Jackson [15] believe that strike-slip faults (i.e., North Tabriz Fault, Gilatu-Siyah Cheshmeh-Khoy Fault and Chalderan Fault) appear to be the continuation of the North Anatolian Fault into NW Iran. Some of these fault segmentsruptured during the 1930, 1966 and 1976 earthquakes and trailed surface deformations [17-20]. The following are the last major earthquakes caused by the North Tabriz Fault (NTF) in the 18th century: the first occurred in 1721 (Ms 7.3) at 37.9ºN, 46.7ºE, and the second one occurred in 1780 (Ms 7.4) at 38.12ºN, 46.29ºE [22]. The locations and elapsed time are related to a region of high seismic activity for both the SE and NW segments of the North Tabriz Fault. However, the initial seismic hazard assessment requires an estimated value of a potential earthquake in a specific area caused by a specific fault.

The estimated magnitude and perceivable intensity in Tabriz are calculated for dataset of faults using different empirical equations and are summarized in Table 4.1. Due to the length of the fault and adjacency to the site, the NW segment of the NTF poses a stronger seismic hazard. Moreover, a time series analysis of RADAR images in the study area between 2004-2010supports a probable earthquake of M ~ 7 as a result of strain accumulation across the North Tabriz Fault [23]. The average thickness of the lithosphere was estimated from gravimetric measurements to be approximately 40 km for NW Iran [24]. The statistical results of instrumental earthquake catalogues in NW Iran with a radius of 150 km indicate that the seismogenic depth is approximately 20 km and fewer daytime than nighttime earthquakes are recorded [25]. Due to the poor instrumental records of smaller events in recent decades, the magnitude of most earthquakes in this radius ranges from M 4 to M 4.5. An increasing trend of M 4 to M 4.5 earthquakes is not evident during this time. This finding conflicts with the Gutenberg-Richter law, which confirms that smaller events have not been recorded well [25]. The last seismic event of the study area occurred on the 11th of August 2012 in the Ahar region of NW Iran. The epicenter of the earthquakes was 60 km away from Tabriz city. The intensity felt in Tabriz was V (MMI), and the group of aftershocks continued for eight months (Fig. 4.1).

Table 4.1 Seismic parameters of distinguished faults of the study area (see Fig. 4.1 for their location).

Fault name	Length (km)	Magnitude of possible earthquake				Average magnitude	Perceivable MMI in Tabriz
		Nowroozi [26]	Wells and Coppersmith [27]	Mohajer and Nowroozi [28]	Bonilla et al. [29]		
NW-NTF	45	6.7	7	7	7.5	7	IX+
SE-NTF	46.5	6.7	7	7	7.6	7.1	VII
SMF	45	6.7	7	7	7.6	7	VIII
NMF	42	6.6	6.7	7	7.5	7	VII
TF	32.5	6.5	6.8	6.9	7.3	6.9	VI
SAF	40	6.5	6.7	6.4	6.7	6.6	VII
1	14	6	6.3	6.5	6.6	6.3	VII
2	9.5	5.8	6.2	6.3	6.3	6.2	VII
3	15.3	6	6.4	6.6	6.7	6.4	VII
4	13.2	6	6.3	6.5	6.6	6.4	VII
5	10.2	5.9	6.2	6.4	6.4	6.2	VII

Estimating the seismic hazard for different parts of the world requires a number of different methods and parameters. The database could affect other steps of seismic microzonation. Therefore, a standard approach to assess damage has been lacking. This study benefits from a relational geodatabase for query and calculation in which all data are represented in terms of tuples and grouped into relations. We attempted to increase the number of new parameters that

are effective in the Iranian seismic zone. Consequently, each parameter for a hierarchy process approach requires a specific weight based on expert judgments. We used the KHM standard method, which is designed for building and human losses in Iran, and then extruded a 3D scene of demolished buildings. Based on a GIS-upheld database, the principal tasks of the presented earthquake scenario can be followed in 3 steps (Fig. 4.2).
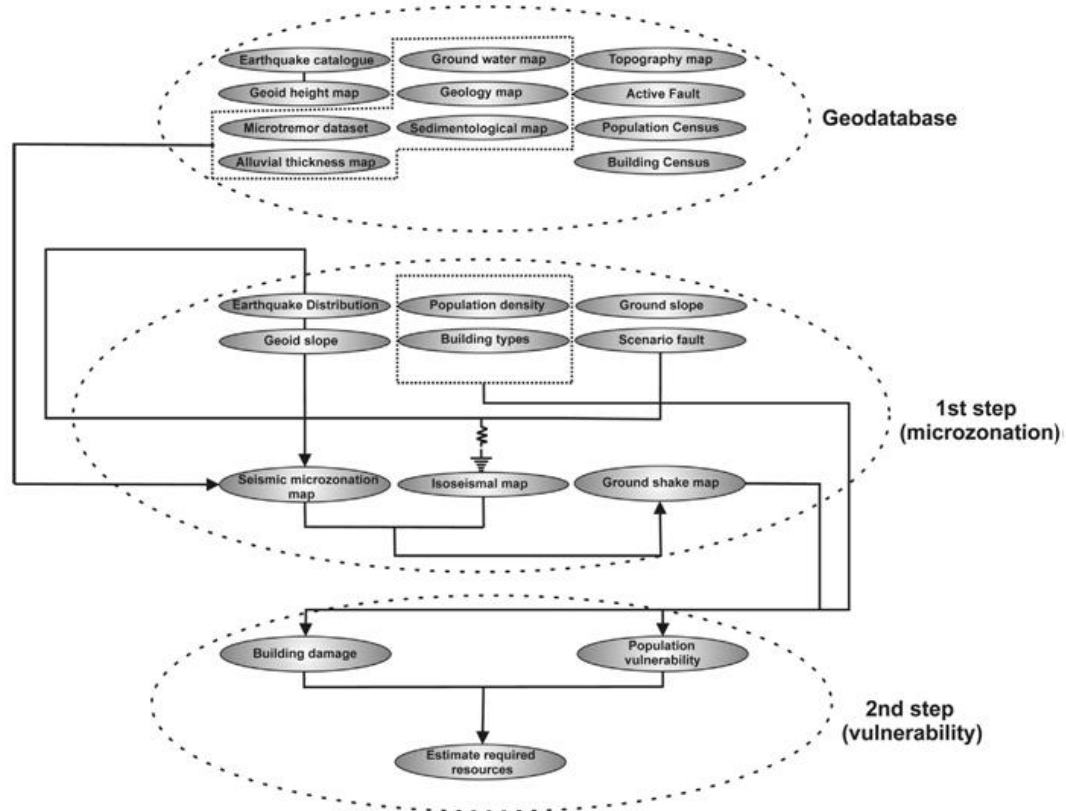
Fig.4.2 Flow chartofearthquakescenariomodel.

4.3 Methodology

4.3.1 Database preparation

At this stage, different data are gathered and adopted to be utilized in the ArcGIS environment. An earthquake catalogue was obtained from the International Institute of Earthquake Engineering and Seismology (IIEES) and modified with the first earthquake catalogue [22]. The modified catalogue was tabulated based on the geographic coordinate, depth (km) and earthquake magnitude in a year/month/day format. The Geological Survey of Iran (GSI) provided the geology map at a scale of 1:100000. This map shows that NW Iran is well defined with various lithologies and ages [30]. The residential districts of Tabriz contain the Cenozoic and Quaternary units. The Cenozoic units persisted from the Miocene to the Quaternary. Younger terraces, gravel fans and salty-gypsiferous deposits lie on the residential parts of our target district (Fig. 4.3a) [30,31]. The

ASTER digital elevation model (30 m posting) was used to evaluate the terrain slope (Fig. 4.3b). The Tabriz region starts with a gentle slope from the east to the west. Elevations vary from 1750 m in the east to 1300 m in the west. The average topographical height in district two was estimated to be approximately1500 m. The geoid slope map, which is based on the geoid map, is another parameter of the seismic microzoning project of Tabriz (Fig. 4.3c). This map is prepared by the International Center for Global Earth Models (ICGEM). Simply put, the geoid is the fundamental surface that describes the figure of the Earth. It can be described as the equipotential surface of Earth's gravity field. The geoid value of NW Iran ranges from 15 to 25 m. The last integrated investigation of seismology data and the geoid gradient of Iran reveals a significant spatial correlation between the locations of past earthquakes and geoid slope, because all Iranian earthquakes with magnitudes greater than 6 were located in areas of higher geoid slopes that exceed 7.5% [32,33].

The alluvial thickness and ground water table information for Tabriz were provided by the Regional Water Organization in X, Y and Z format (Fig. 4.3 d and e). To identify how the soil condition could amplify earthquake waves, we used the shear wave velocity and microtremor measurements of 21 stations in different parts of Tabriz (Fig. 4.3e) to categorize the soil types based on Table 4.2 [34]. The sedimentology map was extracted from the geotechnical studies of GSI as well as the exploration studies of a subway project in the city [30,31,35]. Overall, 149 boreholes and shallow wells were excavated in the study area (Fig. 4.3f). The average depth of boreholes was approximately 30 m. Various tests were conducted to study the compressibility of subsurface layers, such as a Standard Penetration Test (SPT) and pressuremeter test. According to the drilling results, the surface layers mostly consist of alluvial deposits, while some boreholes are dominated by weak stone layers such as siltstone, clay stone and conglomerate [31].

The above collected data from the institutes are normally discrete, and the number of observations is sometimes inconsistent between parameters. Therefore, they were not reliable for all processes. For example, the ground water table was estimated from many wells (>2000) in the region, but the data were obtained under differing circumstances. To resolve this discrepancy, all data are refined, and the uncertainties in gap areas must be reduced. Subsequently, the dimension matrices of all contributors must be the same. A set of sample points with discrete spatial modalities (i.e., earthquake distributions, water wells, geoid slope and etc.) that represent the changes in the landscape or environment can be used to visualize the continuity and variability of collected data across a surface via the use of interpolation tools in ArcGIS. Interpolation is a technique that changes the functionality of a set of point data to grid data. For a grid that represents a surface, each cell (pixel) contains an attribute value that represents a change in the Z value (if X and Y are assumed to represent location), which is the third dimension of the matrix. However, interpolation tools incorporate limits to control surface behavior because the operation must sometimes be

stopped across linear features (i.e., faults). The Kriging interpolation tool is the most famous and powerful statistical method. The Kriging approach assumes that the distance or direction between given points reflects a spatial correlation than can be used to express the gap variation in the surface. It fits a function to a specific number of points or all points (maximum point) within a specific radius to determine a reliable output value for each location. The Kriging approach is especially appropriate when a spatially correlated distance or direction is known. Therefore, it is the most popular interpolation method for applications in soil sciences and geology. In this study, we used a simple Kriging method to predict the unknown Z values on the surface of all parameters. The unknown $\hat{Z}(X_i, Y_i)$ value at coordinates (X_i, Y_i) can be calculated with the following equation:
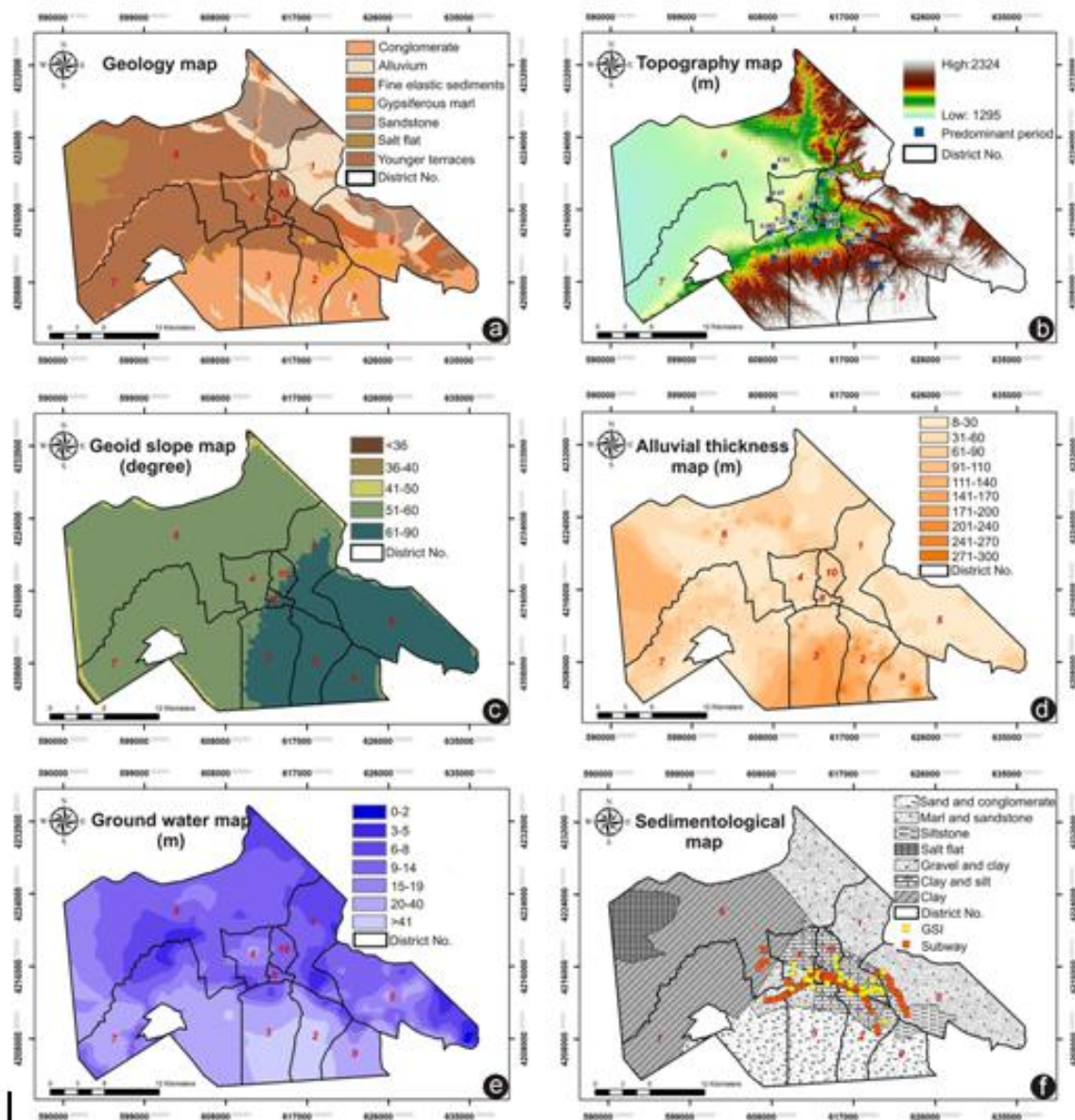
Fig.4.3 Effective local factors in the regions of the ten municipalities of Tabriz city.

Table 4.2 Soil profile classification based on Iranian Code of Practice for Seismic Resistant Design of Buildings: Standard No. 2800 [36].

Soil type	Description	V_s(m/sec)
I	a) Igneous rock (with coarse and fine grade texture), stiff sedimentary rocks and massive metamorphic rocks and conglomerate.	> 750
	b) Stiff soils (compact sand and gravel, very stiff clay) with a thickness more than 30 m above the bedrock.	$375 \leq V_s \leq 750$
II	a) Loose igneous rocks (i.e., tuff), loose sedimentary rocks, foliated metamorphic rocks and in general rocks that have become loose and decomposed due to weathering	$375 \leq V_s \leq 750$
	b) Stiff soils (compact sand and gravel, very stiff clay) having a thickness more than 30 m above the bedrock.	$375 \leq V_s \leq 750$
III	a) Rocks that are disintegrated due to weathering.	$175 \leq V_s \leq 375$
	b) Soils with medium compaction, layers of sand and gravel with medium intra-granular bond and clay with intermediate compaction.	$175 \leq V_s \leq 375$
IV	a) Soft deposits with high moisture content due to high level of water table. b) Any soil profile containing clay with a minimum thickness of 6 m and a plastic index and moisture content exceeding 20 and 40 percent, respectively.	<175

$$\hat{Z}(X_i, Y_i) = \sum_{\alpha=1}^{n} W_{ij\alpha} \times Z_\alpha \ (4.1)$$

Where n is the number of known values; Z_α. $W_{ij\alpha}$ is a set of weight factors for each point. The weight factors are calculated by finding the semi-variogram values for all distances between input points the semi-variogram values for all distances between an unknown pixel and all input points; a set of simultaneous equations must then be solved. Points closer to an unknown pixel bear greater weight, while those farther away bear a lesser weight (Fig. 4.4) [37].
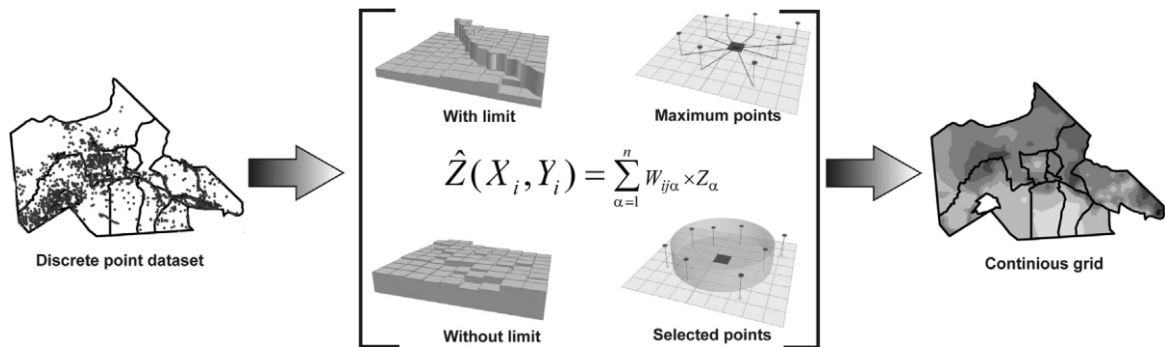
Fig.4.4 ProcedureforKriginginterpolationofdiscrete Z values.

4.3.2 Seismic analysis

As discussed, the North Tabriz Fault (NTF) is a prominent tectonic feature in the vicinity of the city. Future earthquakes in any of the segments of the NTF would significantly impact the buildings and population in Tabriz city, because the seismic activity of this fault is also high, as shown in Table 4.1. The Probabilistic Seismic Hazard Analysis (PSHA) method already was applied to thecityusing the popular logic trees approach for determining of ground motions. The minimum and maximum values of the Peak Ground Acceleration (PGA) for the return periods of 75, 475 and 2475 years were (0.13 g, 0.17 g), (0.22 g, 0.33 g) and (0.30 g, 0.8 g), respectively. The results also showed that amounts of PGA over the bedrock are highest and lowest in the northwestern and southeastern parts of Tabriz city, respectively [25]. Although PSHA has been well known as the best approach for seismic hazard studies, it suffers from some mathematic defects (i.e. it is more theoretical) that may lead to overly conservative public policy [38]. As an alternative, we followed a simple Deterministic Seismic Hazard Analysis (DSHA) model using the ArcGIS toolset because we believe that DSHA is more useful, especially where tectonic features are reasonably active and well defined, such as in the Tabriz region, and the seismic hazard is straightforward, such as that of the North Tabriz Fault. For example, DSHA is frequently used in California due to the knowledge of faults and the region's high seismicity [39-41]. However, this model does not treat uncertainties well. Uncertainties (epistmic or aleatory) have not been quantified in our results. The process consists of the following steps to generate a Ground Shake Map (GSK):

1- Identify nearby seismic source zones (i.e. the specific faults) (Fig. 4.1).

2- Identify proximity to site for each source.

3- Identify the length of the faults using the "Measure" toolbox in ArcGIS.

4- Identify the orientation (strike angle) of the fault using the "Linear Directional Mean" tool, which allows us to calculate the mean orientation for each identified fault.

5- Describe the amplification map.

Usually, ground shaking describes a relationship between the ground motion parameter (i.e. MMI), the earthquake magnitude, the distance from the site and uncertainties.

$$Ln(GSM) = f(M, R) + \delta \qquad (4.2)$$

where GSM is the ground shaking map (here we assume MMI), M is the magnitude of the earthquake, R is the source-to-site radius (raw intensity map) and δ are the uncertainties or residuals, which areindependent of M and R. Instead of the uncertainties, we defined the site

effect parameters inside of a normalized amplification map, which was followed by a weighting approach using AHP.

Although this procedure is approximate, it is also suitable for generating other shaking scenarios. The NW segment of the NTF, which was identified by location and magnitude, was selected as a simulated earthquake to identify the building and human vulnerability as well as estimate the basic demands for survivors. This segment was selected because it is the source of the strongest shaking level expected for the city of Tabriz. However, in case of building damage estimation, the ground shaking may not be the maximum credible event. Instead of assuming a "maximum capable" event, a "negotiated" event is considered in the DSHA due to its relatively conservative nature. The initial elements of the hypothesized fault are summarized in Table 4.3.

Table 4.3 Fault model elements of source earthquake.

NTF elements	Descriptions
Starting point in UTM coordinates (X,Y)	(624555.925,4213508.213)
Ending point in UTM coordinates (X,Y)	(584957.047,423450.388)
Reference point in UTM coordinates (X,Y)	(606924.994,422636.423)
Magnitude (M_w)	7
Length (km)	45
Strike (deg)	270
Dip (deg)	90

The attenuation of ground motion is the severity at which the earthquake is felt in a particular place. Its intensity decreases as the distance from the epicenter increases. In this study, the seismic intensity, specifically the Modified Mercalli Intensity (MMI) level, was assigned as a seismic input parameter because MMI involves the effects of local geology, the seismic source characteristics, duration and distance of the fault to the site. The fragility curves of the vulnerability analysis stage for different building classes in Iran were estimated as a function of MMI. Thus, MMI is more consistent as a ground motion parameter. However, other updated attenuation relationships have been introduced according to PGA or PGV, but they may not be consistent with the applied fragility curves [42,43].We used region-specific intensity attenuation relationships based on major Iranian earthquakes (22 earthquakes in different parts of Iran) to produce an isoseismal map (Eq. 4.3; 4.4) (Fig. 4.5a) [44,45].

$$I_0 = 1.3 \times M_s + 0.09 \quad (4.3)$$

$$I = 11.926 + (0.831 \times M_s) - 2.7 Ln(R + 22) \quad (4.4)$$

where M_s is the surface magnitude, I_0 is the intensity at the epicenter, R is the radius from the epicenter and R is the earthquake intensity at a specific place. Like the Karmania Hazard Model (KHM), we used Eq (3.3) and Eq (3.4) to generate a seismic intensity map. Both Eq (3.3) and Eq

(3.4) were deduced from an analysis of the isoseismal maps of previous earthquakes (elongated in the direction of local structural trend of causative faults) in different regions of Iran to study the attenuation of seismic intensity as a function of the distance from the epicenter under a certain surface wave magnitude (M_s). The amount of errors, M_s, in Eq (4.3) and Eq (4.4) were considerably reduced by using an iterative least squares fit procedure. These equations were derived from more basic concepts, which assumed that the intensity is proportional to the logarithm of the seismic energy density at any location based on empirical relationships [44,45].

If we consider the parameters that influence the microzonation, the results obtained from empirical attenuation relations could clearly be helpful to evaluate the effects of an earthquake. The parameters described in subsection 3.1 are systematically arranged according to the engineering judgment of the amplification coefficient of Tabriz city. Here, the analysis was carried out according to the Analytic Hierarchy Process (AHP) at two levels, which is a systematic approach for complex decisions based on mathematic and expert judgment. At the first level, each parameter is assigned a weight ranging from 0-1 based on its contribution to the amplification of earthquake waves. The weights assigned to each parameter are the geology and sedimentology (0.3), alluvial thickness (0.25), ground water table (0.25), predominant period (0.1) and geoid slope (0.1). At the second level, the elements of each parameter are assigned ranging from 1-9 based on pairwise judgment. For example, in thicker alluvial layers, the weight of this element positively correlates with the thickness in AHP processes because thicker unconsolidated sediment can amplify seismic waves (Fig.4.6).

After the arrangement, a cell-by-cell ($10*10$ m^2) arithmetic overlaying (Eq. 4.5) yields the amplitude map (Fig. 4.5b).

$$A_i = \sum G_i M_i T_i W_i S_i \qquad (4.5)$$

where A_i is the amplification map in area i; G_i is a combination of the geology and sedimentology maps; M_i is the microtremor measurements; T_i is the alluvial thickness; W_i is the ground water table and S_i is the geoid slope value. The seismic analysis step aims to quantify the earthquake ground shaking that may be experienced in the Tabriz metropolitan region. Consequently, the ground shaking map (Fig. 4.7) is produced via a combination of the raw intensity map and amplitude map (Eq. 4.6).

$$GSM = \sum A_i I_i \quad (4.6)$$

where GSM is the ground shaking map; A_i is the Amplitude map; I_i is the intensity map.
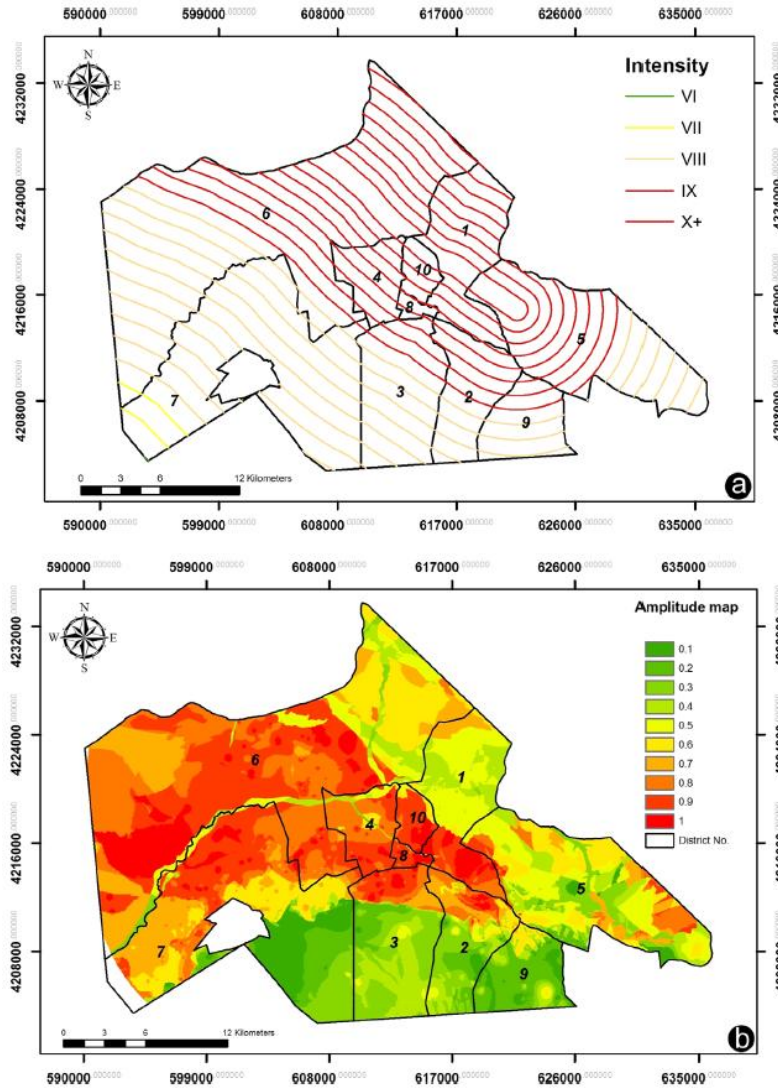
Fig. 4.5(a) Intensity map of a 7 magnitude earthquake (the roman numbers represent Modified Mercalli Intensity); (**b**) seismic amplitude map.
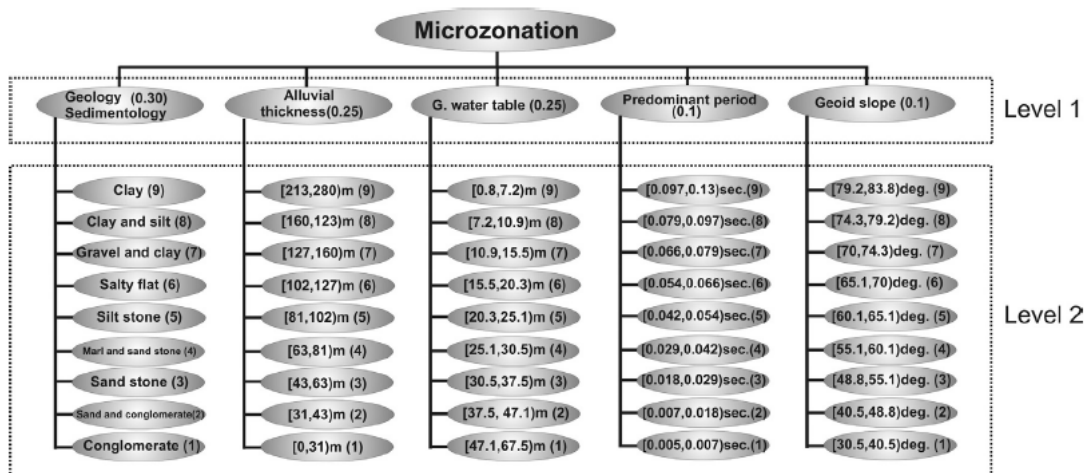
Fig.4.6 Final Analytical Hierarchy Process adoption for influential parameters.
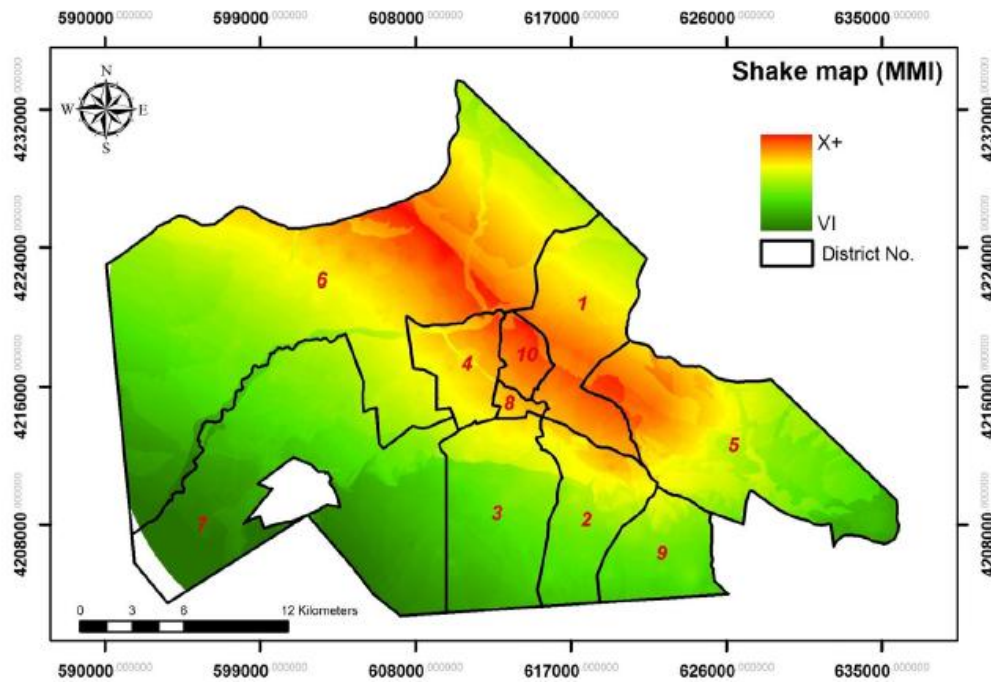
Fig.4.7

Groundshakingmapillustratingtheregionalextentofintensitythatcanbeexpectedfromamagnitude7earthquakeon
theNorthTabrizFault.

4.3.3 Vulnerability analysis

The word "vulnerability" is used to indicate the extent of damage that may be inflicted on buildings, communities or each geographic feature. When an earthquake occurs, a city and its components, such as urban transportation, the telecommunication network, households and buildings, are exposed to destruction risk and loss of their functionalities. Complex urban systems are heavily related to each other, and their functionality mostly depends on the other activities. Therefore, urban vulnerability not only depends on a particular component or section of the city but also on all components together.

4.3.3.1 Building vulnerability estimation

A comparison of the Manjil and Kocaeli earthquakes that occurred in Iran and Turkey, respectively, revealed that Iranian buildings are 1 grade weaker than Turkey's buildings, despite the same magnitude of earthquakes [46]. The JICA developed fragility curve functions for different types of buildings to evaluate the stability of buildings in Tehran (Fig. 4.8). The fragility curves on the MMI scale are determined based on several aspects: 1- the damage to different types of buildings observed for past Iranian earthquakes, such as the Ghir (1972), Ghaenat (1979), Lordegan (1992) and Ardekul (1997) earthquakes, and 2- the evaluation by JICA experts

according to Iranian building code and special welding techniques used for steel structures in Iran [46,47].
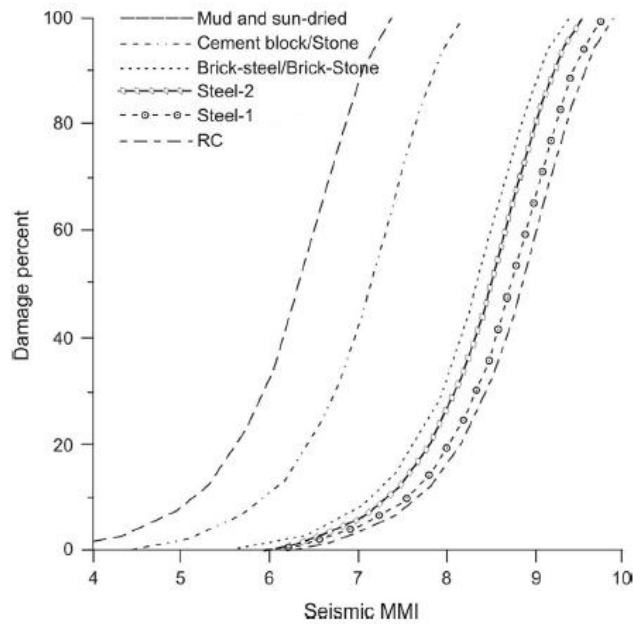
Fig.4.8 Fragilitycurvesof6buildingtypesinthestudyregionasafunctionofthe Modified MercalliIntensityscale(MMI) [46].

Building classification is a common method to differentiate buildings and help the reporting of details. Two essential items were considered to classify buildings in the study area according to Table 4.4: 1- their structural system, which is one of the important aspects of building vulnerability and 2- the number of stories. The building inventory provides 6 building categories for the study area; more precise damage/loss estimates require a more extensive building inventory, but extensive information of the year of construction, the lateral force resisting system and quality were not provided to us. Only a small number of cities in the world features such a "well-developed" building inventory.

Table4.4 Building classes, number of buildings, stories and descriptions.

Typology	Total number of building	Number of stories	Description
Steel-1 (A)	7967	1 to 3	Steel braced or moment resisting frame building
Reinforced Concrete (B)	1002	Multi-story	RC moment resisting or shear wall frame building
Steel-2 (C)	297	>3	Steel braced or moment resisting frame building
Brick-steel or brick stone (D)	15871	Multi-story	Surrounding masonry wall with interior steel column
Cement block and stone (E)	10	All included	All interior and exterior walls are made of cement blocks
Mud and sun-dried (F)	0	All included	Walls made of sun-dried adobe materials

The following building types were included in this study: steel-1 (31.06%), reinforced concrete (4%), steel-2 (1%), brick-steel or brick-stone masonry (63%) and cement block (0.04%). The results show that 90% of steel buildings are less than 4 stories tall (Fig. 4.10a). Due to incomplete information on the stories of the remaining buildings, all were grouped into the same class. Our quick street survey showed that the majority of steel-2 and RC buildings are new, but exact information on their time of constructions, quality, etc. is lacking. For future studies, this type of information would be necessary for more detailed analyses.Generally, a structure is damaged when the earthquake force exceeds the structure's resistance. Here, the earthquake force is defined as the seismic force at the ground surface or at the structure's foundation. In other words, specific damage can be estimated when a seismic force at the ground surface, such as the acceleration, MMI, etc., and the structure of the buildings are known. The 5 types of classified building in the city show 6 damage states (Table4.5), similar to EMS98, which was modified by Hassanzadeh et al. [13] for Iranian buildings. These damage states are totally destroyed (D1), very high destruction (D2), high destruction (D3), moderate destruction (D4), light destruction (D5) and no destruction (D6). Building loss can be estimated according to the probability of building loss in terms of the specific damage percentage and damage level. This type of method is applicable to evaluate the stability of individual or critical buildings, but it is not suitable to estimate the damage of a large number of buildings (district two contains over 25000 buildings). Thus, we built a layer in ArcGIS that allows us to filter and analyze several maps based on criteria that we specified. The query will show all the features from the layer we haveselected that meet the criteria. Here, the mentioned query layer contains three criteria: 1- the information of the ground shaking map (MMI) for each specific building, 2- the information of the derived fragility curves for each specific building and 3- the information of classified buildings. Once the relationship between MMI and the damage ratio is established, the building damage can be estimated. For example, the following holds for steel-1 buildings with MMI="IX":

QUERY (1):

"BUILDING_CLASS" >> "A" AND "MMI" >> "IX"=> "MEAN_DAMAGE_RATIO"=0.674

QUERY (2):

"MEAN_DAMAGE_RATIO">>0.674*100 => "DAMAGE_PERCENT"

If 61% <="DAMAGE_PERCENT" >=80 => "Very high destruction" OR "(D2)"

Table 4.5 Description of building damage level adopted by Hassanzadeh et al., 2013[13] and corresponding damage level by EMS 1998 [48].

Destruction level	Damage percent	Descriptions
No destruction (D6)	0-2	Damages are underestimate
Light destruction (D5)	3-10	Very tiny cracks
Moderate destruction (D4)	11-30	5-20 mm cracks are observed in the building
High destruction (D3)	31-60	>20 mm cracks are observed and some components of building such as walls are destroyed
Very high destruction (D2)	61-80	A part of roof and one building's wall is destroyed
Totally destroyed (D1)	81-100	Entire of roof and more than one building's wall destroyed

4.3.3.2 Population vulnerability estimation

Population vulnerability is a key category of vulnerability analysis defined as the degree of population losses from a natural disaster, such as an earthquake. Several methods can be used to estimate the population vulnerability to an earthquake. Generally, they are divided in two categories: the first category considers collateral effects and estimates the casualty numbers (building damages, non-building damages, etc.), and the second category estimates the casualty rate from only the number of damaged buildings. The fatalities due to large-scale earthquakes mostly result from buildings collapses. Earthquake loss studies during the 20th century reveal that 75% of deaths were caused by collapsed buildings in which people were trapped or buried under rubble and waste material [49]. In this study, we followed the second method to estimate the population vulnerability. To estimate the casualties that are a direct result of earthquakes, the population of district two must be identified for the earthquake scenario. Here, we used 2006 census data that were provided by the Management and Planning Organization (Fig. 4.9). The total population in the 10 districts was 1,189,989 people. The statistical result of the seismic network in NW Iran shows that the number of nighttime tremorsis higher than the number of daytime tremors. In this case, the population of each census tract is divided equally into the number of residential units (parcels). We assume that a nighttime earthquake constitutes the worst scenario because the number of dwellers during the day is usually lower and people are outdoors or in public buildings, which are more resistant than the most houses. The number of daytime fatalities cannot be directly determined because the population scatters or flows to different places or directions. Therefore, a linear regression wasdeveloped based on information from past Iranian earthquakes, which includes both daytime and nighttime earthquakes (Table 4.6).This information shows a correlation between the number of daytime and nighttime fatalities (Fig. 4.13a) [49]. Fig. 4.13a presents the correlation of the earthquake intensity from 8-10 MMI. For a moderate earthquake, the percentage of dead people does not significantly differ between daytime and nighttime. On the contrary, higher intensities result in larger difference between the daytime and

nighttime death rates. Like the building vulnerability, the population vulnerability is calculated from the type of information in a query layer. Once building classes and the number of people are identified, the probability of population damage (number of deaths, hospitalized injured and non-hospitalized population) based on questionnaire surveys and reports of previous earthquake is taken into account and summarized in Table 4.7. The human vulnerability function (Eq. 4.7) was then constructed for the types of buildings, number of exposed people and probability of an injury level.
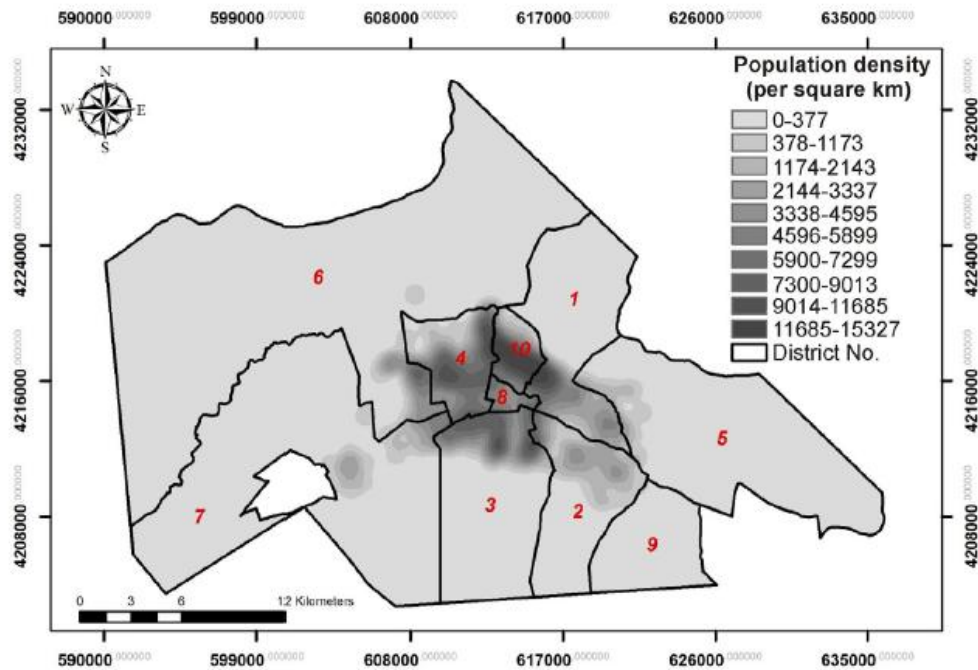
Fig.4.9 Population density of Tabriz city in 2006.

$$H = \sum BP_i \times PK_i \quad (4.7)$$

where H is the population vulnerability, BP_i is the number of people in the buildings in each specific damaged zone and PK_i is the injury probability state (died, hospitalized injured, non-hospitalized and not injured).

Table 4.6 Death ratio by earthquake in Iran. MMI: Modified Mercalli Intensity; Death ratio (%).

Earthquake	Ghir		Tabas		Golbaft		Sirch		Manjil		Ardekul	
Year	1972		1978		1981		1981		1990		1997	
Time	Night-time		Night-time		Day-time		Night-time		Night-time		Day-time	
	MMI	Death	MMI	Death	MMI	Death	MMI	Death	MMI	Death	MMI	Death
Data for each observed site	9	67.1	10	84.3	7	9.2	9	57.1	6	0.79	10	2.7
	9	20.4	9	42.8			9	32.1	6	0.1	10	13.4
			9	19.2			8	9.8	6	0	9	23.1
			8	8.7			8	2.1	9	90	10	45.5
							7	0.08	10	90	8	6.5
							7	0.8	7	9	8	11
									10	66.7	8	1.7
									8	13.3	7	5.8
											8	3

4.4 Results

The applied model outputs the damaged area, a 3D scene of demolished buildings, rate of daytime and nighttime casualties and the number of required resources. These results allow decision-makers to plan safer shelters or settlement areas for survivors. Overall, the area of district two is approximately 42.92 km^2 and includes parks, streets, alleys and vacant lands, while the pure residential area is 6.8 km^2, of which 3.1 km^2 is totally destroyed as a result of the simulated earthquake. In detail, the total base area at all damage states (D1, D2, D3 and D4) for steel-1, RC, steel-2, brick-steel and brick-stone are 1.829, 1.003, 0.101, 2.711 and 0.002 km^2, respectively. The results based on the GIS-oriented analysis indicate that 69.5% of the buildings are totally destroyed, 18.2% experience very high destruction, 12.25% experience high destruction and 0.05% experience moderate destruction (Fig. 4.10b).
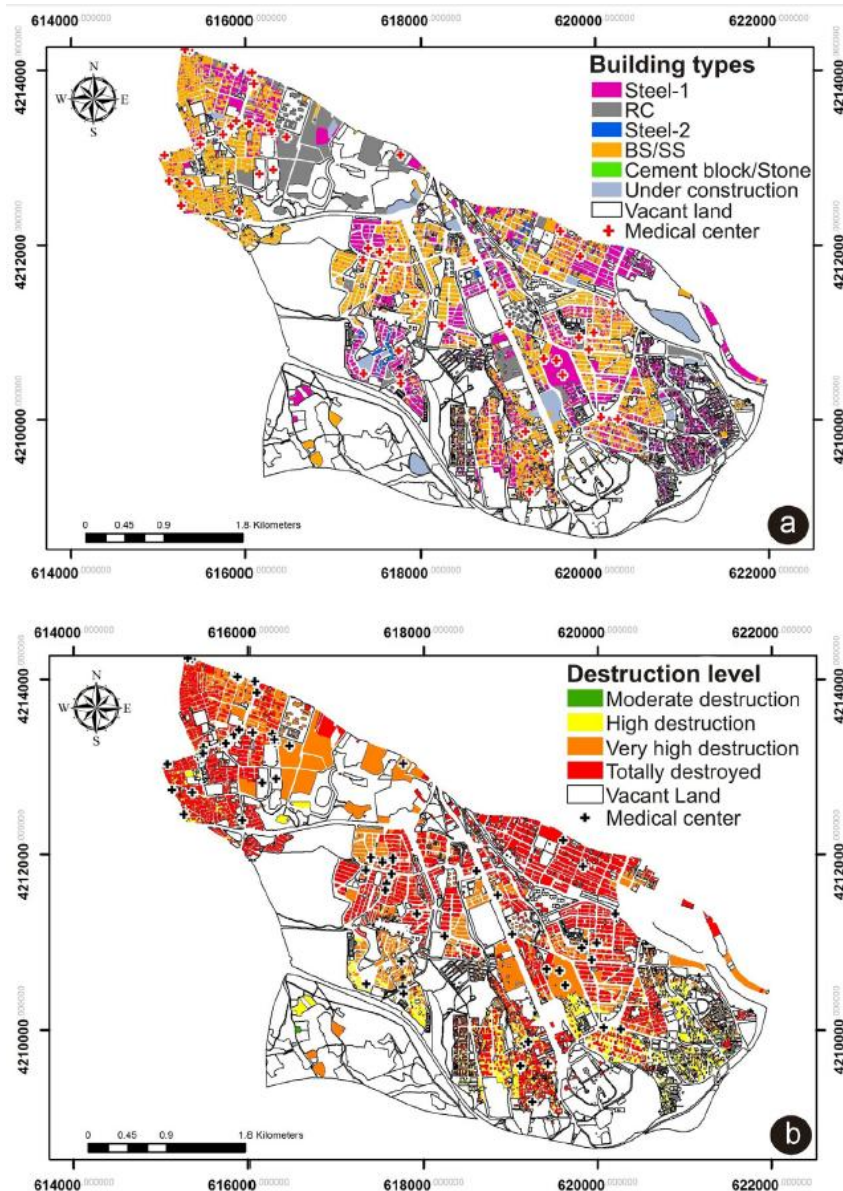
Fig.4.10(a) Building types in district two; **(b)**Destruction map.

At intensity IX, 54% of damaged buildings are placed in D1, and 98% of these buildings are brick-steel or brick-stone masonry buildings, while 2% are steel-1 and cement block buildings. Eighteen percent of the buildings are damaged at D2, 84.7% of which are steel-1, 12.2% are RC, 3% are steel-2 and 0.1% are brick-steel or brick-stone buildings. Twelve percent of all damaged buildings are placed in D3, of which 87% are steel-1, 10% are RC and 3% are steel-2 buildings. Thus, 82% of damaged buildings are placed at intensity IX. The remaining buildings are almost all placed at intensity X. Due to the low possibility of resisting a seismic force at intensity X, the buildings are placed at D1. Thirty-eight percent are steel-1, 4% are RC, 1% are steel-2 and 57% are brick masonry buildings. The resulting estimates for each damage level are summarized in

Table 4.8 and Table 4.9. In district two, the mean total damages of the base area at D1, D2 and D3 at intensity IX are 2.2529, 1.9081 and 0.6173 km^2, respectively. If we take their stories into account, the mean total damages of the floor area at D1, D2 and D3 are 2.889, 4.8368 and 1.3053 km^2, respectively. Due to the fewer buildings at intensity X, the total damaged area is considerably lower than those placed at intensity IX. The mean total damage of the base area at D1 is 0.8517 km^2, and the mean total damage of the floor area is 1.3756 km^2 (Table 4.10, Table 4.11 and Fig. 4.11). At either intensity IX and X, the most damaged area belongs to D1, which shows that the highest number of buildings is completely demolished. Furthermore, brick masonry buildings show a high damage potential. These buildings are abundant in the cities and villages in NW Iran, and reinforced concrete structures demonstrated the most acceptable performance, as expected. This effect might be due to high integrity of structural elements in reinforced concrete structures, such as foundations, columns, beams and slabs, compared to the other types of structures [46].

Table 4.7 Classification of expected population damage based on questionnaire surveys and reports of previous earthquakes in Iran [50].

Type of destruction	Status of people	Damage %
No destruction	Dead	0
	Hospitalized	0
	Non-hospitalized	1
	Not injured	99
Light destruction	Dead	2
	Hospitalized	5
	Non-hospitalized	9
	Not injured	84
Moderate destruction	Dead	4
	Hospitalized	9
	Non-hospitalized	15
	Not injured	72
High destruction	Dead	13
	Hospitalized	17
	Non-hospitalized	23
	Not injured	47
Very high destruction	Dead	16
	Hospitalized	22
	Non-hospitalized	28
	Not injured	34
Totally destroyed	Dead	41
	Hospitalized	16
	Non-hospitalized	21
	Not injured	22

Table4.8 Number of damaged buildings in terms of destruction level at intensity IX.

	D1	D2	D3	D4	Total number of damaged building types
Steel-1	1	3882	2662	1	6546
Reinforced Concrete	0	548	312	0	860
Steel-2	0	149	88	0	237
Brick-steel or Stone steel	13687	4	0	0	13691
Cement block and stone	9	0	0	1	9
Total at each level	13697	4583	3062	2	21343

Table4.9 Number of damaged buildings in terms of destruction level at intensity X.

	D1	D2	D3	D4	Total number of damaged building types
Steel-1	1420	0	0	0	1420
Reinforced Concrete	142	0	0	0	142
Steel-2	60	0	0	0	60
Brick-steel or Stone steel	2180	0	0	0	2180
Cement block and stone	1	0	0	0	1
Total at each level	3803	0	0	0	3803

Table4.10 Expected amount of area of damaged buildings in terms of destruction level at intensity IX.

	D1		D2		D3		D4	
	B area (km^2)	F area (km^2)	B area (km^2)	F area (km^2)	B area (km^2)	F area (km^2)	B area (km^2)	F area (km^2)
Steel-1	0.0002	0.0004	1.0178	1.7681	0.4875	0.833	0	0
Reinforced concrete	0	0	0.7891	2.7433	0.11	0.3894	0	0
Steel-2	0	0	0.0623	0.2865	0.0198	0.0829	0	0
Brick-steel or Stone steel	2.252	2.884	0.0389	0.0389	0	0	0	0
Cement block and stone	0.0007	0.0046	0	0	0	0	0	0
Total	2.2529	2.889	1.9081	4.8368	0.6173	1.3053	0	0

Table4.11 Expected amount of area of damaged buildings in terms of destruction level at intensity X.

	D1		D2		D3		D4	
	B area (km^2)	F area (km^2)	B area (km^2)	F area (km^2)	B area (km^2)	F area (km^2)	B area (km^2)	F area (km^2)
Steel-1	0.324	0.5149	0	0	0	0	0	0
Reinforced concrete	0.104	0.3517	0	0	0	0	0	0
Steel-2	0.0019	0.008	0	0	0	0	0	0
Brick-steel or Stone steel	0.42	0.4942	0	0	0	0	0	0
Cement block and stone	0.0018	0.0018	0	0	0	0	0	0
Total	0.8517	1.3706	0	0	0	0	0	0

Table 4.12 Population vulnerability after an M 7 earthquake.

Destruction level	Exposed population	Vulnerable population	Loss level
Totally destroyed (D1)	58167	23848 (n)	Dead
		5962 (d)	
		9307 (n)	Hospitalized injured
		4374 (d)	
		12215 (n)	Non-hospitalized
		8184 (d)	
		12797 (n)	Not injured
		39647 (d)	
Very high destruction (D2)	15233	2437 (n)	Dead
		609 (d)	
		3351 (n)	Hospitalized injured
		1575 (d)	
		4265 (n)	Non-hospitalized
		2858 (d)	
		5180 (n)	Not injured
		10191 (d)	
High destruction (D3)	10178	1323 (n)	Dead
		331 (d)	
		1730 (n)	Hospitalized injured
		813 (d)	
		2341 (n)	Non-hospitalized
		1568 (d)	
		4784 (n)	Not injured
		7470 (d)	
Moderate destruction (D4)	7	0 (n)	Dead
		0 (d)	
		1 (n)	Hospitalized injured
		0 (d)	
		1 (n)	Non-hospitalized
		0 (d)	
		5 (n)	Not injured
		7 (d)	

The three-dimensional perspective of buildings before and after the earthquake scenario in district two are shown in Fig. 4.12. As illustrated, the most vulnerable structures are located in the North and West parts of district two, and the majority structures resistant to the earthquake vibrations are located in the new towns (i.e., Yaghchian) of the eastern boundary. Infirmaries, which are an important place after any disaster, are seriously damaged (Fig. 4.10 a, b) due to their poor construction. Forty-one percent of infirmaries are completely collapsed and cannot withstand post-disaster incidents.
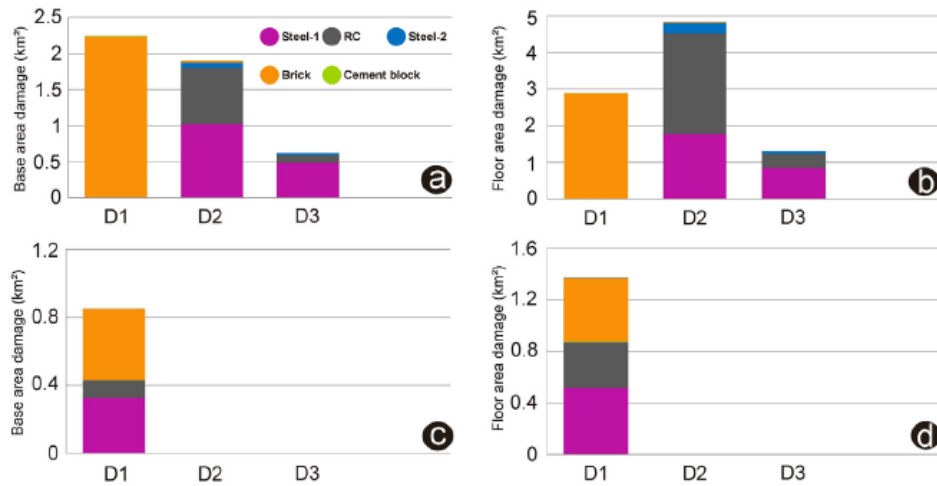
Fig.4.11 Building vulnerability distribution in terms of base area and floor area. **(a)** and **(b)** at intensity IX; **(c)** and **(d)** at intensity X.
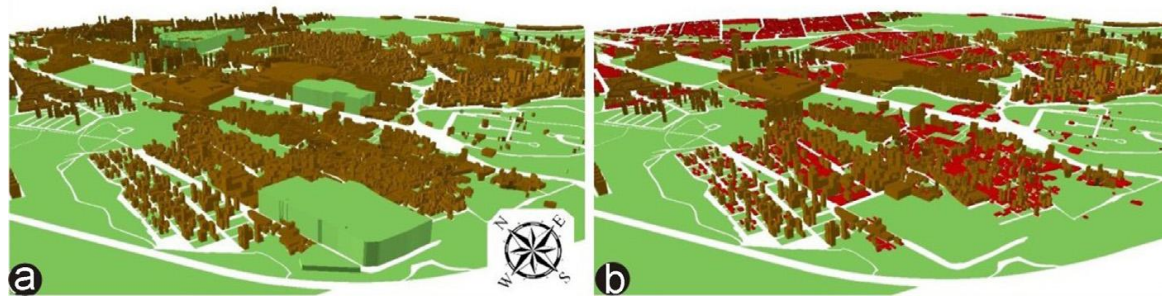
Fig.4.12 Three-dimensional view of the study area. **(a)** before earthquake; **(b)** after earthquake.

The population vulnerability report was estimated using the population dataset, building vulnerability results and population vulnerability ratios (Table 4.6) in different classes (Table 4.7) [50]. For nighttime events, 33% of the entire population in district two died, while 86% of dead people are placed at D1, 9% at D2 and 5% at D3 levels. Sixty-four percent of hospitalized people are placed at D1, 24% at D2 and 12% at D3. The percentages of non-hospitalized injured people at the D1, D2 and D3 states are 64%, 13% and 11%, respectively. The number of dead, hospitalized and non-hospitalized injured people significantly decreased for the same event during the daytime. For example, the total number of dead people decreased to 11% (see Table 4.12 and Fig. 4.13 for more details).
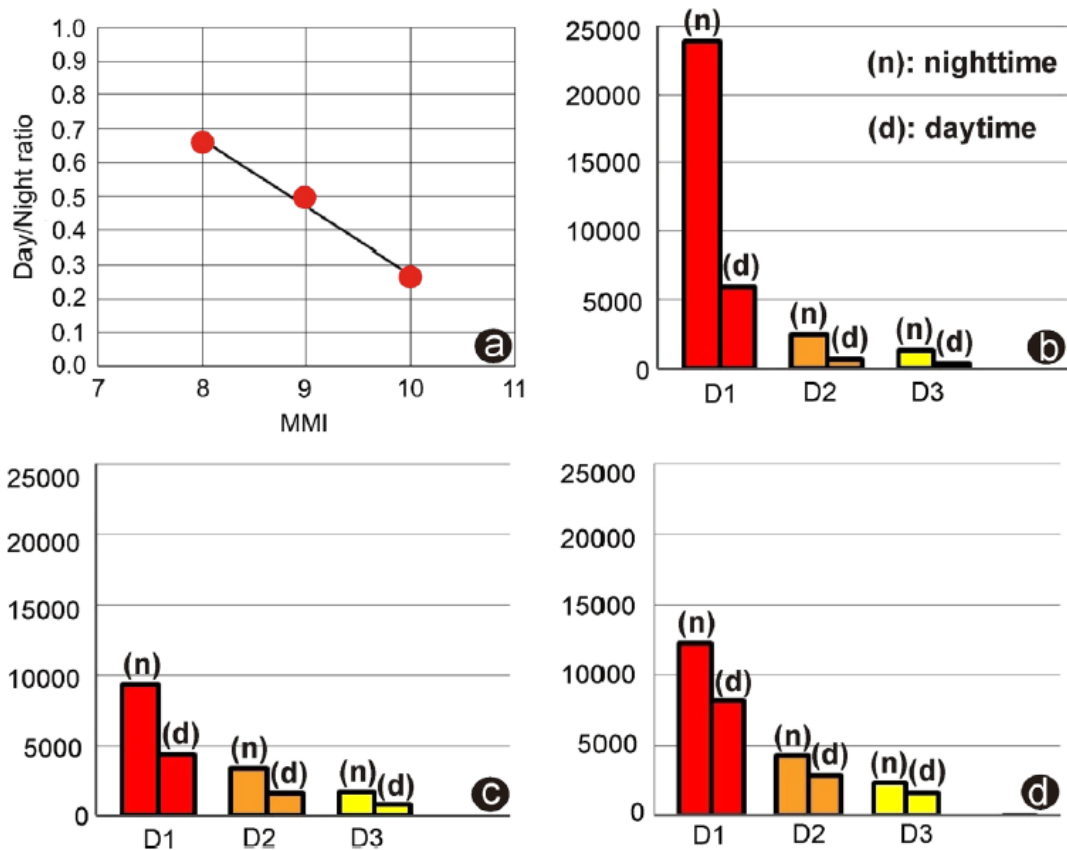
Fig.4.13 (a) day/night ratio for number of casualties.**(b)** Number of dead people for each damage state. **(c)** Number of hospitalized people for each damage state. **(d)** Number of injured people for each damage state.

D1: Totally destroyed; D2: Very high destruction; D3: High destruction.

The high level of destruction and human loss primarily results from the assumption of a strong near field scenario due to an elapsed time of 233 and 292 years since the two last major earthquakes (1721 and 1780) on the North Tabriz Fault, which is situated in the immediate vicinity of Tabriz city. Moreover, historical documents indicate that the high rate of vulnerability is reasonable because the city was completely destroyed several times and thousands were killed [22]. Our street survey, which included experts, shows that poor construction methods are one of the important challenges.

Survival inside trapped places is usually only possible for approximately 2 days after an earthquake. Therefore, the number of rescuers or temporary infirmaries is a crucial factor in the immediate aftermath of an earthquake. The basic demands after an earthquake scenario were calculated based on the number of damaged buildings and population (Table4.13) [50] and are reported in Table 4.14.

Table 4.13 Formulation of required resources based on Sphere 2004 [50] and Bam earthquake report estimation [48].

Material	Formulation
Total Damaged Population (TDP)	Total population - Dead people
Rescuer	(Hospitalized injuries + Injured non-hospitalized)/10
Shovel	Rescuer + Not injured people
Emergency toilet	TDP/20
Emergency bath	TDP/20
Stick and splint	(Hospitalized injuries + Injured non-hospitalized) * 10
Bandage	(Hospitalized injuries + Injured non-hospitalized) * 10
Field infirmary	Hospitalized injuries/100
Drinking water bottle (/day)	TDP * 3
Canned food (/day)	TDP * 4
Bread pieces (/day)	TDP * 2
Blanket	TDP * 1

Table 4.14 Estimated resources based on KDMC 2008 and Hassanzadeh et al. [13,50,51].

Material	The number of resources
Rescuer	5,598
Shovel	28,364
Emergency toilet	2,799
Emergency bath	2,799
Stick and splint	332,110
Bandage	332,110
Field infirmary	144
Drinking water bottle (/day)	167,931
Canned food (/day)	223,908
Bread pieces (/day)	111,954
Blanket	55,977

4.5 Model validation using Ahar earthquake data and observations

The accuracy of the presented model based on an actual earthquake remains a question. The level of available seismic information for the Ahar region is relatively similar to that of the Tabriz region. In addition, we performed a site investigation focused on buildings, lifelines and bridge damage inside affected cities and villages to identify the building vulnerability [52]. The shallow twin earthquakes (M 6.5 and M 6.3) of the Ahar were considered to validate the model. These earthquakes occurred in the highly populated region of East Azerbaijan, near the cities of Ahar, Varzeghan and Heris on August 11, 2012 at 16:50 Iran local time [52]. The first event was

relatively similar to that of the aforementioned Tabriz scenario. A regular spatial dataset for the Ahar or Varzeghan cities for a damage assessment analysis was lacking; Chopanlar village was selected as a validation target site (Fig. 4.14 and Fig. 4.15a). Field observations and surveys demonstrate that the epicenter of events is located in a rural area 60 km away from Tabriz. At least 500 villages were seriously damaged. Most parts of the villages were constructed from mud and cement blocks without any technical supervision (Fig. 4.15a). Public buildings that consist of tie columns and beams with brick walls performed well in response to seismic vibrations. Although repairable, these buildings were damaged due to the heavy roof and wall materials [52,53].

Fig.4.14 Field observation of Chopanlar showing the collapsed buildings.

Most deaths were reported 8 to 20 hours after the earthquake. To assess the accuracy of the presented model in Chopanlar, an interrelation analysis between real data (or observations) and the model was applied. The accelerometer data from 74 seismic stations, which are provided by Building and Housing Research Center (BHRC) with a 200 km radius, were used to estimate the real intensity map and compared with the modeled intensity map (Fig. 4.16a) [54]. The mean isoseismal radii of the model for zones V, VI, VII, VIII and IX are 7.4, 14.6, 26.5 and 45 km, respectively. The coefficient of determination for the presented model shows an accuracy of 76% for near-sites. It decreases to a minimum of 70% for locations far from the epicenter, which shows that the model underestimates distant sites with anintensity greater than 5 (Fig. 4.16b). The physical damage to buildings in Chopanlar was compared with the model and indicates that the

result is 80% accurate (Fig 4.15b, c). However, more accurate methods are needed (i.e., a remotely sense approach) to assess the degree of damage to buildings at smaller scales (i.e., in Ahar or Varzeghan cities, where the building types are more diverse).
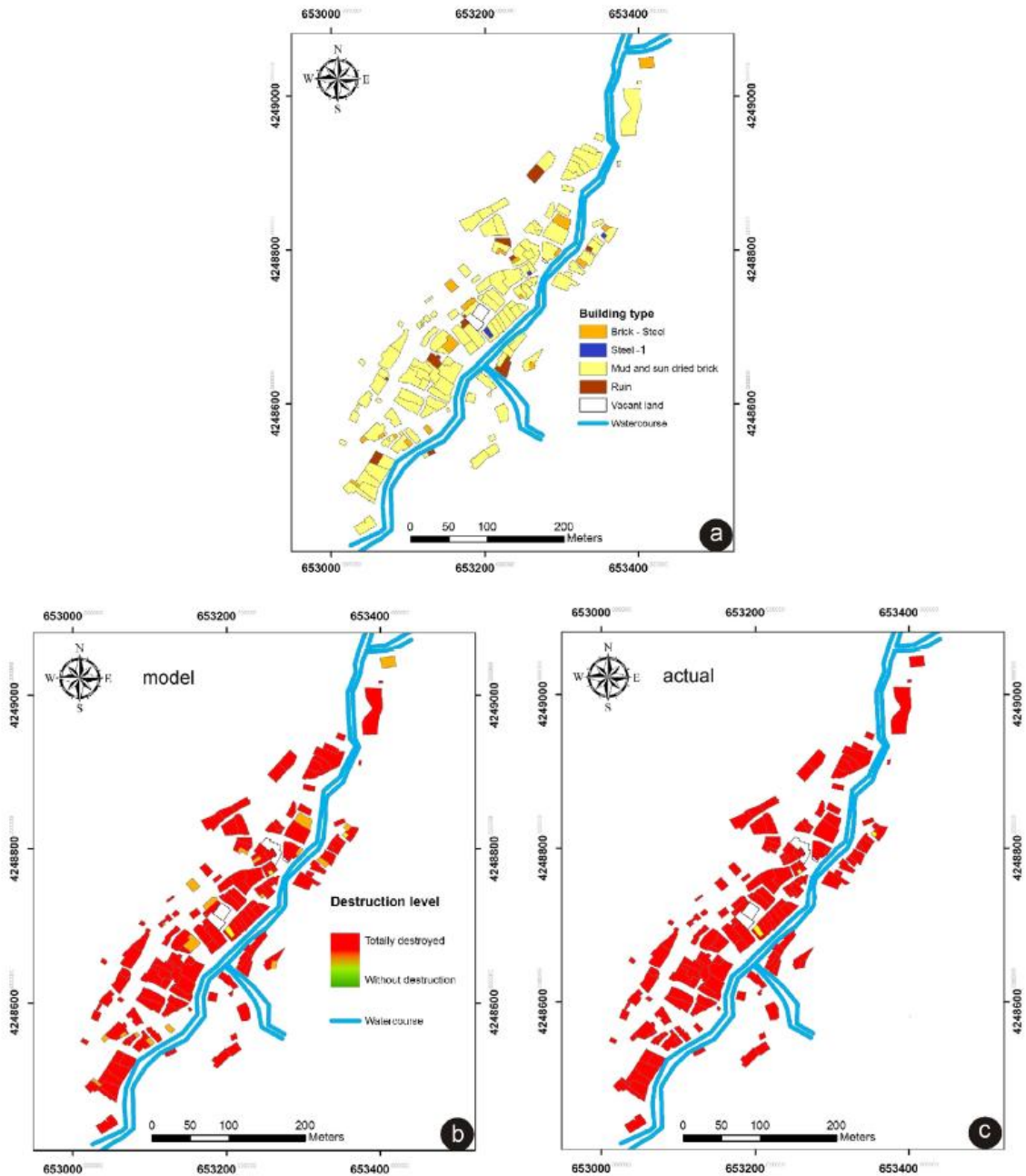
Fig.4.15(a) Buildings types of Chopanlar. **(b)** Modeled destruction map of Chopanlar; **(c)** Actual destruction map of Chopanlar.
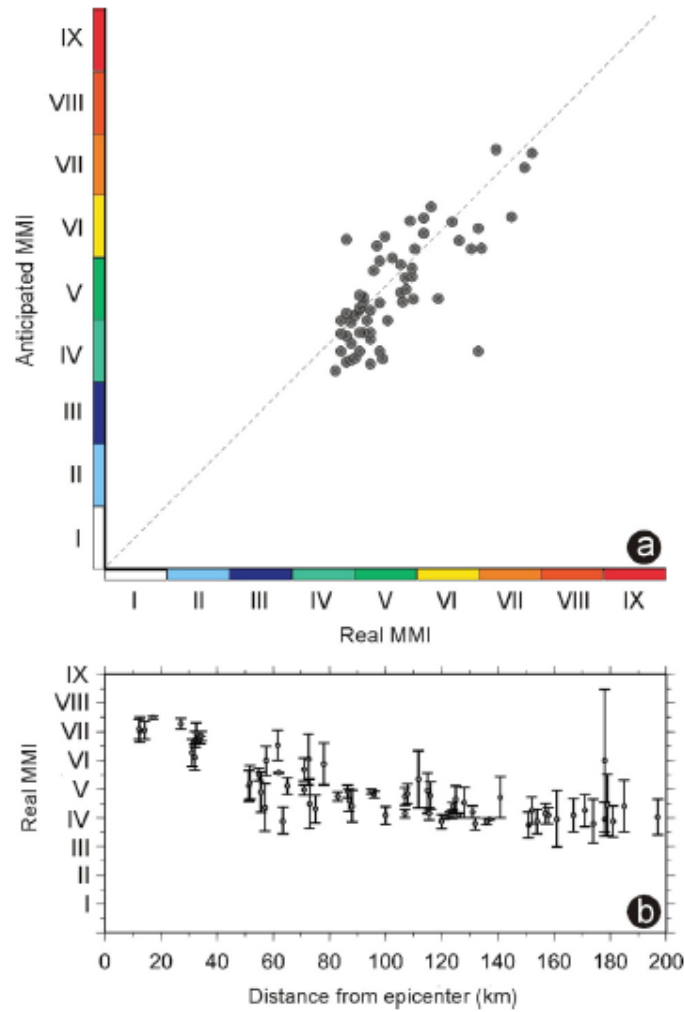
Fig.4.16(a) Comparison of real intensity (deduced from accelerographs) and anticipated intensity (estimated from local site effects and attenuation relationships) in 74 seismic stations; **(b)** Real intensity variation of 74 seismic stations. Error bars represent $\Delta MMI=|MMI_{real}-MMI_{anticipated}|$.

4.6 Summary and conclusion

Overall this study suggests that the seismic hazard potential in district two is almost high according to the seismic and vulnerability steps. This paper demonstrates GIS-oriented procedures in seismic and vulnerability steps in addition to the following results:

A ground-shaking map was created for the Tabriz region based on a series of influential parameters and relative intensity relationships. The parameters were discrete points, i.e., they could not be applied to the seismic step. Thus, they were converted into shape files, classified and finally integrated in a relational geodatabase. The level of certainty of the parameters was validated using the powerful Kriging interpolation method, which links all data together at the same matrix dimensions. A GSM map was produced via the pixel-dependence overlaying of

effective parameters. The delineation of seismic hazard zones requires that effective parameters be established in AHP processes that are clearly defined by their impacts on the seismic microzonation, urban planning and/or land management. For example, the feasibility of the geoid slope map was applied as an effective parameter to define the Iranian plateau. A seismic hazard zonation map was then used to determine the potential building damage in district two of Tabriz city, which exhibits a high seismic hazard such as other densely populated districts, such as districts four, eight and ten. The building vulnerability estimation benefits from a query layer in ArcGIS that considers three criteria: 1- the information of the ground shaking map (MMI) for each specific building, 2- the information from the derived fragility curves for each specific building and 3- the information of classified buildings. The most damaged area was D1 at both intensities IX and X, which shows that the highest number of building was completely demolished. During the last century, Tabriz city has grown across the hazardous area. Widespread damage and casualties due to earthquakes in 1721 (30000 people killed) and in 1780 (50000 people killed) in Tabriz city did not profoundly affect the urban revisions. This study demonstrated that brick-steel masonry buildings are most vulnerable (78% total damaged builds are masonry) in district two, most likely due to the disintegration of the mortar and bricks. Some old unreinforced masonry buildings in district two may even collapse as a consequence of a moderate near field earthquake. Additional data, like the age, material, quality of the buildings and lifeline systems (water and gas pipelines, public transportation), will enhance the scale of damage for this region. Currently, attention should be focused on poor building construction, especially low quality materials, which do not comply with building standard codes for earthquake-resistant design, and the lack of proper supervision during the construction operations of private buildings. Thirty-three percent of the entire population in district two died during the nighttime scenario, while 86% of dead people are placed at the D1, 9% at D2 and 5% at D3 levels. Sixty-four percent of hospitalized people are placed at D1, 24% at D2 and 12% at D3. The number of dead people decreases to 11% for a daytime event. After the scenario, over 30000 homeless require temporary shelters, such as tents, or other basic demands, such as blankets, bottled drinking water, canned food, and bread. The validation of the model using Ahar earthquake (2012) indicated that the model underestimates distant sites with an intensity scale greater than 5 MMI. This study demonstrated that small manipulations in the weights of parameters or fault characteristics (i.e., fault length, epicenter location) could clearly affect the output maps. The mentioned information of the validation model does not support higher intensities. In addition, we could not estimate the accuracy of the population vulnerability due to insufficient information for inhabited areas in the Ahar region. However, "the procedure" of the presented model could satisfy the validation of the building damage aspect irrespective of the intensity grade. In other words, the provided validation model and building damage percentage do

not directly correlate in Tabriz. This finding shows that accuracy of the procedure between the actual surveyed damage and model in Chopanlar (Fig. 4.15b, c).

References

[1] Prompt Assessment of Global Earthquakes for Response (PAGER). <http:// earthquake.usgs.gov/eqcenter/pager/S >; 2010.

[2] Porter KA, Jaiswal K, Wald D.J, Hearne M. Developing loss models for the US Geological Survey's Prompt Assessment of Global Earthquakes for Response (PAGER) system. Proceedings of 14 WCEE, Beijing, China 2008.

[3] Erdik M, Şeşetyan K, Demircioğlu M.B, Hancılar U, Zülfikar C. Rapid earthquake loss assessment after damaging earthquakes. Soil Dynamics and Earthquake Engineering 2011; 31: 247–266.

[4] FEMA, 2003a.HAZUSMH MR4 Earthquake Model User Manual. Department of Homeland Security.Federal Emergency Management Agency.MitigationDivision.Washington, D.C. 2012; www.fema.gov/library/viewRecord.do?id=3732.

[5] FEMA, 2003b.HAZUSMH MR4 Earthquake Model Technical Manual. Department of Homeland Security.Federal Emergency Management Agency.Mitigation Division.Washington, D.C. 2012; www.fema.gov/library/viewRecord.do?id=3732.

[6] Yuba County, Multi-Jurisdictional Multi-Hazard Mitigation Plan.http://www.co.yuba.ca.us.

[7] FEMA, Harris County, Texas Uses HAZUS-Multi Hazard for Risk Assessment & Hurricane Preparedness.2005;http://www.fema.gov/hazus/harris-county-texas-uses-hazus-multi-hazard-risk-assessment-hurricane-preparedness.

[8] Cinicioglu S.F, Bozbey I, Oztoprak S, Kelesoglu M.K. An integrated earthquake damage assessment methodology and its application for two districts in Istanbul, Turkey. Engineering Geology 2007; 94: 145–165.

[9] Ansal A, Kurtulus A, Tonuk G. Seismic microzonation and earthquake damage scenarios for urban areas. Soil Dynamics and Earthquake Engineering 2010; 30: 1319–1328.

[10] Armaş I. Multi-criteria vulnerability analysis to earthquake hazard of Bucharest, Romania. Natural Hazards 2012; 63: 1129–1156.

[11] W. Cole S, Xu Y, W. Burton P. Seismic hazard and risk in Shanghai and estimationof expected building damage. Soil Dynamics and Earthquake Engineering 2008; 28: 778–794.

[12] Hashemi M, Alesheikh A.A. A GIS-based earthquake damage assessment and settlement methodology. Soil Dynamics and Earthquake Engineering 2011; 31: 1607–1617.

[13] Hassanzadeh R, Zorica N, AlaviRazavi A, Norouzzadeh M, Hodhodkian H.Interactive approach for GIS-based earthquake scenario development and resource estimation (Karmania hazard model). Computers & Geoscience 2013; 51: 324–338.

[14] Kamel B. Crisis management of earthquake in pre-occurrence stage by using of GIS. Case study: Municipality of Tabriz region 1. University of Tabriz, Faculty of Geography.Master of Science thesis 2012.

[15] Jackson J. Partitioning of strike-slip and convergent motion between Eurasia and Arabia in Eastern Turkey and the Caucasus.Journal of Geophysical Research 1992; 97 (B9), 12471–12479.

[16] McClusky et al. (2000), GPS constraints on plate kinematics and dynamics in the eastern Mediterranean and Caucasus, Journal of Geophysical Research, 105: 5695–5719.

[17] Westaway R. Block rotation in western Turkey 1. Observational evidence.Journal of Geophysical Research 1990; 95 (B12): 19857–19884.

[18] McKenzie D.P, Active tectonics of the Mediterranean region. Geophysical Journal of Royal Astronomical Society 1972; 30: 109–185.

[19] Toksöz M.N, Arpat E, Saroglu, F. East Anatolia earthquake of 24 November, 1976 Nature 1977; 270: 423–425.

[20] Jackson J, McKenzie D. P. The relationship between plate motions and seismic moment tensors, and the rates of active deformation in the Mediterranean and the Middle East. Geophysical Journal International 1988; 93: 45–73.

[21] Hessami Kh., Jamali F, Tabassi H. Major active faults of Iran: Tehran, Iran, International Institute of Earthquake Engineering and Seismology 2003; 1 sheet, scale 1:2,500,000.

[22] Berberian M. Natural hazards and the first earthquake catalogue of Iran. International Institute of Earthquake Engineering and Seismology 1994; 1: 266–270.

[23] Karimzadeh S, Cakir Z, Osmanoğlu B, Schmalzle G, Miyajima M, Amiraslanzadeh R, Djamour Y. Interseismic strain accumulation across the North Tabriz Fault (NW Iran) deduced from InSAR time series. Journal of Geodynamics 2013; 66: 53–58.

[24] Dehghani G.A, and Makris J. The gravity field and crustal structure of Iran.Geological Survey of Iran 1983; 51: 51–68.

[25] Tehran Padir Consulting Co. Tabriz seismic microzoation investigations 2006.

[26] Nowroozi A.A. Empirical relations between magnitude and fault parameters for earthquakes in Iran.Bulletin of the Seismological Society of America 1985. 75: 1327–1338.

[27] Wells D.L, Coppersmith K.J. New empirical relationships among magnitude, rupture length, rupture width, rupture area, and surface displacement. Bulletin of the Seismological Society of America 1994; 84: 974–1002.

[28] Mohajer A, Nowroozi A.A. Observed and probable Intensity Zoning of Iran. Tectonophysics 1987; 49:21–30.

[29] Bonilla M.G, Mark R.K, Lienkaemper J.J. Statistical relations among earthquake magnitude, surface rupture length, and surface fault displacement. Seismological Society of America Bulletin 1984; 74: 2379–2411.

[30] Pazhouhesh Omran Rahvar Engineering Consultants. Interim report of geotechnical investigations of Tabriz Urban Railway project 2008.

[31] Assadian O, Eftekharnejad J, Jalilian M, Afsharianzadeh A.M. Geology map of Tabriz region. Geological Survey of Iran. 1 sheet, scale 1:100,000.

[32] Barthelmes F. Definition of Functionals of the Geopotential and Their Calculation from Spherical Harmonic Models 2013; http://icgem.gfz-potsdam.de/ICGEM.

[33] Kiamehr R, Sjöberg L.E. Impact of a precise geoid model in studying tectonic structures—A case study in Iran. Journal of Geodynamics 2006; 42: 1–11.

[34] Fallahi A, Erami M.H, Mashayekhi h.R, Miyajima M. Microtremor and Shear Wave Velocity Measurements in Tabriz to Use in Seismic Microzonation. 6th International Conference of Seismology and Earthquake Engineering 2011.

[35] Abdolahi M.R, Jamali F, Pedrami M, Haddadan M, Ghaemi J, Ghomashi A. Engineering geological maps of Tabriz. Engineering (compressive strength, suspectibility to slide, discontinuity surface).Geological Survey of Iran. 1 sheet, scale 1:50,000.

[36] Iranian code of practice for seismic resistance design of buildings. Iranian Building Codes and Standards, Standard No. 2800.3[rd] edition.Building and Housing Research Center (BHRC) 1999.

[37] Child C. Interpolating surfaces in ArcGIS spatial analyst; 2004. Arc User, 32–35.

[38] Wang Z. Seismic Hazard Assessment: Issues and Alternatives. Pure Applied Geophysics 2010.

[39] Mualchin L, Jones A.L. Peak Acceleration from Maximum Credible Earthquakes in California. California Department Conservation 1992; Open-File Rep. 92-01: 53 pp & Map.

[40] Mualchin L. Development of the Caltrans deterministic fault and earthquake hazard map of California. Engineering Geology 1996; 42: 217–222.

[41] Mualchin L, History of Modern Earthquake Hazard Mapping and Assessment in California Using a Deterministic or Scenario Approach. Pure Applied Geophysics 2011; 168: 383–407.

[42] Hamzeloo H, Mahood M. Ground-Motion Attenuation Relationship for East Central Iran. Bulletin of the Seismological Society of America 2012; 102: 2677–2684.

[43] Saffari H, Kuwata Y, Takada S, Mahdavian A.Updated PGA, PGV, and Spectral Acceleration Attenuation Relations for Iran. Earthquake Spectra 2012; 28: 257–276.

[44] Chandra V, Mc Whorter J.G, Nowroozi A.A. Attenuation of Intensities in Iran. Bulletin of the Seismological Society of America 1979; 69: 237–250.

[45] Siahkali Moradi A, Mirzaei N, Rezapour M. Attenuation relationships of seismic intensity in Iran. Journal of Earth and Space Physics 2004; 30: 1–9.

[46] The Study on Seismic Microzoning of the Greater Tehran Area in the Islamic Republic of Iran. Final Report. Japan International Cooperation Agency (JICA) and Centre for Earthquake and Environmental Studies of Tehran (CEST) and Tehran Municipality 2000.

[47] ATC-13 Earthquake Damage Evaluation Data for California. Applied Technology Council. Redwood city, CA 1985.

[48] Grünthal G. European Macroseismic Scale 1998(EMS-98). Cahiers du Centre Europeen de Geodynamique et de Seismologie, Vol. 15. Centre Europeen de Geodynamique et de Seismologie, Luxembourg; 1998. p.99.

[49] Coburn A, Spence R. Earthquake Protection. 2nd edition. West Sussex, England: John Wiley and Sons Ltd; 2002.

[50] Karmania Hazard Model User Manual. Kerman Disaster Management Center (KDMC). Kerman, Iran 2008; p. 235.

[51] Humanitarian Charter and Minimum Standards in Humanitarian Response (Sphere), Northampton, United Kingdom, The Sphere Project, Belmont Press Ltd; 2004.

[52] Miyajima M, Fallahi A, Sadeghi A, Ghanbari E, Soltani H, Amiraslanzadeh R, Vakilazadsarabi A, Forounzandeh F, Sheikhalizadeh R. Site Investigation of the Ahar-Varzeghan Earthquake in NW Iran of Auguest 11, 2012. Japan Society of Civil Engineers (JSCE) 2013.

[53] Zare M, Kalantari A, Ansari A, Haghshenas E, Davoudi M, Mostafazadeh M. Reconnaissance report of Varzeghan twin earthquakes (Ahar county - Eastern Azerbaijan) of International Institute of Earthquake Engineering and Seismology (IIEES) 2012 (In Persian).

[54] Iran Strong Motion Network. Building and Housing Research Center.

5. Concluding remarks

5.1. Conclusion

In this study the feasibility of GIS and remote sensing applications are shown and studied. The importance of these tools could be boosted when they are combined to study a specific region or phenomenon. The outcomes of chapter 2 showed that classification of seismic stations could be profitably used in description of the location of the seismic stations. Generating TPI maps using accurate DEMs with different radii is one of the useful/fast approaches for landscape characterization and slope position classification. TPI results for Iran territory showed that the majority of the seismic stations in the larger radius (TPI 100m) are located in the Valley and Ridge positions while in the smaller one (TPI 50), the stations are categorized in different slope positions. One important point was the size of radius which is discussed fairly in the chapter 2. The TPI results are the first topographic classification of the study area that shows that the valley and ridge classes were the largest categories in Iran territory for both 50m and 100m radii. Although these classes were detected well in the Alborz & Azerbaijan, Central Iran and Zagros blocks, but lower slope and flat positions were not detected well in the Lut and Central Iran which shows the TPI analysis has some shortcomings for detection of more complex textures. To solve this problem, the desirable TPI analysis ranges between 50m and 1000m with a certain interval, but in this study due to limitations in the memory and the used code, only radii 50m and 100m were tested. By increasing the radius, the number of ridge stations are increased which means that the TPI is entirely a scale-dependent approach. In seismic stations, larger radii can be used in application of topographic amplification factor, while small scales are important in detection of morphology of the study area. Simply put, the resolution of the topography (30m) in small-scale analysis (e.g. TPI 50m) leads to a detailed site condition map in which topographic features are likely to be manifestations of real and model differences. By increasing the TPI neighborhood size, topographic amplification factor can be studied well while the small lateral features disappear or in other words, there is a tradeoff between topographic amplification factor and rest of the site factors in different neighborhood sizes. TPI 100m provides detailed results about the landscape formations which can be used to describe site-condition and probably good results for seismological purposes related with TAF.

In chapter 3, tectonic and non-tectonic hazards in NW Iran are studied. Land subsidence patterns in the Tabriz basin are observed through InSAR method. The results of the InSAR analysis show that the maximum land subsidence is occurred in the well 30 (~40 mm) at the center of the subsidence pattern which was growing between 2004 and 2009. The water level measurements and InSAR results are plotted in order to show the relationship between land subsidence, seasonal recharge and amount of water removal, but lack of enough geodetic observations (i.e. GPS or

even precise leveling) in the study area restricts extensive interpretation of large-scale deformations. Only one thing, the subsidence rate was accelerated in W15, W26 and W30 (sub-basin 1) between 2007 and 2009 according to InSAR time series and as a consequences considerable damages to the structures located in the Tabriz basin. With respect to the country's climate, seasonal water fluctuations (water recharge and discharge) are relatively correlated with seasonal climate condition of the above-mentioned wells (W15, W26 and W30). The subsidence results are not contributed in the hazard model of NW Iran. However, the results could be a ''call for action'' to develop new geodetic stations in the Tabriz basin and design new water resource models before the region falls victim of intensive agricultural activities and anthropogenic changes like Mashhad valley in NE Iran. Following in the chapter 3 interseismic slip rate of the North Tabriz Fault (NTF) has been studied as well. A multi temporal InSAR technique is used to deduce the slip of the North Tabriz Fault using 17 ENVISAT ASAR images acquired during a period of 6 years between 2004 and 2010. Elastic dislocation modeling of the InSAR data yields an average slip rate of 8.7 ± 2.5 mm/yr, in agreement with previous geodetic estimates based on recent GPS measurements which mean that earthquake recurrence intervals for large earthquake (Mw 7 to 7.3) on the NTF could be about 250-300 years.

Based on the initial seismic hazard assessment in chapter 3, the earthquake scenario for the city of Tabriz is defined on the NTF under a GIS procedure. The procedure is followed in two main steps (seismic microzonation and vulnerability steps) along with its application in Tabriz (a city in NW Iran). First, the detailed geological, geodetical, geotechnical and geophysical parameters of the region are combined using an Analytic Hierarchy Process (AHP) and a deterministic near-field earthquake of magnitude 7 in the North Tabriz Fault is simulated. This simulation provides differing intensities of ground shaking in the different districts of Tabriz. Second, the vulnerability of buildings, human losses and basic resources for survivors are estimated in district two of the city based on damage functions and relational analyses. The results demonstrate that 69.5% of existing buildings are completely destroyed, and the rate of fatalities is approximately 33% after a nighttime scenario. Finally, the same procedure was applied to an actual earthquake (first event on the 11th of August, 2012 of the Ahar twin earthquakes) to validate the presented model based on two aspects: (1) building damages and (2) seismic intensity.Overall the results of this chapter suggest that the seismic hazard potential in district two of the city is almost high according to the seismic and vulnerability steps. For example brick-steel masonry buildings are most vulnerable (78% total damaged builds are masonry) in district two, most likely due to the disintegration of the mortar and bricks. Some old unreinforced masonry buildings in district two may even collapse as a consequence of a moderate near field earthquake. As a concluding remark must be noted that currently attentions should be focused on poor building construction, especially low quality materials, which do not comply with building standard codes for

earthquake-resistant design, and the lack of proper supervision during the construction operations of private buildings.

Appendix 1

Table 2.3 Topographic slope position of the seismic stations in six seismotectonic regions of Iran.

Name (Code)	Lat.	Long.	TPI 50	TPI 100	Seismotectonic region	Network	Vs30 (m/s)
1	36.05	53.7	Valley	Valley	Alborz & Azerbaijan	GSI	427.89
2	36.18	53.87	Upper slope	Ridge	Alborz & Azerbaijan	GSI	574.36
3	35.97	53.56	Flat	Valley	Alborz & Azerbaijan	GSI	443.95
4	35.99	53.62	Flat	Valley	Alborz & Azerbaijan	GSI	485.84
5	36.16	53.83	Lower slope	Valley	Alborz & Azerbaijan	GSI	545
6	36.14	53.67	Lower slope	Valley	Alborz & Azerbaijan	GSI	391.14
7	36.05	53.56	Valley	Valley	Alborz & Azerbaijan	GSI	760
8	36.09	53.93	Valley	Valley	Alborz & Azerbaijan	GSI	663.03
9	36.03	53.82	Flat	Valley	Alborz & Azerbaijan	GSI	329.67
10	35.95	53.65	Valley	Valley	Alborz & Azerbaijan	GSI	681.9
11	35.78	53.37	Ridge	Ridge	Alborz & Azerbaijan	GSI	505.57
12	35.75	53.36	Ridge	Ridge	Alborz & Azerbaijan	GSI	541.8
13	35.9	53.26	Flat	Valley	Alborz & Azerbaijan	GSI	760
14	35.6	53.12	Valley	Valley	Alborz & Azerbaijan	GSI	442.69
15	35.81	53.01	Steep slope	Steep slope	Alborz & Azerbaijan	GSI	468.66
16	35.95	53.1	Valley	Valley	Alborz & Azerbaijan	GSI	760
17	35.82	53.28	Valley	Valley	Alborz & Azerbaijan	GSI	750.28
18	35.91	52.98	Flat	Lower slope	Alborz & Azerbaijan	GSI	697.11
19	35.82	53.28	Valley	Valley	Alborz & Azerbaijan	GSI	750.28
20	35.8	53.2	Valley	Valley	Alborz & Azerbaijan	GSI	633.73
CHTH	35.91	51.13	Ridge	Upper slope	Alborz & Azerbaijan	IIEES	760
DAMV	35.63	51.97	Flat	Ridge	Alborz & Azerbaijan	IIEES	540.73
GRMI	38.81	47.89	Valley	Valley	Alborz & Azerbaijan	IIEES	432.85
MAKU	39.36	44.68	Flat	Ridge	Alborz & Azerbaijan	IIEES	484.01
THKV	35.92	50.88	Ridge	Ridge	Alborz & Azerbaijan	IIEES	759.13
QALM	36.43	50.65	Valley	Valley	Alborz & Azerbaijan	IGUT	760

QSDN	36.5	49.17	Flat	Ridge	Alborz & Azerbaijan	IGUT	741.44
ALA	36.08	52.81	Flat	Ridge	Alborz & Azerbaijan	IGUT	759.79
GLO	36.5	53.83	Flat	Ridge	Alborz & Azerbaijan	IGUT	599.98
KIA	36.21	53.68	Flat	Ridge	Alborz & Azerbaijan	IGUT	752.56
PRN	36.24	52.34	Upper slope	Ridge	Alborz & Azerbaijan	IGUT	750.67
SHM	35.81	53.28	Flat	Ridge	Alborz & Azerbaijan	IGUT	705.38
AZR	37.68	45.98	Flat	Ridge	Alborz & Azerbaijan	IGUT	694.01
BST	37.7	46.89	Upper slope	Ridge	Alborz & Azerbaijan	IGUT	396.98
HRS	38.32	47.04	Ridge	Ridge	Alborz & Azerbaijan	IGUT	753.94
HSH	37.31	47.26	Flat	Ridge	Alborz & Azerbaijan	IGUT	634.16
MRD	38.71	45.7	Flat	Ridge	Alborz & Azerbaijan	IGUT	701.39
SHB	38.28	45.62	Flat	Ridge	Alborz & Azerbaijan	IGUT	631.07
SRB	37.82	47.66	Ridge	Ridge	Alborz & Azerbaijan	IGUT	746.63
TABZ	38.06	46.33	Lower slope	Flat	Alborz & Azerbaijan	IGUT	414.72
TAHR	38.49	47.05	Upper slope	Upper slope	Alborz & Azerbaijan	IGUT	389.95
TBZ	38.23	46.15	Ridge	Ridge	Alborz & Azerbaijan	IGUT	649.83
TVRZ	38.5	46.67	Lower slope	Valley	Alborz & Azerbaijan	IGUT	345.46
DMV	35.58	52.03	Flat	Ridge	Alborz & Azerbaijan	IGUT	700.19
FIR	35.64	52.75	Ridge	Ridge	Alborz & Azerbaijan	IGUT	608.29
GZV	36.39	50.22	Flat	Ridge	Alborz & Azerbaijan	IGUT	604.85
TEH	35.75	51.39	Ridge	Ridge	Alborz & Azerbaijan	IGUT	420.01
MAHB	36.77	45.71	Valley	Valley	Alborz & Azerbaijan	IGUT	369.63
AFJ	35.86	51.71	Flat	Ridge	Alborz & Azerbaijan	IGUT	760
FTB	38.02	46.39	Upper slope	Ridge	Alborz & Azerbaijan	IGUT	441.04
SHR	35.81	51.29	Upper slope	Ridge	Alborz & Azerbaijan	IGUT	742.32
21	35.54	53.3	Valley	Valley	Central Iran	GSI	351.31
Maku	39.308	44.509	Upper slope	Ridge	Alborz & Azerbaijan	BHRC	563.98
Manjil	36.763	49.392	Flat	Valley	Alborz & Azerbaijan	BHRC	700.95
Rudbar	36.8	49.4	Upper slope	Ridge	Alborz & Azerbaijan	BHRC	453.22

Lahijan	37.21	50.03	Upper slope	Upper slope	Alborz & Azerbaijan	BHRC	350.98
Rudsar	37.13	50.3	Ridge	Upper slope	Alborz & Azerbaijan	BHRC	263.67
Talesh	37.8	48.9	Valley	Valley	Alborz & Azerbaijan	BHRC	387.1
Tonkabon	36.808	50.884	Lower slope	Lower slope	Alborz & Azerbaijan	BHRC	303.36
ASAO	34.55	50.03	Valley	Valley	Central Iran	IIEES	445.5
GHVR	34.48	51.3	Valley	Valley	Central Iran	IIEES	302.21
KRBR	29.98	56.76	Upper slope	Ridge	Central Iran	IIEES	469.73
KHMZ	33.74	49.96	Upper slope	Ridge	Central Iran	IIEES	413.1
NASN	32.8	52.81	Ridge	Ridge	Central Iran	IIEES	509.73
SHRD	35.99	56.01	Flat	Ridge	Central Iran	IIEES	433.69
TABS	33.65	57.12	Steep slope	Flat	Central Iran	IIEES	602.82
ZNJK	36.67	48.69	Ridge	Ridge	Central Iran	IIEES	546.86
YAZD	32.46	54.68	Flat	Valley	Central Iran	IIEES	636.56
HAGD	34.82	49.14	Ridge	Ridge	Central Iran	IGUT	702.34
HSRG	35.24	48.28	Flat	Ridge	Central Iran	IGUT	755.29
ANAR	33.19	53.73	Valley	Valley	Central Iran	IGUT	574.43
GAR	32.41	52.05	Flat	Ridge	Central Iran	IGUT	643.31
KLH	33.32	51.58	Ridge	Ridge	Central Iran	IGUT	553.79
KRSH	33.97	52.14	Valley	Valley	Central Iran	IGUT	523.52
QAM	33.76	51.44	Flat	Valley	Central Iran	IGUT	723.68
RAM	31.81	52.38	Flat	Valley	Central Iran	IGUT	651.76
ZEF	32.9	52.33	Ridge	Ridge	Central Iran	IGUT	760
CHMN	29.86	57.54	Flat	Ridge	Central Iran	IGUT	506.82
KHGB	30.38	56.48	Valley	Valley	Central Iran	IGUT	417.72
NGRK	29.64	56.73	Upper slope	Ridge	Central Iran	IGUT	689.74
TVBK	29.99	56.76	Flat	Ridge	Central Iran	IGUT	471.88
MOG	36.11	59.34	Flat	Ridge	Central Iran	IGUT	756.12
PAY	36.45	58.99	Flat	Ridge	Central Iran	IGUT	563.96
QABG	35.71	49.58	Upper slope	Steep slope	Central Iran	IGUT	610.07

QCNT	36.29	50.01	Lower slope	Valley	Central Iran	IGUT	328.21
GZV	36.39	57.61	Flat	Ridge	Central Iran	IGUT	670.83
ANJ	35.47	53.91	Flat	Ridge	Central Iran	IGUT	587.8
LAS	35.38	52.96	Upper slope	Ridge	Central Iran	IGUT	520.94
TKDS	33.61	57.12	Ridge	Ridge	Central Iran	IGUT	726.23
TNSJ	33.96	56.61	Ridge	Ridge	Central Iran	IGUT	414.25
TPRV	33.03	56.69	Valley	Valley	Central Iran	IGUT	372.15
HSB	35.44	51.28	Ridge	Ridge	Central Iran	IGUT	437.55
MHD	35.69	50.67	Steep slope	Ridge	Central Iran	IGUT	760
QOM	34.84	51.06	Steep slope	Upper slope	Central Iran	IGUT	504.53
RAZ	35.4	49.93	Flat	Ridge	Central Iran	IGUT	400.38
SFB	34.35	52.24	Lower slope	Valley	Central Iran	IGUT	477.38
VRN	35	51.73	Ridge	Ridge	Central Iran	IGUT	514.36
BAF	31.59	55.57	Flat	Ridge	Central Iran	IGUT	464.05
CHK	32.24	54.41	Ridge	Ridge	Central Iran	IGUT	748.59
MEH	31.39	54.61	Flat	Ridge	Central Iran	IGUT	717.29
SAD	31.91	53.69	Upper slope	Ridge	Central Iran	IGUT	619.32
HKZM	35.38	48.9	Flat	Ridge	Central Iran	IGUT	560.47
IL3	35.48	51.02	Upper slope	Ridge	Central Iran	IGUT	346.13
IL5	35.21	50.58	Upper slope	Ridge	Central Iran	IGUT	390.94
QBNZ	35.64	50.19	Steep slope	Steep slope	Central Iran	IGUT	623.57
TBB	35	51.73	Ridge	Ridge	Central Iran	IGUT	514.36
Tabas	33.58	56.92	Steep slope	Steep slope	Central Iran	BHRC	324.36
Ghazvin	36.26	50.01	Ridge	Ridge	Central Iran	BHRC	310.21
Golbaf	29.88	57.72	Upper slope	Upper slope	Central Iran	BHRC	420.05
Abhar	36.09	49.22	Ridge	Upper slope	Central Iran	BHRC	438.01
BNDS	27.4	56.17	Ridge	Ridge	Zagros	IIEES	760
GHIR	28.29	52.99	Ridge	Ridge	Zagros	IIEES	414.34
RMKL	30.98	49.81	Lower slope	Valley	Zagros	IIEES	356.9

SNGE	35.09	47.35	Ridge	Ridge	Zagros	IIEES	443.93
SHGR	32.11	48.8	Upper slope	Ridge	Zagros	IIEES	400.68
AHRM	28.86	51.3	Lower slope	Valley	Zagros	IIEES	500.55
ILAM	33.62	46.2	Lower slope	Valley	Zagros	IIEES	521.83
YASJ	31.1	51.3	Ridge	Ridge	Zagros	IIEES	760
3791	28.37	52.6	Steep slope	Steep slope	Zagros	GSI	567.08
3764	28.31	52.62	Flat	Valley	Zagros	GSI	745.29
3797	28.19	52.35	Upper slope	Upper slope	Zagros	GSI	265.13
3768	28.49	52.3	Ridge	Ridge	Zagros	GSI	474.69
3766	28.05	52.51	Steep slope	Steep slope	Zagros	GSI	248.47
3770	28	52.74	Steep slope	Steep slope	Zagros	GSI	348.78
3786	28.19	52.41	Ridge	Ridge	Zagros	GSI	319.57
3798	28.41	52.38	Ridge	Ridge	Zagros	GSI	398.1
MYP1	27.99	52.36	Upper slope	Upper slope	Zagros	GSI	499.47
BDRS	33.95	48.88	Flat	Ridge	Zagros	IGUT	646.35
BMDN	33.67	48.82	Steep slope	Steep slope	Zagros	IGUT	630.95
HALM	34.86	48.17	Flat	Ridge	Zagros	IGUT	631.9
HSAM	34.21	48.6	Flat	Ridge	Zagros	IGUT	580.19
KLNJ	31.01	51.59	Upper slope	Ridge	Zagros	IGUT	756.48
PIR	32.68	50.89	Flat	Ridge	Zagros	IGUT	523.71
KHNJ	27.95	57.71	Valley	Valley	Zagros	IGUT	344.52
BZA	34.47	47.86	Flat	Ridge	Zagros	IGUT	728.45
DHR	34.7	46.39	Upper slope	Ridge	Zagros	IGUT	541.79
GHG	34.33	46.57	Flat	Ridge	Zagros	IGUT	728.61
KCHF	34.28	47.04	Flat	Ridge	Zagros	IGUT	554.94
KER	34.39	47.13	Flat	Valley	Zagros	IGUT	760
KOM	34.18	47.51	Flat	Ridge	Zagros	IGUT	472.98
LIN	34.92	46.96	Flat	Ridge	Zagros	IGUT	611.85
VIS	34.53	46.85	Flat	Ridge	Zagros	IGUT	758.3

DOB	33.79	48.18	Flat	Ridge	Zagros	IGUT	708.32
KFM	33.52	47.85	Flat	Ridge	Zagros	IGUT	716.36
KMR	33.52	48.38	Flat	Ridge	Zagros	IGUT	700.21
BNB	27.45	56.54	Ridge	Steep slope	Zagros	IGUT	338.79
GENO	27.4	56.17	Upper slope	Ridge	Zagros	IGUT	760
NIAN	27.56	56.83	Ridge	Ridge	Zagros	IGUT	541.16
BRJ	31.91	51.26	Valley	Valley	Zagros	IGUT	686.06
JHBN	32.23	50.67	Upper slope	Ridge	Zagros	IGUT	756.24
ROKH	32.4	51.07	Upper slope	Upper slope	Zagros	IGUT	565.81
ZNGN	32.12	50.85	Flat	Ridge	Zagros	IGUT	741.21
GHB	29.38	52.54	Flat	Ridge	Zagros	IGUT	760
JHRM	28.51	53.58	Ridge	Ridge	Zagros	IGUT	311.55
KAZ	29.78	51.84	Flat	Ridge	Zagros	IGUT	760
LAR1	27.67	54.37	Ridge	Ridge	Zagros	IGUT	238.13
LMD1	27.34	53.16	Ridge	Ridge	Zagros	IGUT	323.54
SHI	29.64	52.52	Flat	Ridge	Zagros	IGUT	595.57
SRV	29.38	53.1	Flat	Ridge	Zagros	IGUT	687.28
AHWZ	31.33	48.64	Valley	Valley	Zagros	IGUT	221.97
BND	27.45	56.54	Ridge	Steep slope	Zagros	IGUT	338.79
DHL1	32.68	47.28	Upper slope	Ridge	Zagros	IGUT	300.22
KHSK	26.76	57.05	Upper slope	Ridge	Makran	IGUT	316.83
MOK	29.04	52.71	Flat	Ridge	Zagros	IGUT	553.34
PAR	29.84	53.03	Valley	Valley	Zagros	IGUT	737.5
Jovakan	29.037	52.571	Steep slope	Steep slope	Zagros	BHRC	396.59
Naghan	31.98	51.22	Lower slope	Lower slope	Zagros	BHRC	309.33
Saadabad	29.38	51.116	Steep slope	Steep slope	Zagros	BHRC	321.71
Kavar	29.17	53.03	Flat	Lower slope	Zagros	BHRC	473.91
Zanjiran	29.07	52.62	Flat	Valley	Zagros	BHRC	643.81
Fin	27.63	55.895	Valley	Valley	Zagros	BHRC	379.87

Firouzabad	28.83	52.56	Lower slope	Lower slope	Zagros	BHRC	270.39
Zarrat	29.094	52.847	Lower slope	Valley	Zagros	BHRC	503.03
Hosseinieh	32.679	48.246	Steep slope	Flat	Zagros	BHRC	426.22
Shabankareh	29.471	50.988	Upper slope	Upper slope	Zagros	BHRC	297.18
BJRD	37.7	57.41	Lower slope	Valley	Kopet Dag	IIEES	520.67
MRVT	37.66	56.09	Steep slope	Ridge	Kopet Dag	IIEES	426.77
MSHD	36.59	59.94	Ridge	Ridge	Kopet Dag	IIEES	736.49
JRKH	35.91	60.35	Steep slope	Ridge	Kopet Dag	IGUT	432.89
KRD	36.78	59.51	Ridge	Ridge	Kopet Dag	IGUT	741.3
MYA	36.34	60.1	Flat	Ridge	Kopet Dag	IGUT	653.18
SRO	36.31	59.47	Lower slope	Valley	Kopet Dag	IGUT	528.65
AKL	36.59	58.75	Flat	Ridge	Kopet Dag	IGUT	493.03
EMG	37.41	58.65	Flat	Ridge	Kopet Dag	IGUT	486.86
SFR	37.05	58	Flat	Ridge	Kopet Dag	IGUT	599.93
MND	37.24	55.39	Ridge	Ridge	Kopet Dag	IGUT	506.25
MHI	36.31	59.47	Lower slope	Valley	Kopet Dag	IGUT	528.65
QHU	37.07	58.54	Upper slope	Steep slope	Kopet Dag	IGUT	304.05
SHV	37.53	57.7	Steep slope	Ridge	Kopet Dag	IGUT	673.13
Abbar	36.7	55.06	Upper slope	Ridge	Kopet Dag	BHRC	508.48
CHBR	25.6	60.48	Ridge	Ridge	Makran	IIEES	295.32
MNB1	27.11	57.1	Upper slope	Upper slope	Makran	IGUT	270.6
SHRT	33.65	60.29	Ridge	Ridge	Lut	IIEES	409.13
ZHSF	29.61	60.78	Ridge	Ridge	Lut	IIEES	479.94
BSRN	32	59.12	Ridge	Ridge	Lut	IIEES	343.41
GNBJ	34.31	58.33	Ridge	Ridge	Lut	IIEES	653.32
DAH	32.74	59.87	Lower slope	Lower slope	Lut	IGUT	627.86
KOO	32.42	59	Ridge	Ridge	Lut	IGUT	647.97
MON	33.19	59.67	Flat	Ridge	Lut	IGUT	448.24
NHDN	31.39	60.05	Upper slope	Upper slope	Lut	IGUT	430.54

TEG	32.9	58.75	Flat	Ridge	Lut	IGUT	470.36
SZD1	29.49	60.87	Valley	Valley	Lut	IGUT	296.76
Deyhuk	33.29	57.5	Valley	Valley	Lut	BHRC	398.62
Ghaen	33.73	59.22	Steep slope	Steep slope	Lut	BHRC	390.27
Kakhk	34.14	58.66	Upper slope	Steep slope	Lut	BHRC	469.39
Vendik	33.82	59.23	Valley	Valley	Lut	BHRC	425.15